Theory of ultrashort quantum states and their detection through electro-optic sampling

Dissertation zur Erlangung des akademischen Grades

eines Doktors der Naturwissenschaften

(Dr. rer. nat)

vorgelegt von

Matthias Kizmann

an der

Universität Konstanz

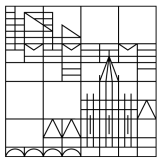

Mathematisch-Naturwissenschaftliche Sektion

Fachbereich Physik

Tag der mündlichen Prüfung: 23. Februar 2022

1. Referent: Prof. Dr. Andrey S. Moskalenko

2. Referent: Prof. Dr. Oded Zilberberg

Abstract

Light represents one of the most fundamental and also natural ways of information transfer available in both physics and our everyday life. As a result, quantum optics possesses large overlaps with many fields like nonlinear optics, quantum information theory, spectroscopy and the fundamentals of quantum mechanics. Conventionally, the photon statistics of light are studied using techniques like homodyne detection or coincidence measurements. Recently, a quantum extension of classical electro-optic sampling was developed, which enables the measurement of electric field statistics on ultrashort time scales. This measurement relies on a nonlinear interaction between an ultrashort classical probe and the sampled quantum field to impose its quantum statistics on the polarization state of the probe. In this thesis, we aim at advancing the theoretical description of this method and exploring its applications in the study of the nature of ultrashort quantum fields.

First, we discuss the role of the electro-optic process in the generation of ultrashort squeezed states. Here, we formulate a consistent time-domain theory of the generation and sampling of few-cycle and subcycle pulsed squeezed states. We show that the electro-optic process can be used to induce effective local accelerations in the propagation of the electric field, which lead to its squeezing. We provide a relativistic interpretation of this process in terms of induced changes in the local flow of time.

Afterwards, we develop a microscopic quantum theory of the electro-optic process adopting an ensemble of non-interacting three-level systems as a model for the nonlinear material. We show that the response of the nonlinear medium can be separated into a conventional part, which is also exploited in the sampling of classical coherent electric fields, and quantum contributions, which are independent of the state of the terahertz input. The quantum contribution arises from initially absent interactions between the three-level systems which are mediated by terahertz vacuum fluctuations. Here, time-ordering effects related to the ultrashort nature of the involved fields need to be taken into account. We also determine conditions under which the classical response serves as a good approximation of the electro-optic process and show that electro-optic sampling can serve as a spectroscopic tool to study the pure quantum susceptibilities of matter

in a complementary regime. The time-ordering effects in the electro-optic process are further discussed in terms of an effective Hamiltonian, where the effects of the spatial gating of the sampled terahertz vacuum field are taken into account.

Finally, we show that the statistics of the sampled terahertz field can be reconstructed from the measured statistics of the electro-optic signal by eliminating the fluctuations associated with the near-infrared frequencies of the probe. Here, a detailed theoretical model of the sampling of vacuum fluctuations is needed, whose foundations have been developed in the previous chapters. We find that the resulting terahertz statistics describe the quantum characteristics of ultrashort, few-cycle terahertz states of quantum light.

Zusammenfassung

Licht repräsentiert eine der fundamentalsten und auch natürlichsten Arten der Informationsübertragung, welche uns sowohl in der Physik als auch in unserem täglichen Leben zur Verfügung stehen. Aufgrund dessen besitzt die Quantenoptik einen großen Überlapp mit anderen Bereichen wie der nichtlinearen Optik, der Quanteninformationstheorie, der Spektroskopie und den Grundlagen der Quantenmechanik. Üblicherweise wird die Photonenstatistik von Licht durch Techniken wie die homodyne Detektion oder Koinzidenzmessungen untersucht. Vor kurzem wurde eine quantenmechanische Erweiterung des klassischen elektrooptischen Abtastens entwickelt, welche die Messung elektrischer Feldstatistiken auf ultrakurzen Zeitskalen ermöglicht. Diese Messung beruht auf einer nichtlinearen Wechselwirkung zwischen einem ultrakurzen klassischen Abtastimpuls und dem abgetasteten Quantenfeld, welche dessen Quantenstatistik auf den Polarisationszustand des Abtastimpulses überträgt. In dieser Dissertation soll die theoretische Beschreibung dieser Methode erweitert, und ihre Anwendungen bei der Erforschung der Charakteristiken ultrakurzer Quantenfelder untersucht werden.

Wir beschreiben zunächst die Anwendung des elektrooptischen Prozesses bei der Erzeugung von ultrakurzen gequetschten Zuständen. Dabei formulieren wir eine konsistente Theorie der Erzeugung und Abtastung von ultrakurzen gepulsten Zuständen mit einzelnen oder wenigen Zyklen in der Zeitdomäne. Wir zeigen, dass mit dem elektrooptischen Verfahren effektive lokale Beschleunigungen in der Propagation des elektrischen Feldes induziert werden können, die zum Quetschen des Feldes führen. Dabei präsentieren wir eine relativistische Interpretation dieses Prozesses in Bezug auf induzierte Änderungen des lokalen Zeitflusses.

Im zweiten Teil entwickeln wir eine mikroskopische Quantentheorie des elektrooptischen Prozesses, wobei wir ein Ensemble nicht-wechselwirkender Drei-Niveau-Systeme als Modell für das nichtlineare Material verwenden. Wir zeigen, dass die Antwort des nichtlinearen Mediums in einen konventionellen Teil und einen Quantenteil unterteilt werden kann. Der konventionelle Teil wird auch bei der Abtastung klassischer kohärenter elektrischer Felder ausgenutzt, wohingegen der quantenmechanische Teil unabhängig vom Zustand des eingehenden Terahertz-Feldes ist. Der Quantenteil ergibt

sich aus zunächst abwesenden Wechselwirkungen zwischen den Drei-Niveau-Systemen, die durch Terahertz-Vakuumfluktuationen übertragen werden. Dabei müssen zeitliche Ordnungseffekte im Zusammenhang mit der ultrakurzen Pulszeit der beteiligten Felder berücksichtigt werden. Wir demonstrieren Bedingungen, unter denen die klassische Antwort eine gute Näherung des elektrooptischen Prozesses darstellt und zeigen, dass das elektrooptische Abtasten alternativ auch als spektroskopisches Werkzeug dienen kann, um die reinen Quantensuszeptibilitäten der Materie zu untersuchen. Die zeitlichen Ordnungseffekte im elektrooptischen Prozess werden darüberhinaus im Hinblick auf einen effektiven Hamilton-Operator diskutiert, wobei die Effekte der räumlichen Mittelung des abgetasteten Terahertz-Vakuumfeldes berücksichtigt werden.

Schlußendlich zeigen wir, dass die Statistik des abgetasteten Terahertz-Feldes aus der gemessenen Statistik des elektrooptischen Signals rekonstruiert werden kann indem die nahinfrarotfrequenten Fluktuationen des Abtastimpulses eliminiert werden. Dies erfordert ein detailliertes theoretisches Modell des Abtastens von Vakuumfluktuationen, dessen Grundlagen in den vorangegangenen Kapiteln entwickelt wurden. Wir stellen fest, dass die resultierenden Terahertz-Statistiken die Quanteneigenschaften von ultrakurzen Terahertz-Quantenzuständen des Lichts mit wenigen Zyklen beschreiben.

Acknowledgments

As I am finishing this thesis, I suddenly realize that my time as a PhD student is slowly coming to an end. I would like to thank my supervisors Guido Burkard and Andrey S. Moskalenko for their guidance throughout my PhD which helped me to form the foundations of my education. They provided numerous advices, both scientifically and also in terms of my future career. Here, I learned what it means to be scientifically rigorous and how to communicate my ideas. I also want to thank my other collaborators Alfred Leitenstorfer, Shaul Mukamel, Thiago Lucena de Macedo Guedes, Philipp Sulzer, and Denis V. Seletskiy. I always had fun exploring ideas and participating in in-depth discussions.

I also want to thank all my present and former friends and colleagues in Konstanz: Alessandro David, Jonas Mielke, Matthew Brooks, Maximilian Russ, Vladyslav Shkolnykov, Monica Benito Gonzales, Florian Ginzel, Philipp Mutter, Benjamin D'Anjou, Thiago Lucena de Macedo Guedes, Amin Hosseinkhani, Csaba Peterfalvi, Irinia Heinz, Benedikt Tissot, Emanuel Hubenschmid, Regina Finsterhölzl, Violeta Ivanova-Rohling, Joris Kattemölle, Stephen McMillan, Lin Wang, Andor Kormanyos, and Susanne Später. You helped me catching a break when I hit a wall during my research and always provided some much needed distraction.

I am especially grateful to the Landesgraduiertenförderungsgesetz of the state Baden-Württemberg, whose scholarship allowed me to start my PhD in the first place.

I would like to thank my family and friends for all the support and guidance throughout my life. My parents always tried to provide the best environment for me to focus on the things that are important to me and I am eternally grateful for their support. Patrick Luzenko, Melanie Kizmann, Kevin Bohl, Tobias Bohl, Thiago Lucena de Macedo Guedes, and Cornelia Kizmann helped me out tremendously by suffering through the task of reading through the first versions of my thesis.

Lastly, I want to thank my wife Cornelia Kizmann for the endless reassurances that I am indeed able to pull this off. You are the person that I can always talk to and who I want to have by my side during the bad and the good times.

Abbreviations

NIR	near-infrared
THz	terahertz
SFG	sum frequency generation
DFG	difference frequency generation
MIR	mid-infrared
SVAA	slowly-varying amplitude approximation
EOM	electro-optic medium
WP	Wollaston Prism
GX	generation crystal
RWA	rotating-wave approximation

Contents

Chapter 1

Introduction

It was Max Planck and his solution to the problem of the ultraviolet catastrophe of black-body radiation in classical physics that marked the beginning of the development of quantum mechanics in the year 1900. Planck introduced the notion of quantization by treating the black body as a group of oscillators with discrete energy levels, which led to an effective quantization in the frequencies of the emitted light. The second major milestone along the discovery of the principles of quantum mechanics was developed in 1905 by Alfred Einstein, who applied the idea of quantization to optics itself by proposing that the energy of electromagnetic radiation can only be transported in discrete packages proportional to their frequency. Twenty more years were needed to finally formulate the basic principles of quantum mechanics still in use today.

Despite its fundamental role in the discovery of quantum mechanics, the field of optics kept relying heavily on classical or semiclassical descriptions for photon statistics. These theories were successful due to the fact that most measurements involved the detection of a large number of photons. In contrast, the theoretical description of electrodynamic effects were restricted to states possessing only a small number of photons. From a historic point of view, classical optics already presented a matured field with a well developed physical framework in terms of the Maxwell Equations, while atomic physics was just beginning to form at the start of the 20th century.

The field of optics was first made aware of its lack of a sufficient quantum description for the photon statistics of electromagnetic radiation when Hanbury-Brown and Twiss[1–3] presented their work on the measurement of the diameter of stars. To this end, they developed an intensity interferometer which from today's viewpoint represented the first measurement of the second-order correlation function of electromagnetic radiation. Both the observations by Hanbury-Brown and Twiss and the development of the laser (or more specifically maser) served as the inspiration for Glauber to ultimately develop the theory of optical coherence[4, 5], which can be seen as the fundamental

building block of modern quantum optics.

The development of laser light not only played a crucial role in the formulation of optical coherence, but also the discovery of nonlinear effects. Usually, pulsed lasers are employed to study nonlinear effects, since their short duration leads to very high peak intensities enabling the observation of these effects. In modern physics, the employment of ultrashort light pulses in the study of ultrafast physical phenomena is ubiquitous. In classical optics, various techniques for the time-resolved detection of classical electric field transients on ultrashort time scales are available.

Only recently, a quantum version of electro-optic sampling has been demonstrated to enable the detection of quantum electric fields with equivalent temporal resolution to its classical counterpart. In classical electro-optic sampling, a near-infrared (NIR) ultrashort probe is used to sample a classical terahertz (THz) field. The temporal duration of the probe is usually much shorter than half a cycle of the sampled THz field. Both fields are sent into a second-order nonlinear crystal where the THz field changes the polarization direction of the probe proportionally to its local field strength at the peak of the probe. Measuring this change in the polarization direction of the probe for different delay times between the probe and the THz field allows to resolve the temporal trace of the THz field. If this experiment is performed in the absence of a classical THz transient, the average change in the polarization direction of the probe vanishes. However, collecting the statistics of the measured polarization changes reveals that its fluctuations increase proportionally to the vacuum fluctuations of the THz vacuum gated in time and space by the probe[6–9].

In this chapter, the main concepts of the quantization of the electromagnetic field and its interaction with both linear and nonlinear matter are introduced to the extent needed in order to understand the main results of this thesis. In chapter 2, the generation and subsequent detection of ultrashort squeezed states of light and their connection to accelerated reference frames is presented. Chapter 3 provides a microscopic model of the electro-optic process and discusses the role of quantum susceptibilities and time-ordering effects in the generation of the electro-optic signal. These time-ordering effects are treated further within the framework of an effective Hamiltonian in chapter 4, where arbitrary propagation directions for the THz field are taken into account. Finally, chapter 5 demonstrates that the Wigner function of ultrashort THz states can be reconstructed from the measured statistics of the electro-optic signal. Chapter 6 provides a short recap of the main results of this thesis.

1.1 Free electromagnetic field quantization

In this chapter we want to derive the quantization of the electromagnetic field in the vacuum (i.e. in absence of any charges). The canonical quantization procedure of a classical theory involves the derivation of the Hamiltonian through the Lagrangian. Afterwards, the canonical conjugates can be promoted to operators and their Poisson brackets are replaced by commutators (multiplied by the factor $i\hbar$).

1.1.1 Maxwell Equations

The classical electromagnetic fields are described elegantly by the microscopic Maxwell equations[10–13]

$$\nabla \cdot \mathbf{E}(\mathbf{r}) = \frac{\rho(\mathbf{r})}{\varepsilon_0}, \tag{1.1a}$$

$$\nabla \cdot \mathbf{B}(\mathbf{r}) = 0, \tag{1.1b}$$

$$\nabla \times \mathbf{E}(\mathbf{r}) + \frac{\partial}{\partial t}\mathbf{B}(\mathbf{r}) = 0, \tag{1.1c}$$

$$\nabla \times \mathbf{B}(\mathbf{r}) - \frac{1}{c_0^2}\frac{\partial}{\partial t}\mathbf{E}(\mathbf{r}) = \frac{1}{\varepsilon_0 c_0^2}\mathbf{j}(\mathbf{r}), \tag{1.1d}$$

where $\mathbf{E}(\mathbf{r})$ is the electric field, $\mathbf{B}(\mathbf{r})$ is the magnetic field, $\rho(\mathbf{r})$ is the charge density, $\mathbf{j}(\mathbf{r})$ is the current density, ε_0 is the vacuum permittivity, and c_0 is the speed of light in the vacuum. From here on out, we will use bold letters to denote vectors. Looking at Eq. (1.1b), we can see that this equation is fulfilled automatically if we express the magnetic field in terms of a so-called vector potential $\mathbf{A}(\mathbf{r})$,

$$\mathbf{B}(\mathbf{r}) = \nabla \times \mathbf{A}(\mathbf{r}), \tag{1.2}$$

since the divergence of the curl of a vector field always vanishes. If we use Eq. (1.2) in Eq. (1.1c), we obtain

$$\nabla \times \left(\mathbf{E}(\mathbf{r}) + \frac{\partial}{\partial t}\mathbf{A}(\mathbf{r})\right) = 0. \tag{1.3}$$

Similarly, we can express the electric field in terms of a so-called scalar potential $\phi(\mathbf{r})$ (and also the vector potential),

$$\mathbf{E}(\mathbf{r}) = -\nabla\phi(\mathbf{r}) - \frac{\partial}{\partial t}\mathbf{A}(\mathbf{r}), \tag{1.4}$$

so that Eq. (1.1c) is fulfilled automatically. The introduction of the potentials $\phi(\mathbf{r})$ and $\mathbf{A}(\mathbf{r})$ is closely related to Helmholtz's theorem, which states that any sufficiently smooth and rapidly decaying vector field in three dimensions can be decomposed into a curl-free and a divergence-free part. For the electric field, the vector potential $\mathbf{A}(\mathbf{r})$ is connected to the divergence-free part and the scalar potential $\phi(\mathbf{r})$ is connected to the curl-free part.

Introducing the vector and scalar potential has allowed us to eliminate Eqs. (1.1b) and (1.1c). The two remaining Eqs. (1.1a) and (1.1d) can then be reformulated using Eq. (1.2) and (1.4),

$$\nabla^2\phi(\mathbf{r}) + \frac{\partial}{\partial t}\nabla\cdot\mathbf{A}(\mathbf{r}) = -\frac{\rho(\mathbf{r})}{\varepsilon_0}, \tag{1.5a}$$

$$\nabla^2\mathbf{A}(\mathbf{r}) - \frac{1}{c_0^2}\frac{\partial^2}{\partial t^2}\mathbf{A}(\mathbf{r}) - \nabla\left(\nabla\cdot\mathbf{A}(\mathbf{r}) + \frac{1}{c_0^2}\frac{\partial}{\partial t}\phi(\mathbf{r})\right) = -\frac{1}{\varepsilon_0 c_0^2}\mathbf{j}(\mathbf{r}), \tag{1.5b}$$

where we used the identity

$$\nabla\times\nabla\times\mathbf{A}(\mathbf{r}) = -\nabla^2\mathbf{A}(\mathbf{r}) + \nabla\left(\nabla\cdot\mathbf{A}(\mathbf{r})\right). \tag{1.6}$$

These two equations can be simplified further by noticing that the two potentials are not defined uniquely by Eq. (1.2) and (1.4). This leaves room for different gauges that change the potentials but leave the electromagnetic fields unperturbed. Looking at Eq. (1.2), we notice that adding the gradient of an arbitrary scalar function $f(\mathbf{r})$ to $\mathbf{A}(\mathbf{r})$ leaves the magnetic field unchanged,

$$\mathbf{A}(\mathbf{r}) \to \mathbf{A}'(\mathbf{r}) = \mathbf{A}(\mathbf{r}) + \nabla f(\mathbf{r}). \tag{1.7}$$

Correspondingly, $\phi(\mathbf{r})$ has to be changed according to

$$\phi(\mathbf{r}) \to \phi'(\mathbf{r}) = \phi(\mathbf{r}) - \frac{\partial}{\partial t}f(\mathbf{r}) \tag{1.8}$$

in order to leave the electric field in Eq. (1.4) unchanged.

One particularly useful example of this gauge freedom is given by the Coulomb gauge $\nabla\cdot\mathbf{A}(\mathbf{r}) = 0$, in which Eqs. (1.5a) and (1.5b) are given by

$$\nabla^2\phi(\mathbf{r}) = -\frac{\rho(\mathbf{r})}{\varepsilon_0}, \tag{1.9a}$$

$$\left(\nabla^2 - \frac{1}{c_0^2}\frac{\partial^2}{\partial t^2}\right)\mathbf{A}(\mathbf{r}) - \frac{1}{c_0^2}\nabla\left(\frac{\partial}{\partial t}\phi(\mathbf{r})\right) = -\frac{1}{\varepsilon_0 c_0^2}\mathbf{j}(\mathbf{r}). \tag{1.9b}$$

In this gauge, the two potentials $\mathbf{A}(\mathbf{r})$ and $\phi(\mathbf{r})$ can be understood as generating the

transversal and longitudinal (with respect to the propagation direction) parts of the electromagnetic fields, respectively. Therefore, according to Eq. (1.2), the magnetic field does not possess any longitudinal component, while Eq. (1.4) shows that the electric field can have a longitudinal part, given by the scalar potential $\phi(\mathbf{r})$. This longitudinal part results from the charge density $\rho(\mathbf{r})$ in Eq. (1.1a). The transversal part of $\mathbf{E}(\mathbf{r})$ originates from the vector potential $\mathbf{A}(\mathbf{r})$ in Eq. (1.4).

In the absence of charged particles, the charge and current density in Eqs. (1.1a) and (1.1d) are set to zero, i.e., $\rho(\mathbf{r}) = 0$ and $\mathbf{j}(\mathbf{r}) = 0$. Equation (1.1a) shows that now also the electric field does not possess a longitudinal part. This means that the scalar potential can be taken to vanish in Eq. (1.4) and only the vector potential remains to be determined by

$$\left(\nabla^2 - \frac{1}{c_0^2}\frac{\partial^2}{\partial t^2}\right)\mathbf{A}(\mathbf{r}) = 0. \tag{1.10}$$

1.1.2 Lagrangian and canonical quantization

Having introduced the vector potential and the Coulomb gauge, we can now move on to define the Lagrangian of the electromagnetic field [10, 11]. In absence of charged particles the Lagrangian, in the Coulomb gauge, is given by

$$L = \frac{\varepsilon_0}{2}\int \mathrm{d}^3 r \ \left\{\dot{\mathbf{A}}^2(\mathbf{r}) - c_0^2[\nabla \times \mathbf{A}(\mathbf{r})]^2\right\}, \tag{1.11}$$

where we have used the notation $\dot{\mathbf{A}}(\mathbf{r}) = \frac{\partial}{\partial t}\mathbf{A}(\mathbf{r})$ for brevity. Indeed, using the Euler-Lagrange Equation

$$\frac{\mathrm{d}}{\mathrm{d}t}\frac{\delta L}{\delta \dot{\mathbf{A}}(\mathbf{r})} - \frac{\delta L}{\delta \mathbf{A}(\mathbf{r})} = 0 \tag{1.12}$$

results in the wave equation for the vector potential, given in Eq. (1.10). Note that the vector potential needs to be varied in the space of transverse vector functions $\mathbf{g}(\mathbf{r})$, with $\nabla \cdot \mathbf{g}(\mathbf{r}) = 0$. This ensures that $\mathbf{A}(\mathbf{r})$ remains in the Coulomb gauge. In this case, the functional derivative $\frac{\delta}{\delta \mathbf{g}(\mathbf{r})}$ of a functional $F[\mathbf{g}(\mathbf{r})]$ is given by

$$\frac{\delta F[\mathbf{g}(\mathbf{r})]}{\delta \mathbf{g}(\mathbf{r})} = \lim_{\varepsilon \to 0}\frac{1}{\varepsilon}\left(F[\mathbf{g}(\mathbf{r}') + \varepsilon\delta^{\perp}(\mathbf{r} - \mathbf{r}')] - F[\mathbf{g}(\mathbf{r}')]\right). \tag{1.13}$$

Here, $\delta^{\perp}(\mathbf{r})$ denotes the perpendicular delta function

$$\delta_{ij}^{\perp}(\mathbf{r}) = \frac{1}{(2\pi)^3}\int \mathrm{d}^3 k \ e^{i\mathbf{k}\mathbf{r}}\left(\delta_{ij} - \frac{k_i k_j}{k^2}\right) = \delta_{ij}\delta(\mathbf{r}) + \frac{1}{4\pi}\frac{\partial^2}{\partial r_i \partial r_j}\frac{1}{r}, \tag{1.14}$$

where $i, j = 1, 2, 3$ are the indices for the three spatial dimensions. The transverse part of a vector field $\mathbf{V}(\mathbf{r})$ can then be found by $V_i^{\perp}(\mathbf{r}) = \sum_j \int \mathrm{d}^3 r' \delta_{ij}^{\perp}(\mathbf{r} - \mathbf{r}') V_j(\mathbf{r}')$.

The Hamiltonian of the free electromagnetic field is now given by

$$H = \int \mathrm{d}^3 r \; \mathbf{\Pi}(\mathbf{r}) \dot{\mathbf{A}}(\mathbf{r}) - L = \int \mathrm{d}^3 r \frac{\varepsilon_0}{2} \left\{ \mathbf{\Pi}^2(\mathbf{r}) - c_0^2 \left[\nabla \times \mathbf{A}(\mathbf{r}) \right]^2 \right\}, \tag{1.15}$$

where the canonical momentum field is defined as

$$\mathbf{\Pi}(\mathbf{r}) = \frac{\delta L}{\delta \dot{\mathbf{A}}(\mathbf{r})} = \varepsilon_0 \dot{\mathbf{A}}(\mathbf{r}). \tag{1.16}$$

Having derived the Hamiltonian, we can finally perform the canonical quantization. In order to do so, the Poisson brackets, given by

$$\left\{ A_i(\mathbf{r}), \Pi_j(\mathbf{r}') \right\} = \delta_{ij}^{\perp}(\mathbf{r} - \mathbf{r}'), \tag{1.17a}$$

$$\left\{ A_i(\mathbf{r}), A_j(\mathbf{r}') \right\} = \left\{ \Pi_i(\mathbf{r}), \Pi_j(\mathbf{r}') \right\} = 0, \tag{1.17b}$$

need to be replaced by commutators multiplied by the factor $\frac{1}{i\hbar}$,

$$\left[\hat{A}_i(\mathbf{r}), \hat{\Pi}_j(\mathbf{r}') \right] = i\hbar \delta_{ij}^{\perp}(\mathbf{r} - \mathbf{r}'), \tag{1.18a}$$

$$\left[\hat{A}_i(\mathbf{r}), \hat{A}_j(\mathbf{r}') \right] = \left[\hat{\Pi}_i(\mathbf{r}), \hat{\Pi}_j(\mathbf{r}') \right] = 0. \tag{1.18b}$$

Note that we have additionally promoted the fields $\mathbf{A}(\mathbf{r})$ and $\mathbf{\Pi}(\mathbf{r})$ to operators $\hat{\mathbf{A}}(\mathbf{r})$ and $\hat{\mathbf{\Pi}}(\mathbf{r})$ acting on a Hilbert space. Inserting Eqs. (1.2) and (1.4) (with $\phi(\mathbf{r}) = 0$ in the vacuum) in Eq. (1.15), the Hamiltonian can now be expressed through the electric and magnetic fields,

$$\hat{H} = \frac{\varepsilon_0}{2} \int \mathrm{d}^3 r \; \left[\hat{\mathbf{E}}^2(\mathbf{r}) + c_0^2 \hat{\mathbf{B}}^2(\mathbf{r}) \right]. \tag{1.19}$$

The Hamiltonian takes on the form of a harmonic oscillator. The commutator between the electric and magnetic field can be calculated from Eq. (1.18a),

$$\left[\hat{\mathbf{E}}(\mathbf{r}), \hat{\mathbf{B}}(\mathbf{r}') \right] = \frac{i\hbar}{\varepsilon_0} \nabla \times \delta(\mathbf{r} - \mathbf{r}'). \tag{1.20}$$

Here, we have used the relation $\nabla \times \delta^{\perp}(\mathbf{r}) = \nabla \times \delta(\mathbf{r})$, which is easily verifiable through Eq. (1.14).

The quantized version of the wave equation in Eq. (1.10) can now be derived from the operator version of Eq. (1.15). The time evolution of the operators $\hat{\mathbf{A}}(\mathbf{r})$ and $\hat{\mathbf{\Pi}}(\mathbf{r})$

in the Heisenberg picture is governed by their commutator with the Hamiltonian,

$$\dot{\hat{\mathbf{A}}}(\mathbf{r}) = \frac{1}{i\hbar}\left[\hat{\mathbf{A}}(\mathbf{r}), \hat{H}\right] = \frac{1}{\varepsilon_0}\hat{\mathbf{\Pi}}(\mathbf{r}) \tag{1.21a}$$

$$\dot{\hat{\mathbf{\Pi}}}(\mathbf{r}) = \frac{1}{i\hbar}\left[\hat{\mathbf{\Pi}}(\mathbf{r}), \hat{H}\right] = \frac{\varepsilon_0}{c_0^2}\nabla^2\hat{\mathbf{A}}(\mathbf{r}). \tag{1.21b}$$

Taking the derivative with respect to time of the first line and inserting the second line for the resulting operator $\dot{\hat{\mathbf{\Pi}}}(\mathbf{r})$ finally leads to the wave equation for the operator $\hat{\mathbf{A}}(\mathbf{r})$,

$$\left(\nabla^2 - \frac{1}{c_0^2}\frac{\partial^2}{\partial t^2}\right)\hat{\mathbf{A}}(\mathbf{r}) = 0. \tag{1.22}$$

Note that the only difference to Eq. (1.22) lies in the fact that the vector potential has been promoted to an operator. This equivalence is a result of the canonical quantization, which preserves the formal structure of the classical theory by replacing the Poisson brackets with commutators. Equivalent wave equations can also be obtained for the electric and magnetic field, using the Hamiltonian in Eq. (1.19).

1.1.3 Expansion in plane waves

In order to solve Eq. (1.22), we separate the variables,

$$\hat{\mathbf{A}}(\mathbf{r}, t) = \frac{1}{\sqrt{\varepsilon_0}}\sum_{\lambda}\sum_{\mathbf{k}}\boldsymbol{\epsilon}^{(\lambda)}(\mathbf{k})A_{\mathbf{k}}(\mathbf{r})\hat{q}_{\lambda,\mathbf{k}}(t), \tag{1.23}$$

where $\boldsymbol{\epsilon}^{(\lambda)}(\mathbf{k})$ is the polarization direction and λ denotes the two possible perpendicular polarization directions according to $\mathbf{k}\cdot\boldsymbol{\epsilon}^{(\lambda)}(\mathbf{k}) = 0$. Inserting Eq. (1.23) into Eq. (1.22) allows us to separate the spatial and the temporal part of the vector potential $\hat{\mathbf{A}}(\mathbf{r}, t)$, so that $A_{\mathbf{k}}(\mathbf{r})$ has to satisfy the Helmholtz equation

$$\left(\nabla^2 + \frac{\omega_{\mathbf{k}}^2}{c_0^2}\right)A_{\mathbf{k}}(\mathbf{r}) = 0 \tag{1.24}$$

and $\hat{q}_{\lambda,\mathbf{k}}(t)$ has to satisfy the equation for a harmonic oscillator,

$$\ddot{\hat{q}}_{\lambda,\mathbf{k}}(t) + \omega_{\mathbf{k}}^2\hat{q}_{\lambda,\mathbf{k}}(t) = 0. \tag{1.25}$$

Equation (1.24) can be solved by a plane-wave ansatz,

$$A_{\mathbf{k}}(\mathbf{r}) = \frac{1}{\sqrt{V}}e^{i\mathbf{k}\mathbf{r}}, \tag{1.26}$$

where the dispersion relation $\omega_{\mathbf{k}}^2 = c_0^2 k^2$ connects the wave vector to the angular frequency. Here, we have assumed that the vector potential is constrained to a box of Volume $V = L^3$. Enforcing periodic boundary conditions $\mathbf{A}(\mathbf{r} + \mathbf{L}) = \mathbf{A}(\mathbf{r})$ with $\mathbf{L} = L(n_1, n_2, n_3)^T$ leads to the discrete wave vectors

$$\mathbf{k} = \frac{2\pi}{L}(m_1, m_2, m_3)^T, \tag{1.27}$$

where n_i, m_i are integers. Note that the solutions $A_{\mathbf{k}}(\mathbf{r})$ form an orthonormal basis, i.e. $\int \mathrm{d}^3 r \; A_{\mathbf{k}}(\mathbf{r}) A^*_{\mathbf{k}'}(\mathbf{r}) = \delta_{\mathbf{k},\mathbf{k}'}$.

An identical wave equation as in Eq. (1.22) can be derived for the canonically conjugated field $\mathbf{\Pi}(\mathbf{r}, t)$. The corresponding solution can be calculated equivalently and is given by

$$\hat{\mathbf{\Pi}}(\mathbf{r}, t) = \sqrt{\varepsilon_0} \sum_{\lambda} \sum_{\mathbf{k}} \boldsymbol{\epsilon}^{(\lambda)}(\mathbf{k}) A^*_{\mathbf{k}}(\mathbf{r}) \hat{p}_{\lambda,\mathbf{k}}(t). \tag{1.28}$$

Comparing these two solutions to the commutators in Eqs. (1.18a) and (1.18b) then leads to the commutators for the two quadratures $\hat{q}_{\lambda,\mathbf{k}}$ and $\hat{p}_{\lambda,\mathbf{k}}$,

$$\left[\hat{q}_{\lambda,\mathbf{k}}, \hat{p}_{\lambda',\mathbf{k}'}\right] = i\hbar \delta_{\lambda,\lambda'} \delta_{\mathbf{k},\mathbf{k}'} \tag{1.29a}$$

$$\left[\hat{q}_{\lambda,\mathbf{k}}, \hat{q}_{\lambda',\mathbf{k}'}\right] = \left[\hat{p}_{\lambda,\mathbf{k}}, \hat{p}_{\lambda',\mathbf{k}'}\right] = 0. \tag{1.29b}$$

The Hamiltonian can be brought into its most simple form by introducing so-called annihilation and creation operators according to

$$\hat{q}_{\lambda,\mathbf{k}} = \sqrt{\frac{\hbar}{2\omega_{\mathbf{k}}}} \left(\hat{a}_{\lambda,\mathbf{k}} + \hat{a}^\dagger_{\lambda,-\mathbf{k}}\right), \tag{1.30a}$$

$$\hat{p}_{\lambda,\mathbf{k}} = i\sqrt{\frac{\hbar}{2\omega_{\mathbf{k}}}} \left(\hat{a}^\dagger_{\lambda,\mathbf{k}} - \hat{a}_{\lambda,-\mathbf{k}}\right). \tag{1.30b}$$

Comparison to Eqs. (1.29a) and (1.29b) leads to the commutators for the annihilation and creation operators,

$$\left[\hat{a}_{\lambda,\mathbf{k}}, \hat{a}^\dagger_{\lambda',\mathbf{k}'}\right] = \delta_{\lambda,\lambda'} \delta_{\mathbf{k},\mathbf{k}'} \tag{1.31a}$$

$$\left[\hat{a}_{\lambda,\mathbf{k}}, \hat{a}_{\lambda',\mathbf{k}'}\right] = \left[\hat{a}^\dagger_{\lambda,\mathbf{k}}, \hat{a}^\dagger_{\lambda',\mathbf{k}'}\right] = 0. \tag{1.31b}$$

Expressing Eqs. (1.23) and (1.28) in terms of the annihilation and creation operators,

the Hamiltonian can be expressed as

$$\hat{H} = \sum_{\lambda} \sum_{\mathbf{k}} \hbar\omega_{\mathbf{k}} \left(\hat{a}^{\dagger}_{\lambda,\mathbf{k}} \hat{a}_{\lambda,\mathbf{k}} + \frac{1}{2} \right). \tag{1.32}$$

The operators $\hat{a}_{\lambda,\mathbf{k}}$ and $\hat{a}^{\dagger}_{\lambda,\mathbf{k}}$ annihilate and create excitations of energy $\hbar\omega_{\mathbf{k}}$, respectively, which manifest in terms of photons. Therefore, the operators $\hat{a}_{\lambda,\mathbf{k}}$ and $\hat{a}^{\dagger}_{\lambda,\mathbf{k}}$ can also be thought of as annihilating or creating photons of polarization λ and wave vector $\mathbf{k}$, respectively.

Finally, the vector potential can be expressed through the annihilators and creators and its time dependence can be calculated using the Hamiltonian in Eq. (1.32). The result is given by

$$\hat{\mathbf{A}}(\mathbf{r}, t) = \sum_{\lambda} \sum_{\mathbf{k}} \sqrt{\frac{\hbar}{2\varepsilon_0 \omega_{\mathbf{k}} V}} \boldsymbol{\epsilon}^{(\lambda)}(\mathbf{k}) \left(\hat{a}_{\lambda,\mathbf{k}} e^{i(\mathbf{kr} - \omega_{\mathbf{k}} t)} + \hat{a}^{\dagger}_{\lambda,\mathbf{k}} e^{-i(\mathbf{kr} - \omega_{\mathbf{k}} t)} \right). \tag{1.33}$$

Recall that we have treated the case of the vector potential confined in a finite box of volume $V = L^3$. In order to obtain the vector potential of the free, unrestricted space, we need to let the dimensions of the box grow until it covers the entire space $L \to \infty$. In turn, this leads eventually to continuous wave vectors $\mathbf{k}$ [cf. Eq. (1.27)], so that the sum over the wave vectors has to be replaced by an integral, $\sum_{\mathbf{k}} \to \frac{V}{(2\pi)^3} \int \mathrm{d}^3 k$. This transformation from discrete to continuous modes also affects the annihilation and creation operators, which need to be replaced by $\hat{a}_{\lambda}(\mathbf{k}) = \sqrt{\frac{V}{(2\pi)^3}} \hat{a}_{\lambda,\mathbf{k}}$.

The vector potential of the free space is thus given by

$$\hat{\mathbf{A}}(\mathbf{r}, t) = \sum_{\lambda} \int \mathrm{d}^3 k \, \sqrt{\frac{\hbar}{2(2\pi)^3 \varepsilon_0 \omega_{\mathbf{k}}}} \boldsymbol{\epsilon}^{(\lambda)}(\mathbf{k}) \left(\hat{a}_{\lambda}(\mathbf{k}) e^{i(\mathbf{kr} - \omega_{\mathbf{k}} t)} + \hat{a}^{\dagger}_{\lambda}(\mathbf{k}) e^{-i(\mathbf{kr} - \omega_{\mathbf{k}} t)} \right). \tag{1.34}$$

The electric and magnetic fields are given by

$$\hat{\mathbf{E}}(\mathbf{r}, t) = i \sum_{\lambda} \int \mathrm{d}^3 k \, \sqrt{\frac{\hbar\omega_{\mathbf{k}}}{2(2\pi)^3 \varepsilon_0}} \boldsymbol{\epsilon}^{(\lambda)}(\mathbf{k}) \left(\hat{a}_{\lambda}(\mathbf{k}) e^{i(\mathbf{kr} - \omega_{\mathbf{k}} t)} - \hat{a}^{\dagger}_{\lambda}(\mathbf{k}) e^{-i(\mathbf{kr} - \omega_{\mathbf{k}} t)} \right), \tag{1.35a}$$

$$\hat{\mathbf{B}}(\mathbf{r}, t) = i \sum_{\lambda} \int \mathrm{d}^3 k \, \sqrt{\frac{\hbar}{2(2\pi)^3 \varepsilon_0 \omega_{\mathbf{k}}}} \mathbf{k} \times \boldsymbol{\epsilon}^{(\lambda)}(\mathbf{k}) \left(\hat{a}_{\lambda}(\mathbf{k}) e^{i(\mathbf{kr} - \omega_{\mathbf{k}} t)} - \hat{a}^{\dagger}_{\lambda}(\mathbf{k}) e^{-i(\mathbf{kr} - \omega_{\mathbf{k}} t)} \right). \tag{1.35b}$$

1.2 Paraxial approximation

The use of lasers in modern optics is ubiquitous. The expansion of the electric fields in Eqs. (1.35a) in terms of plane waves is the easiest one to derive but is oftentimes ill-suited to describe laser fields generated in real experiments. In this case, the field can be thought of as a beam, which is mainly propagating along a well-defined direction. The beam is being focused on a specific point along the propagation direction, so that the beam's cross-sectional area has its minimum in this region and widens outside of the focused interval.

1.2.1 Paraxial and one-dimensional wave equation

First, we decompose the vector $\mathbf{r} = (\mathbf{r}_\perp, r_\parallel)^T$ into a longitudinal part $r_\parallel$ and a transversal part $\mathbf{r}_\perp$. Since the beam is mainly propagating along one propagation direction ($r_\parallel$), we will factor out the main component of this propagation in terms of a plane wave in Eq. (1.34). This can be done by introducing the identity[14, 15]

$$\int_0^\infty \mathrm{d}k_0 \, \frac{e^{ik_0(r_\parallel - c_0 t)}}{e^{ik_0(r_\parallel - c_0 t)}} \delta[k_0 - f(\mathbf{k})] = 1 \tag{1.36}$$

into Eq. (1.34). The function $f(\mathbf{k})$ can be chosen completely arbitrary in this case. Using this identity, we can decompose the vector field according to

$$\hat{\mathbf{A}}(\mathbf{r}, t) = \int_0^\infty \mathrm{d}k_0 e^{ik_0(r_\parallel - c_0 t)} \hat{\mathbf{A}}_{k_0}(\mathbf{r}, t) + H.c. \tag{1.37}$$

Now, this ansatz can be inserted into the wave equation given in Eq. (1.22). We can then choose the form of the function $f(\mathbf{k})$ in Eq. (1.36) such that the envelope of the plane wave $\hat{\mathbf{A}}_{k_0}(\mathbf{r}, t)$ in Eq. (1.37) satisfies the paraxial wave equation

$$\left(\nabla_\perp^2 + i2k_0 \frac{\partial}{\partial r_\parallel} \right) \hat{\mathbf{A}}_{k_0}(\mathbf{r}, t) = 0, \tag{1.38}$$

where $\nabla_\perp$ denotes the ∇ operator in the transversal plane. This results in the function

$$f(\mathbf{k}) = \frac{k_\parallel + \sqrt{k_\parallel^2 + 2k_\perp^2}}{2}, \tag{1.39}$$

where we have split the wave vector $\mathbf{k} = (\mathbf{k}_\perp, k_\parallel)^T$ into a part longitudinal to the propagation direction ($k_\parallel$) and a part transversal to it ($\mathbf{k}_\perp$), analogously to $\mathbf{r}$.

The envelope of the plane wave $\hat{\mathbf{A}}_{k_0}(\mathbf{r},t)$ is then given by

$$\hat{\mathbf{A}}_{k_0}(\mathbf{r},t) = \sum_{\lambda} \int \mathrm{d}^2 k_\perp \sqrt{\frac{\hbar(1+\vartheta^2)}{2(2\pi)^3 \varepsilon_0 c_0 k_0 \sqrt{1+\vartheta^4}}} \boldsymbol{\epsilon}^{(\lambda)}[\mathbf{k}_\perp, k_0(1-\vartheta^2)] \\ \hat{a}_\lambda(\mathbf{k}_\perp, k_0) e^{i(\mathbf{k}_\perp \mathbf{r}_\perp - k_0 \vartheta^2 r_\parallel - c_0 k_0 [\sqrt{1+\vartheta^4}-1])}, \tag{1.40}$$

where $\vartheta = \frac{k_\perp}{\sqrt{2}k_0}$ is a measure of the paraxiality, i.e. the degree to which the propagation does not align with the main propagation direction along the $k_\parallel$-axis.

The spatial modes that solve the paraxial wave equation, given in Eq. (1.38), belong to the family of Gaussian beams. The precise modal structure of these beams is determined by the symmetries underlying their generation process. In cavities with a rectangular symmetry, Hermite-Gaussian modes are used, which consist of the product of two independent spatial modes for each perpendicular direction. If the generated beam possesses elliptical symmetry, Ince-Gaussian modes can be used to describe the spatial behaviour of the beam. In the following, we want to focus on the (2D) rotationally symmetric case, given by Laguerre-Gaussian modes.

1.2.2 Laguerre-Gaussian modes

The Laguerre-Gaussian modes are given by

$$\mathrm{LG}_{lp}(r_\perp, \varphi, r_\parallel; k_0) = \sqrt{\frac{2p!}{\pi(|l|+p)!}} \frac{1}{w(r_\parallel)} \left(\frac{\sqrt{2} r_\perp}{w(r_\parallel)}\right)^{|l|} \mathrm{L}_p^{|l|}\left(\frac{2r_\perp^2}{w^2(r_\parallel)}\right) \\ \times \exp\left[-\frac{r_\perp^2}{w^2(r_\parallel)} + il\varphi + i\frac{k_0 r_\perp^2}{2\mathcal{R}(r_\parallel)} + i\Phi_\mathrm{G}(r_\parallel)\right]. \tag{1.41}$$

Here, we express the transverse vector $\mathbf{r}_\perp = r_\perp(\cos\varphi, \sin\varphi)^T$ in polar coordinates. $w(r_\parallel) = w_0\sqrt{1 + r_\parallel^2/l_R^2(k_0)}$ denotes the transverse mode radius at the longitudinal position $r_\parallel$, with w_0 as the waist size of the beam at the most focused point $r_\parallel = 0$. The Rayleigh range $l_R(k_0) = k_0 w_0^2/2$ describes the point at which the beam's waist size is increased by a factor of $\sqrt{2}$ with respect to w_0. $\mathcal{R}(r_\parallel) = r_\parallel\left[1 + l_R^2(k_0)/r_\parallel^2\right]$ is the phase-front radius and $\Phi_\mathrm{G} = -(2p + |l| + 1)\arctan(r_\parallel/w_0)$ is the Gouy phase. The Laguerre polynomials $\mathrm{L}_p^{|l|}(x)$ are given by

$$\mathrm{L}_p^{|l|}(x) = \sum_{n=0}^{p} (-1)^n \frac{(|l|+p)!}{(p-n)!(|l|+n)!n!} x^n, \tag{1.42}$$

where l are integers and p are positive integers (both including 0) [16].

The normalized Fourier transforms of the Laguerre Gaussian modes $\mathcal{LG}_{lp}(\mathbf{k}_\perp)$ at $r_\parallel = 0$ are given by [17]

$$\begin{aligned}\mathcal{LG}_{lp}(k_\perp,\phi) &= \frac{1}{2\pi}\int \mathrm{d}^2 r_\perp \mathrm{LG}_{lp}(r_\perp,\varphi,0;k_0)e^{i\mathbf{k}_\perp\mathbf{r}_\perp} \\ &= \sqrt{\frac{w_0^2 p!}{2\pi(|l|+p)!}}\left(\frac{w_0 k_\perp}{\sqrt{2}}\right)^{|l|}\mathrm{L}_p^{|l|}\left(\frac{w_0^2k_\perp^2}{2}\right) \\ &\qquad\times\exp\left(-\frac{w_0^2k_\perp^2}{4}+il\phi+i\frac{\pi}{2}(|l|+2p)\right).\end{aligned} \tag{1.43}$$

Here, we have expressed the transversal vector $\mathbf{k}_\perp = k_\perp(\cos\phi,\sin\phi)^T$ in polar coordinates. Both the Laguerre-Gaussian modes and their Fourier transforms (at $r_\parallel = 0$) form an orthonormal basis, i.e.

$$\int \mathrm{d}^2 r_\perp \mathrm{LG}^*_{lp}(r_\perp,\varphi,r_\parallel;k_0)\mathrm{LG}_{l'p'}(r_\perp,\varphi,r_\parallel;k_0) = \delta_{l,l'}\delta_{p,p'}, \tag{1.44a}$$

$$\sum_{l,p}\mathrm{LG}^*_{lp}(r_\perp,\varphi,r_\parallel;k_0)\mathrm{LG}_{lp}(r'_\perp,\varphi',r_\parallel;k_0) = \delta(\mathbf{r}_\perp-\mathbf{r}'_\perp), \tag{1.44b}$$

$$\int \mathrm{d}^2 k_\perp \mathcal{LG}^*_{lp}(k_\perp,\phi)\mathcal{LG}_{l'p'}(k_\perp,\phi) = \delta_{l,l'}\delta_{p,p'}, \tag{1.44c}$$

$$\sum_{l,p}\mathcal{LG}^*_{lp}(k_\perp,\phi)\mathcal{LG}_{lp}(k'_\perp,\phi') = \delta(\mathbf{k}_\perp-\mathbf{k}'_\perp). \tag{1.44d}$$

The orthogonality of $\mathcal{LG}_{lp}(k_\perp,\phi)$ in Eq. (1.44d) can be used to decompose the plane wave $e^{i(\mathbf{k}_\perp\mathbf{r}_\perp-k_0\vartheta^2 r_\parallel)}$ into Laguerre-Gaussian modes through

$$\begin{aligned}e^{i(\mathbf{k}_\perp\mathbf{r}_\perp-k_0\vartheta^2 r_\parallel)} &= \int \mathrm{d}\mathbf{k}'_\perp e^{i(\mathbf{k}'_\perp\mathbf{r}_\perp-k_0\vartheta'^2 r_\parallel)}\delta(\mathbf{k}_\perp-\mathbf{k}'_\perp) \\ &= \int \mathrm{d}\mathbf{k}'_\perp e^{i(\mathbf{k}'_\perp\mathbf{r}_\perp-k_0\vartheta'^2 r_\parallel)}\sum_{l,p}\mathcal{LG}^*_{lp}(k_\perp,\phi)\mathcal{LG}_{lp}(k'_\perp,\phi') \\ &= \sum_{l,p}\mathcal{LG}^*_{lp}(k_\perp,\phi)\int \mathrm{d}\mathbf{k}'_\perp e^{i(\mathbf{k}'_\perp\mathbf{r}_\perp-k_0\vartheta'^2 r_\parallel)}\mathcal{LG}_{lp}(k'_\perp,\phi') \\ &= 2\pi\sum_{l,p}\mathcal{LG}^*_{lp}(k_\perp,\phi)\mathrm{LG}_{lp}(r_\perp,\varphi,r_\parallel;k_0).\end{aligned} \tag{1.45}$$

Here, we have used the propagation formula of the angular spectrum in the last step, which connects the Laguerre-Gaussian modes at any point $r_\parallel$ to their Fourier transform at $r_\parallel = 0$ by noting that the effect of the propagation is simply given by a wave-vector dependent phase shift [18].

The derived identity can be used to express the envelope $\mathbf{A}_{k_0}(\mathbf{r},t)$ in terms of the

better suited Laguerre-Gaussian modes,

$$\hat{\mathbf{A}}_{k_0}(\mathbf{r},t) = \sum_\lambda \int \mathrm{d}^2 k_\perp \sqrt{\frac{\hbar(1+\vartheta^2)}{4\pi\varepsilon_0 c_0 k_0 \sqrt{1+\vartheta^4}}} \boldsymbol{\epsilon}^{(\lambda)}[\mathbf{k}_\perp, k_0(1-\vartheta^2)] \hat{a}_\lambda(\mathbf{k}_\perp, k_0) \sum_{l,p} \mathcal{LG}^*_{lp}(k_\perp,\phi) \mathrm{LG}_{lp}(r_\perp,\varphi,r_\parallel;k_0) e^{-ic_0 k_0[\sqrt{1+\vartheta^4}-1]}. \tag{1.46}$$

Note that this decomposition in terms of the Laguerre-Gaussian modes [if inserted into Eq. (1.37)] is identical to the decomposition in terms of plane waves according to Eq. (1.34).

Equation (1.46) can be simplified significantly if we enforce the paraxial approximation $\vartheta \ll 1$, i.e. we assume that the field is mainly propagating along one direction along the $r_\parallel$-axis. In this case, the absolute value of the wave vector and thus the frequency $\omega_{\mathbf{k}}$ is basically given by $k \approx k_0$ and we can neglect the dependence on ϑ in Eq. (1.46). This also means that the polarization vectors $\boldsymbol{\epsilon}^{(\lambda)}[\mathbf{k}_\perp, k_0(1-\vartheta^2)] \approx \boldsymbol{\epsilon}^{(\lambda)}$ can be viewed as independent of $\mathbf{k}$, so that just two mutually orthogonal polarization vectors in the transversal plane of the propagation direction need to be selected. This leads to

$$\hat{\mathbf{A}}_{k_0}(\mathbf{r}) = \sum_\lambda \sqrt{\frac{\hbar}{4\pi\varepsilon_0 c_0 k_0}} \boldsymbol{\epsilon}^{(\lambda)} \sum_{l,p} \mathrm{LG}_{lp}(r_\perp,\varphi,r_\parallel;k_0) \hat{a}_{\lambda lp}(k_0). \tag{1.47}$$

Here, we have defined the annihilation operators in the basis of the Laguerre-Gaussian modes,

$$\hat{a}_{\lambda lp}(k_0) = \int \mathrm{d}^2 k_\perp \mathcal{LG}^*_{lp}(k_\perp,\phi) \hat{a}_\lambda(\mathbf{k}_\perp, k_0), \tag{1.48}$$

which, according to Eq. (1.44d), satisfy the commutation relations $\left[\hat{a}_{\lambda lp}(k_0), \hat{a}^\dagger_{\lambda' l' p'}(k_0)\right] = \delta_{\lambda,\lambda'}\delta_{l,l'}\delta_{p,p'}\delta(k_0 - k_0')$. The operator $\hat{a}_{\lambda lp}(k_0)$ now annihilates a photon of polarization λ, wave vector k_0 and transverse spatial mode $\mathrm{LG}_{lp}(r_\perp,\varphi,r_\parallel;k_0)$.

Finally, the vector potential field in the paraxial quantization is given by

$$\hat{\mathbf{A}}(\mathbf{r},t) = \sum_\lambda \int_0^\infty \mathrm{d}k \sqrt{\frac{\hbar}{4\pi\varepsilon_0\omega_k}} \boldsymbol{\epsilon}^{(\lambda)} \sum_{l,p} \mathrm{LG}_{lp}(r_\perp,\varphi,r_\parallel;k) \hat{a}_{\lambda lp}(k) e^{ik(r_\parallel - c_0 t)} + H.c.. \tag{1.49}$$

An additional simplification can be made by assuming that the field is in the fundamental Laguerre-Gaussian mode LG_{00} and the cross-sectional area of the beam is broad enough that it can be effectively treated like a plane wave again, extending infinitely

in the transversal plane. In this case, the Laguerre-Gaussian can be replaced by an effective cross-sectional area A, $\mathrm{LG}_{00}(r_\perp, \varphi, r_\parallel; k_0) \to \frac{1}{\sqrt{A}}$. This results in

$$\hat{\mathbf{A}}(r_\parallel, t) = \sum_\lambda \int_0^\infty \mathrm{d}k \, \sqrt{\frac{\hbar}{4\pi\varepsilon_0 A \omega_{\mathbf{k}}}} \boldsymbol{\epsilon}^{(\lambda)} \hat{a}_\lambda(k) e^{i(kr_\parallel - \omega_k t)} + H.c., \tag{1.50}$$

where $\left[\hat{a}_\lambda(k), \hat{a}_\lambda^\dagger(k)\right] = \delta(k - k')$.

In this thesis, we are interested in the coupling of the electric field to nonlinear media. Furthermore, it is often more convenient to describe the annihilation and creation operators in dependence on the angular frequency ω. When changing their dependence from k to ω, we need to ensure that the commutation relations are not changed,

$$\left[\hat{a}_\lambda(k), \hat{a}_\lambda^\dagger(k')\right] = \delta(k - k') = c_0 \delta(\omega - \omega') = c_0 \left[\hat{a}_\lambda(\omega), \hat{a}_\lambda^\dagger(\omega')\right], \tag{1.51}$$

which results in the identity $\hat{a}_\lambda(k) = \sqrt{c_0}\hat{a}_\lambda(\omega)$. The transformation for the annihilation operator in the Laguerre-Gaussian basis is identical.

The electric field in the paraxial approximation is given by

$$\hat{\mathbf{E}}(\mathbf{r}, t) = i \sum_\lambda \int_0^\infty \mathrm{d}\omega \, \sqrt{\frac{\hbar\omega}{4\pi\varepsilon_0 c_0 A}} \boldsymbol{\epsilon}^{(\lambda)} \sum_{l,p} \mathrm{LG}_{lp}(r_\perp, \varphi, r_\parallel; k_\omega) \hat{a}_{\lambda lp}(\omega) e^{i(k_\omega r_\parallel - \omega t)} + H.c.. \tag{1.52}$$

In the one-dimensional plane wave approximation, the electric field is given by

$$\hat{\mathbf{E}}(r_\parallel, t) = i \sum_\lambda \int_0^\infty \mathrm{d}\omega \, \sqrt{\frac{\hbar\omega}{4\pi\varepsilon_0 c_0 A}} \boldsymbol{\epsilon}^{(\lambda)} \hat{a}_\lambda(\omega) e^{i(k_\omega r_\parallel - \omega t)} + H.c.. \tag{1.53}$$

1.3 Field quantization in linear media

We have so far assumed that the electromagnetic fields are propagating in the vacuum. In the presence of few charged particles, the quantization for the free electromagnetic field still holds as a good approximation and corrections to the fields due to the charged particles can be calculated perturbatively. If the density of the charged particles grows, a perturbative approach becomes intractable. In this case, the quantization of the electromagnetic field needs to take into account the matter degrees of freedom[1]. The quantization of the electromagnetic field can then be performed in two different ways.

[1]Note that in this thesis, we will only consider media with linear responses for the quantization, since the quantization of the electromagnetic field in nonlinear media is still an open problem in modern physics.

The first approach is the microscopic one. Here, the Lagrangian of the combined system of electromagnetic fields and the matter is formulated, which can then be quantized canonically by replacing the Poisson brackets of conjugated variables with commutators. This does only provide a formal quantization of the system. The obtained Hamiltonian then needs to be diagonalized according to the specific characteristics of the medium under study. In this sense, this quantization procedure is medium specific [19, 20].

The second approach is given by a macroscopic description, where the quantization procedure is performed under two main assumptions. First, the classical Maxwell equations describing the evolution of the electromagnetic field must also be obeyed by its quantized counterpart. Second, the electric and magnetic response of the medium can be described through linear susceptibilities and the electromagnetic quantum fluctuations satisfy the fluctuation-dissipation theorem describing the connection between the absorption rate of a medium and its thermal fluctuations. This approach is more general and can describe any material whose electromagnetic response can be described by linear susceptibilities [21]. Both of these approaches lead to approximately the same results.

Following the second approach, the starting point is given by the quantized macroscopic Maxwell equations in case of absent free charges and currents,

$$\nabla \cdot \hat{\mathbf{D}}(\mathbf{r}, t) = 0, \tag{1.54a}$$

$$\nabla \cdot \hat{\mathbf{H}}(\mathbf{r}, t) = 0, \tag{1.54b}$$

$$\nabla \times \hat{\mathbf{E}}(\mathbf{r}, t) + \frac{\partial}{\partial t}\hat{\mathbf{B}}(\mathbf{r}, t) = 0, \tag{1.54c}$$

$$\nabla \times \hat{\mathbf{H}}(\mathbf{r}, t) - \frac{\partial}{\partial t}\hat{\mathbf{D}}(\mathbf{r}, t) = 0. \tag{1.54d}$$

Here, $\hat{\mathbf{H}}(\mathbf{r}, t) = \hat{\mathbf{B}}(\mathbf{r}, t)/\mu_0$ is identical to the magnetic field if the magnetization of the medium can be neglected and $\hat{\mathbf{D}}(\mathbf{r}, t) = \varepsilon_0\hat{\mathbf{E}}(\mathbf{r}, t) + \hat{\mathbf{P}}(\mathbf{r}, t)$ is the displacement field given by the sum of the electric field and the polarization field $\hat{\mathbf{P}}(\mathbf{r}, t)$.

In a homogeneous, isotropic medium with a local response, the polarization operator is given by[21]

$$\hat{\mathbf{P}}(\mathbf{r}, t) = \varepsilon_0 \int \mathrm{d}\tau \chi^{(1)}(\tau)\hat{\mathbf{E}}(\mathbf{r}, t - \tau) + \hat{\mathbf{P}}_N(\mathbf{r}, t). \tag{1.55}$$

The field $\hat{\mathbf{P}}_N(\mathbf{r}, t)$ describes the noise polarization accounting for the fluctuations inside the medium. It ensures that the fluctuation-dissipation theorem is obeyed and is therefore essentially given by the imaginary part of the linear susceptibility $\chi^{(1)}(\tau)$. If

we assume that the frequencies of the fields we are interested in are far away from any resonances of the medium, we can ignore the imaginary part of $\chi^{(1)}(\tau)$ and hence the contribution of $\hat{\mathbf{P}}_N(\mathbf{r},t)$ in Eq. (1.55). This allows us to describe the displacement field $\hat{\mathbf{D}}(\mathbf{r},t)$ as

$$\hat{\mathbf{D}}(\mathbf{r},t) = \varepsilon_0 \int \mathrm{d}\tau \ \left[\delta(\tau) + \chi^{(1)}(\tau)\right] \hat{\mathbf{E}}(\mathbf{r}, t-\tau). \tag{1.56}$$

The wave equation for the electric field can now be derived in a similar way to the wave equation for the vector potential in Sec. 1.1,

$$\nabla^2 \hat{\mathbf{E}}(\mathbf{r},t) - \frac{1}{c_0^2}\frac{\partial}{\partial t^2}\hat{\mathbf{E}}(\mathbf{r},t) = \frac{1}{\varepsilon_0 c_0^2}\frac{\partial^2}{\partial t^2}\hat{\mathbf{P}}(\mathbf{r},t). \tag{1.57}$$

Analogously to the classical case, Eq. (1.55) can be inserted into the wave equation above, which ultimately leads to the same wave equation as for the vacuum case, with the only difference that the dispersion relation has been changed to $k_\omega = n_\omega \omega / c_0$ with $n_\omega^2 = 1 + \int_{-\infty}^{\infty} \mathrm{d}t \ \chi^{(1)}(t) e^{i\omega t}$. This means that the general form of the decomposition of the electric field into annihilation and creation operators remains unchanged. In case of the one dimensional solution, in Eq. (1.53), the precise form of the electric field can be found by first making the ansatz[12]

$$\hat{\mathbf{E}}(r_\parallel, t) = i \sum_\lambda \int_0^\infty \mathrm{d}\omega \ f(\omega) \boldsymbol{\epsilon}^{(\lambda)} \hat{a}_\lambda(\omega) e^{i(k_\omega r_\parallel - \omega t)} + H.c.. \tag{1.58}$$

Likewise, the magnetic field is then given by

$$\hat{\mathbf{B}}(r_\parallel, t) = i \sum_\lambda \int_0^\infty \mathrm{d}\omega \ f(\omega) \frac{n(\omega)}{c_0} \boldsymbol{\epsilon}^{(\lambda)} \hat{a}_\lambda(\omega) e^{i(k_\omega r_\parallel - \omega t)} + H.c., \tag{1.59}$$

and the displacement field is given by

$$\hat{\mathbf{D}}(r_\parallel, t) = i\varepsilon_0 \sum_\lambda \int_0^\infty \mathrm{d}\omega \ f(\omega) n^2(\omega) \boldsymbol{\epsilon}^{(\lambda)} \hat{a}_\lambda(\omega) e^{i(k_\omega r_\parallel - \omega t)} + H.c.. \tag{1.60}$$

In order to find the correct mode amplitude $f(\omega)$, the rate of change of the electro-

magnetic field energy operator $\hat{W}(r_\parallel, t)$ can be calculated[2], which is given by

$$\begin{aligned}\frac{\partial \hat{W}(r_\parallel,t)}{\partial t} = \hat{\mathbf{E}}^{(-)}(r_\parallel,t)\frac{\partial \hat{\mathbf{D}}^{(+)}(r_\parallel,t)}{\partial t} + \frac{\partial \hat{\mathbf{D}}^{(-)}(r_\parallel,t)}{\partial t}\hat{\mathbf{E}}^{(+)}(r_\parallel,t) \\ + \frac{\varepsilon_0}{c_0^2}\hat{\mathbf{B}}^{(-)}(r_\parallel,t)\frac{\partial \hat{\mathbf{B}}^{(+)}(r_\parallel,t)}{\partial t} + \frac{\partial \hat{\mathbf{B}}^{(-)}(r_\parallel,t)}{\partial t}\hat{\mathbf{B}}^{(+)}(r_\parallel,t).\end{aligned} \tag{1.61}$$

Here, we have used the notation introduced by Glauber, where $\hat{\mathbf{E}}^{(+)}(r_\parallel, t)$ [$\hat{\mathbf{E}}^{(-)}(r_\parallel, t)$] denotes the annihilation [creation] part of the electric field operator, so that $\hat{\mathbf{E}}(r_\parallel, t) = \hat{\mathbf{E}}^{(-)}(r_\parallel, t) + \hat{\mathbf{E}}^{(+)}(r_\parallel, t)$ (and analogously for all other fields).

Now, $f(\omega)$ can be found by inserting Eqs. (1.58), (1.59), (1.60) into Eq. (1.61) and choosing $f(\omega)$ such that the total energy is again given by that of a continuous-mode set of uncoupled harmonic oscillators

$$A\int \mathrm{d}r_\parallel\ \hat{W}(r_\parallel,t) = \sum_\lambda \int_0^\infty \mathrm{d}\omega\ \hbar\omega\ \hat{a}_\lambda^\dagger(\omega)\hat{a}_\lambda(\omega). \tag{1.62}$$

Assuming a slowly changing refractive index n_ω, so that $\frac{\mathrm{d}k_\omega}{\mathrm{d}\omega} \approx \frac{n_\omega}{c_0}$, then leads to

$$f(\omega) = \sqrt{\frac{\hbar}{4\pi\varepsilon c_0 n_\omega A}}. \tag{1.63}$$

Therefore, the mode amplitude of the electric field inside a transparent (i.e. nonabsorbing), homogeneous medium just needs to be divided by the factor $\sqrt{n_\omega}$ to obtain the correct quantization. The same transformation also holds for the electric field operator in the paraxial quantization.

1.4 Nonlinear optics

From the very start, the field of nonlinear optics has been closely related to laser physics. It was the invention of the laser in 1960 which enabled one of the first observations of nonlinear effects in terms of two-photon absorption and second-harmonic generation. Previous light sources were simply not able to produce high enough intensities to drive nonlinear effects. Since their discovery, nonlinear effects have become irreplaceable in quantum optics due to their role in the generation of squeezed states and entangled photons through processes like parametric downconversion [22–24] or four-wave mixing [25]. Resonances of the nonlinear matter would only complicate the description of the process and lead to absorption. Thus, the nonlinear matter is operated in the

[2]Its classical counterpart can be calculated by the Poynting theorem $-\nabla\cdot\mathbf{S} = \frac{\partial W}{\partial t}$ and the classical macroscopic Maxwell equations given in Eqs. (1.54a), (1.54b), (1.54c), and (1.54d).

off-resonant regime and merely acts as a kind of catalyst for the effective interaction between the electric fields.

In the field of classical nonlinear spectroscopy, nonlinear effects are used to analyse the response and characteristics of the resonances of various kinds of materials. With the impressive advances in the control and generation of nonclassical states of light, spectroscopy with quantum light has emerged as a novel and exciting field [26]. In contrast to classical light, quantum states of light exhibit a larger number of degrees of freedom, therefore extending the possibilities of classical spectroscopic tools. The matter response to quantum light can be separated into two types. In the first type, the response of matter is described by causal susceptibilities also observable by classical fields. Here, the quantum effects of the radiation states can be exploited to enhance the sensitivity of certain measurements. In the second type, entanglement between the matter and the quantum states of the light is taken into account. The matter response is described by noncausal susceptibilities that have no classical counterpart [27–29]. This truly takes advantage of the enhanced degrees of freedom of quantum states and demonstrates the potential of spectroscopic techniques employing quantum light.

1.4.1 Superoperator formalism and Liouville space

The superoperator formalism describes the evolution of the observable of interest in the Liouville space [13]. Within this framework, we associate plus- and minus-type superoperators with any ordinary operator $\hat{A}$ which are defined by their action on an arbitrary operator $\hat{X}$,

$$\hat{A}_+\hat{X} = \frac{1}{2}\{\hat{A},\hat{X}\} = \frac{1}{2}\left(\hat{A}\hat{X} + \hat{X}\hat{A}\right), \tag{1.64a}$$

$$\hat{A}_-\hat{X} = [\hat{A},\hat{X}] = \hat{A}\hat{X} - \hat{A}\hat{X}. \tag{1.64b}$$

Operators $\hat{X}$ take on the role of states in the Liouville space and their corresponding superoperators $\hat{X}_\pm$ function as operators acting on the states of the Liouville space. This enables the description of the density matrix in terms of a state in the Liouville space. The formal solution to its time evolution according to the Liouville-von Neumann equation

$$\frac{\partial}{\partial t}\hat{\rho}(t) = -\frac{i}{\hbar}\left[\hat{H}(t),\hat{\rho}(t)\right] \tag{1.65}$$

can then be calculated equivalently to the formal solution of the time evolution of the quantum state in the Hilbert space.

Hilbert space		**Liouville space**
$\frac{\partial}{\partial t}\|\psi(t)\rangle = -\frac{i}{\hbar}\hat{H}(t)\|\psi(t)\rangle$	$\leftrightarrow$	$\frac{\partial}{\partial t}\hat{\rho}(t) = -\frac{i}{\hbar}\hat{H}_-(t)\hat{\rho}(t)$
$\|\psi(t)\rangle = \mathcal{T}\exp\left(-\frac{i}{\hbar}\int_{-\infty}^{t}\mathrm{d}\tau\hat{H}(\tau)\right)\|\psi(0)\rangle$	$\leftrightarrow$	$\hat{\rho}(t) = \mathcal{T}\exp\left(-\frac{i}{\hbar}\int_{-\infty}^{t}\mathrm{d}\tau\hat{H}_-(\tau)\right)\hat{\rho}(0)$

Here, $\mathcal{T}$ denotes the time-ordering operator,

$$\mathcal{T}\exp\left(-\frac{i}{\hbar}\int_{-\infty}^{t}\mathrm{d}\tau\hat{H}_-(\tau)\right) = 1 + \sum_{n=1}^{\infty}\left(\frac{-i}{\hbar}\right)^n\int_{-\infty}^{t}\mathrm{d}\tau_n\int_{-\infty}^{\tau_n}\mathrm{d}\tau_{n-1}...\int_{-\infty}^{\tau_2}\mathrm{d}\tau_1 \times \hat{H}_-(\tau_n)\hat{H}_-(\tau_{n-1})...\hat{H}_-(\tau_1). \tag{1.66}$$

1.4.2 Electric susceptibilities

In Sec. (1.3), Eq. (1.57) showed how the effect of a material on the electric field is described by the polarization $\hat{\mathbf{P}}(\mathbf{r},t)$, entering as a source term in its wave equation. Similar to the first term in Eq. (1.55) for the linear response, the nonlinear polarization can be described by higher order terms of the electric fields, contracted with the respective nonlinear susceptibilities. Here, an introduction to the description of the response of a single molecule to electric fields in terms of these electric susceptibilities is given. We will employ the superoperator approach, formulated in the Liouville space, to show how the response can be expanded into powers of the electric field, giving rise to different orders of susceptibilities $\chi^{(n)}$, which describe $n+1$ wave-mixing processes.

This section treats the case of the interaction of the electric field with a single molecule, located at $\mathbf{r}$, whose size is much smaller than the typical wavelengths of the involved electric fields. The interaction can then be described by the dipole approximation. In this case, the Hamiltonian in the interaction picture is given by

$$\hat{H}_{\mathrm{int}}(t) = -\hat{\mathcal{E}}(\mathbf{r},t)\hat{\mathcal{V}}(t). \tag{1.67}$$

$\hat{\mathcal{E}}(\mathbf{r},t) = \hat{E}^{(+)}(\mathbf{r},t) + \hat{E}^{(-)}(\mathbf{r},t)$ is the electric field operator at the position of the molecule $\mathbf{r}$. Throughout this thesis, we will use curved letters like $\hat{\mathcal{E}}(\mathbf{r},t)$ $[\hat{\mathcal{P}}(\mathbf{r},t)]$ to denote the entire Hermitian electric field [polarization] operator. In contrast, regular letters $\hat{E}(\mathbf{r},t)$ $[\hat{P}(\mathbf{r},t)]$ will be used to denote their respective annihilation part, i.e. $\hat{E}^{(+)}(\mathbf{r},t) \equiv \hat{E}(\mathbf{r},t)$ $[\hat{P}^{(+)}(\mathbf{r},t) \equiv \hat{P}(\mathbf{r},t)]$ and $\hat{E}^{(-)}(\mathbf{r},t) \equiv \hat{E}^{\dagger}(\mathbf{r},t)$ $[\hat{E}^{(-)}(\mathbf{r},t) \equiv \hat{E}^{\dagger}(\mathbf{r},t)]$. This is done to avoid possible confusions with the superoperator indices. The dipole operator in the interaction picture $\hat{\mathcal{V}}(t)$ is given by

$$\hat{\mathcal{V}}(t) = \hat{G}^{\dagger}(t)\hat{\mathcal{V}}\hat{G}(t). \tag{1.68}$$

The Green's function $\hat{G}(t) = \exp\left[-\frac{i}{\hbar}\hat{H}_{\mathrm{mat}}\ t\right]$ describes the free temporal evolution of the dipole operator in terms of the time-independent Hamiltonian $\hat{H}_{\mathrm{mat}}$ of the molecule.

Usually, the field and matter degrees of freedom are initially independent of one another, so that the initial density matrix is given by the tensor product of the density matrix for photons and the density matrix for the field,

$$\hat{\rho}_{\mathrm{in}} = \hat{\rho}_{\mathrm{field}} \otimes \hat{\rho}_{\mathrm{mat}}. \tag{1.69}$$

Furthermore, the density matrix for the matter is assumed to be in thermal equilibrium, so that it does not evolve in time with respect to its free Hamiltonian, $\hat{\rho}_{\mathrm{mat}}(t) = \hat{G}^{\dagger}(t)\hat{\rho}_{\mathrm{mat}}\hat{G}(t) = \hat{\rho}_{\mathrm{mat}}$.

In Liouville space, the evolution of the density matrix is then given by

$$\hat{\rho}(t) = \mathcal{T}\exp\left(-\frac{i}{\hbar}\int_{-\infty}^{t}\mathrm{d}\tau\hat{H}_{\mathrm{int},-}(\tau)\right)\hat{\rho}_{\mathrm{in}}. \tag{1.70}$$

The superoperator $\hat{H}_{\mathrm{int},-}(\tau)$ can be expressed as

$$\hat{H}_{\mathrm{int},-}(t) = -\left[\hat{\mathcal{E}}_{+}(\mathbf{r},t)\hat{\mathcal{V}}_{-}(t) + \hat{\mathcal{E}}_{-}(\mathbf{r},t)\hat{\mathcal{V}}_{+}(t)\right], \tag{1.71}$$

since the operators $\hat{\mathcal{E}}(\mathbf{r},t)$ and $\hat{\mathcal{V}}(t)$ commute. The superoperator $\hat{\mathcal{V}}_{\pm}(t)$ is defined analogously to its operator counterpart in Eq. (1.68) and is given by

$$\hat{\mathcal{V}}_{\pm}(t) = \hat{\mathcal{G}}^{\dagger}(t)\hat{\mathcal{V}}_{\pm}\hat{\mathcal{G}}(t), \tag{1.72}$$

with $\hat{\mathcal{G}}(t) = \exp\left[-\frac{i}{\hbar}\hat{H}_{\mathrm{mat},-}\ t\right]$.

Given a signal $\hat{\mathcal{S}}$ specified by the measured observable in the experiment, we can now calculate the corresponding expectation value,

$$\left\langle\hat{\mathcal{S}}(t)\right\rangle = \mathrm{tr}\left\{\hat{\mathcal{S}}\mathcal{T}\exp\left(-\frac{i}{\hbar}\int_{-\infty}^{t}\mathrm{d}\tau\hat{H}_{\mathrm{int},-}(\tau)\right)\hat{\rho}_{\mathrm{in}}\right\} \tag{1.73}$$

$$= -\frac{i}{\hbar}\int_{-\infty}^{t}\mathrm{d}\tau\ \mathrm{tr}\left\{\mathcal{T}\hat{\mathcal{S}}\hat{H}_{\mathrm{int},-}(\tau)\exp\left(-\frac{i}{\hbar}\int_{-\infty}^{\tau}\mathrm{d}\tau'\hat{H}_{\mathrm{int},-}(\tau')\right)\hat{\rho}_{\mathrm{in}}\right\}, \tag{1.74}$$

where we have simply written out the final time integration in the second line and assumed that the initial expectation value of the signal $\mathrm{tr}\left\{\hat{\mathcal{S}}\hat{\rho}_{\mathrm{in}}\right\}$ vanishes. If the signal only acts on the field degrees of freedom (as is usual in optical experiments), we can now further simplify this expression by noting that only the term $\hat{\mathcal{E}}_{-}(\mathbf{r},\tau)\hat{\mathcal{V}}_{+}(\tau)$ needs to be considered for $\hat{H}_{\mathrm{int},-}(\tau)$, since the final expression can be factorized into a trace over the field degrees of freedom and a trace over the matter degrees of freedom.

The trace over the matter degrees of freedom then vanishes if the last interaction is given by $\hat{\mathcal{V}}_-(\tau)$ since the trace over a commutator always vanishes due to its invariance under cyclic permutation, $\mathrm{tr}\left\{\hat{A}_-\hat{X}\right\} = 0$. These considerations lead to

$$\left\langle \hat{\mathcal{S}}(t) \right\rangle = \frac{i}{\hbar}\int_{-\infty}^{t} \mathrm{d}\tau \ \mathrm{tr}\left\{ \mathcal{T}\left[\hat{\mathcal{S}}, \hat{\mathcal{E}}(\mathbf{r},\tau)\right] \hat{\mathcal{V}}_+(\tau) \exp\left(-\frac{i}{\hbar}\int_{-\infty}^{\tau} \mathrm{d}\tau' \hat{H}_{\mathrm{int},-}(\tau') \right) \hat{\rho}_{\mathrm{in}} \right\}, \quad (1.75)$$

where we have again used the invariance of the trace under cyclic permutation in order to let the superoperator $\hat{\mathcal{E}}_-(\mathbf{r},\tau)$ act to the left[3].

Now, the expansion of the evolution operator can be carried on and the nth term of the exponential in Eq. (1.75) results in a correction $\left\langle \hat{\mathcal{S}}^{(n)}(t) \right\rangle$ to the signal according to

$$\begin{aligned} \left\langle \hat{\mathcal{S}}^{(n)}(t) \right\rangle = \left(\frac{i}{\hbar}\right)^{n+1} \sum_{\{\mu_i\}} \int_{-\infty}^{t} \mathrm{d}\tau \int_{-\infty}^{\tau} \mathrm{d}\tau_n ... \int_{-\infty}^{\tau_2} \mathrm{d}\tau_1 \\ \times \mathrm{tr}\left\{ \left[\hat{\mathcal{S}}, \hat{\mathcal{E}}(\mathbf{r},\tau)\right] \hat{\mathcal{E}}_{\mu_n}(\mathbf{r},\tau_n) ... \hat{\mathcal{E}}_{\mu_1}(\mathbf{r},\tau_1) \hat{\rho}_{\mathrm{field}} \right\} \\ \times \mathrm{tr}\left\{ \hat{\mathcal{V}}_+ \hat{\mathcal{G}}(\tau-\tau_n) \hat{\mathcal{V}}_{\overline{\mu_n}} \hat{\mathcal{G}}(\tau_n - \tau_{n-1}) ... \hat{\mathcal{G}}(\tau_2 - \tau_1) \hat{\mathcal{V}}_{\overline{\mu_1}} \hat{\rho}_{\mathrm{mat}} \right\}. \end{aligned} \quad (1.76)$$

Here, the sequence $' - \mu_n ... \mu_1'$ with $\mu_i = \pm$ denotes the type of superoperator interactions with the electric fields in chronological order (the last interaction is always a minus in order to obtain a signal at all) and the sum runs over all possible combinations of sequences. Note that by virtue of Eq. (1.71), the corresponding superoperator interactions for the dipole operators is given by the opposite sequence $' + \overline{\mu_n} ... \overline{\mu_1}'$, with $\overline{(\pm)} = (\mp)$. For the dipole superoperators, we have used Eq. (1.72) and the relation $\hat{\mathcal{G}}(\tau)\hat{\mathcal{G}}^\dagger(\tau_n) = \hat{\mathcal{G}}(\tau - \tau_n)$. The first and the last free evolution described by the superoperator Green's functions $\hat{\mathcal{G}}(\tau_1)$ and $\hat{\mathcal{G}}^\dagger(\tau)$, respectively, can be ignored due to the fact that the matter density matrix $\hat{\rho}_{\mathrm{mat}}$ is in thermal equilibrium.

To get rid of the time ordering inside the integrals, a change of integration variables can be performed, so that $t_i = \tau_{i+1} - \tau_i$. Physically, the variables τ_i describe the actual times of interactions, while the variables t_i describe the time intervals between the $(i+1)$th and the ith interaction. This leads to

$$\begin{aligned} \left\langle \hat{\mathcal{S}}^{(n)}(t) \right\rangle = \left(\frac{i}{\hbar}\right)^{n+1} \sum_{\{\mu_i\}} \int_{-\infty}^{t} \mathrm{d}\tau \int_{0}^{\infty} \mathrm{d}t_n ... \int_{0}^{\infty} \mathrm{d}t_1 \ \mathrm{tr}\left\{ \hat{\mathcal{V}}_+ \hat{\mathcal{G}}(t_n) \hat{\mathcal{V}}_{\overline{\mu_n}} \hat{\mathcal{G}}(t_{n-1}) ... \hat{\mathcal{G}}(t_1) \hat{\mathcal{V}}_{\overline{\mu_1}} \hat{\rho}_{\mathrm{mat}} \right\} \\ \times \mathrm{tr}\left\{ \left[\hat{\mathcal{S}}, \hat{\mathcal{E}}(\mathbf{r},\tau)\right] \hat{\mathcal{E}}_{\mu_n}(\mathbf{r}, \tau - t_n) ... \hat{\mathcal{E}}_{\mu_1}(\mathbf{r}, \tau - t_n - ... - t_1) \hat{\rho}_{\mathrm{field}} \right\} \end{aligned} \quad (1.77)$$

[3] $\mathrm{tr}\left\{\hat{X}\hat{A}_-\hat{\rho}\right\} = \mathrm{tr}\left\{\hat{X}\hat{A}\hat{\rho} - \hat{X}\hat{\rho}\hat{A}\right\} = \mathrm{tr}\left\{\hat{X}\hat{A}\hat{\rho} - \hat{A}\hat{X}\hat{\rho}\right\} = \mathrm{tr}\left\{\left[\hat{X},\hat{A}\right]\hat{\rho}\right\}$

Finally, we can express the first n interacting fields in terms of their Fourier transforms $\hat{\mathcal{E}}(\mathbf{r},t) = \int_{-\infty}^{\infty} \mathrm{d}\omega\ \hat{\mathcal{E}}(\mathbf{r},\omega)e^{-i\omega t}$, where $\hat{\mathcal{E}}(\mathbf{r},-\omega) = \hat{\mathcal{E}}^{\dagger}(\mathbf{r},\omega)$ since $\hat{\mathcal{E}}(\mathbf{r},t)$ is Hermitian. Using the definition $\hat{\mathcal{G}}(\omega) = -i\int_0^{\infty} \mathrm{d}t\ \hat{\mathcal{G}}(t)e^{i\omega t}$ for the Green's function in Fourier space, the nth order correction to the signal is then given by

$$\begin{aligned}\left\langle \hat{\mathcal{S}}^{(n)}(t) \right\rangle = \varepsilon_0 \frac{i}{\hbar} \sum_{\{\mu_i\}} \int_{-\infty}^{t} \mathrm{d}\tau \int_{-\infty}^{\infty} \mathrm{d}\omega_n ... \int_{-\infty}^{\infty} \mathrm{d}\omega_1\ \chi^{(n)}_{+\overline{\mu_n}...\overline{\mu_1}}(-\omega_s;\omega_n,...,\omega_1) \\ \times \mathrm{tr}\left\{ \left[\hat{\mathcal{S}}, \hat{\mathcal{E}}(\mathbf{r},\tau) \right] \hat{\mathcal{E}}_{\mu_n}(\mathbf{r},\omega_n)...\hat{\mathcal{E}}_{\mu_1}(\mathbf{r},\omega_1)\hat{\rho}_{\mathrm{field}} \right\} e^{-i\omega_s \tau},\end{aligned} \tag{1.78}$$

where $\omega_s = \sum_{i=1}^{n} \omega_i$. We have introduced the nth order susceptibility $\chi^{(n)}$, which is given by[4]

$$\chi^{(n)}_{+\overline{\mu_n}...\overline{\mu_1}}(-\omega_s;\omega_n,...,\omega_1) = \frac{1}{\varepsilon_0}\left(\frac{-1}{\hbar}\right)^n \mathrm{tr}\left\{ \hat{\mathcal{V}}_{+} \hat{\mathcal{G}}(\omega_s) \hat{\mathcal{V}}_{\overline{\mu_n}} \hat{\mathcal{G}}(\omega_{n-1}+...+\omega_1)...\hat{\mathcal{G}}(\omega_1)\hat{\mathcal{V}}_{\overline{\mu_1}}\hat{\rho}_{\mathrm{mat}} \right\}. \tag{1.79}$$

Here, the argument of the kth superoperator Green's function is given by $\sum_{i=1}^{k} \omega_i$.

Equation (1.78) represents the nth order response of a single molecule to the electric field. Similar expressions can be derived for more complicated systems [13]. In general, both the electric field and the dipole operator are given by vectors and the susceptibilities are given by high-rank tensors. The tensor structure of the susceptibilities gains special importance inside of anisotropic media like crystals, where the spatial symmetries of the crystal structure can be used to rule out various elements of these tensors [30].

We have shown how the response of a single molecule can be described in powers of the electric field. Usually, the nonlinear susceptibilities in Eq. (1.79) are either calculated assuming interactions with classical electric fields, or measured using classical electrical fields. In this case, the superoperator sequence for the fields is given by $'-\underbrace{+...+}_{n}$ for the nth order correction, since the commutator vanishes for classical fields (note that the last interaction needs to be a $'-'$-type to generate a measurable signal in the first place). This leads to a classical susceptibility of the form $\chi^{(n)}_{+\underbrace{-...-}_{n}}$, i.e. n $'-'$-type dipole superoperator interactions, followed by a $'+'$-type interaction for the nth-order susceptibility. These types of susceptibilities are also called causal since a clear time ordering between the interaction and generation of fields can be established.

[4]Note that usually, the susceptibilities are defined in a way that makes them invariant under permutations of their frequency arguments (together with all corresponding superoperoperator signs). For sake of simplicity, we refrain from doing so in this thesis.

The matter system interacts with n fields (first n $'+'$-type interactions) and generates a new field (last $'-'$-type interaction).

Other classes of nonlinear susceptibilities are given by superoperator sequences with several +-type interactions for the dipole superoperators. A susceptibility of the form $\chi^{(n)}_{+\underbrace{+...+}_{n-m}\underbrace{-...-}_{m}}$ for example describes the generation of $n-m+1$ fields through an interaction with m fields. The $n-m+1$ fields are being generated through spontaneous fluctuations, and thus no clear time ordering for the generation of the fields can be established. These kinds of susceptibilities are therefore termed quantum or noncausal susceptibilities[27, 29].

In quantum optics, the classical susceptibilities are then typically used to describe the nth-order polarization as

$$\begin{aligned}\hat{\mathcal{P}}^{(n)}(\mathbf{r},t) = \varepsilon_0 \int_{-\infty}^{\infty} \mathrm{d}\omega_n ... \int_{-\infty}^{\infty} \mathrm{d}\omega_1 \; \chi^{(n)}_{+-...-}(-\omega_s;\omega_n,...,\omega_1) \\ \times \hat{\mathcal{E}}(\mathbf{r},\omega_n)...\hat{\mathcal{E}}(\mathbf{r},\omega_1)e^{-i\omega_s\tau}.\end{aligned} \tag{1.80}$$

Note that although the fields are considered quantum, the response of the medium to these fields is considered to be the same as for classical fields. If all frequencies of the involved fields are far away from material resonances, the noncausal susceptibilities vanish and Eq. (1.80) serves as a good approximation. Close to material resonances, however, these effective theories are ignoring crucial contributions stemming from the noncausal susceptibilities.

1.4.3 Diagrammatic visualization of nonlinear processes

Equation (1.78) represents a very general expression for the nth-order nonlinear response of a single molecule. The field operator $\hat{\mathcal{E}}(\mathbf{r},t)$ is given by the sum of the annihilation and creation operators of all fields involved in the nonlinear process and furthermore appears with either a $'+'$- or a $'-'$-type superoperator index. In principle, this results in a large number of terms that need to be taken into account. In reality however, the majority of terms can be neglected from the start due to details about the signal and conditions like energy conservation and phase matching. In order to keep track of the relevant terms that actually need to be calculated, a diagrammatic approach can be used to visualize the relevant terms.

Figure 1.1(a) explains the basic idea of the diagrammatic visualization. The vertical line represents the combined density matrix of the matter and the field and time runs along the line with the past at the bottom and the future at the top. The line is then dressed with arrows representing interactions with the field, where multiple shapes of

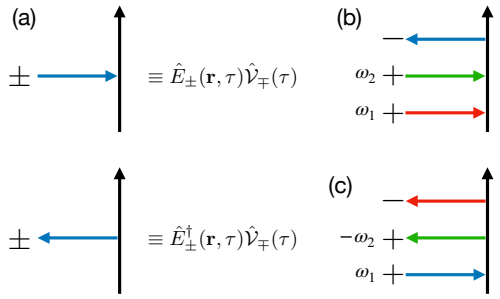

Figure 1.1: Diagrammatic visualization of the terms in Eq. (1.78). (a) Vectors pointing to the right (left) describe the annihilation (creation) of a photon. The sign on the left of the arrow describes the type of superoperator interaction for the field, which is accompanied by the opposite sign for the dipole superoperator. (b) Example for a classical sum frequency process. The frequency of the first two fields is given, additionally. The frequency of the outgoing field is given by $\omega_1 + \omega_2$, if $t \to \infty$ in Eq. (1.81). (c) Example for a classical difference frequency process. The frequency of the first two fields is given, additionally. Note that the creation of a photon is accompanied by a $-$ sign.

arrows can be used to represent fields of different frequencies or polarizations. An arrow pointing to the right (left) then describes the annihilation (creation) of a photon. Finally, the sign next to the arrow defines the type of superoperator associated with the respective field interaction.

In Fig. 1.1(b) we show how a classical sum frequency process can be visualized diagrammatically. Two $'+'$-type interactions with lower field frequencies (red and green), corresponding to the absorption of two photons, lead to the generation of a higher frequency field (blue) through a $'-'$-type interaction and the creation of a photon. This diagram therefore represents a classical three-wave mixing process and is described by the susceptibility $\chi^{(2)}_{+--}$. The corresponding expectation value is given by

$$\begin{aligned}\left\langle \hat{\mathcal{S}}^{(3)}_{\mathrm{SFG}}(t) \right\rangle = \varepsilon_0 \frac{i}{\hbar} \sum_{\{\mu_i\}} \int_{-\infty}^{t} \mathrm{d}\tau \int_0^{\infty} \mathrm{d}\omega_2 \int_0^{\infty} \mathrm{d}\omega_1 \; \chi^{(2)}_{+--}(-\omega_2-\omega_1;\omega_2,\omega_1) \\ \times \mathrm{tr}\left\{ \left[\hat{\mathcal{S}}, \hat{E}^{\dagger}(\mathbf{r},\tau) \right] \hat{E}_+(\mathbf{r},\omega_2)\hat{E}_+(\mathbf{r},\omega_1)\hat{\rho}_{\mathrm{field}} \right\} e^{-i(\omega_2+\omega_1)\tau}.\end{aligned} \tag{1.81}$$

The diagram for a classical difference frequency process is shown in Fig. 1.1(c). Here, the first $'+'$-type interaction with the field describes the annihilation of a high frequency photon, while the second $'+'$-type interaction describes the creation of a low frequency photon. This leads to the generation of both another low frequency photon

and low frequency field,

$$\left\langle \hat{\mathcal{S}}^{(3)}_{\mathrm{DFG}}(t) \right\rangle = \varepsilon_0 \frac{i}{\hbar} \sum_{\{\mu_i\}} \int_{-\infty}^{t} \mathrm{d}\tau \int_0^{\infty} \mathrm{d}\omega_2 \int_0^{\infty} \mathrm{d}\omega_1 \; \chi^{(2)}_{+--}(\omega_2 - \omega_1; -\omega_2, \omega_1) \\ \times \mathrm{tr}\left\{ \left[\hat{\mathcal{S}}, \hat{E}^{\dagger}(\mathbf{r}, \tau) \right] \hat{E}^{\dagger}_{+}(\mathbf{r}, \omega_2) \hat{E}_{+}(\mathbf{r}, \omega_1) \hat{\rho}_{\mathrm{field}} \right\} e^{i(\omega_2 + \omega_1)\tau}. \tag{1.82}$$

1.4.4 Second order susceptibilities

Having derived the general expression of the nth order response of a single molecule to the electric field, we will now show how the second order susceptibility can be calculated explicitly. According to Eq. (1.79), the second order susceptibility is given by

$$\chi^{(2)}_{+rs}(-\omega_2 - \omega_1; \omega_2, \omega_1) = \frac{1}{\varepsilon_0 \hbar^2} \mathrm{tr}\left\{ \hat{\mathcal{V}}_{+} \hat{\mathcal{G}}(\omega_2 + \omega_1) \hat{\mathcal{V}}_{r} \hat{\mathcal{G}}(\omega_1) \hat{\mathcal{V}}_{s} \hat{\rho}_{\mathrm{mat}} \right\}. \tag{1.83}$$

The Hamiltonian describing a single molecule in its eigenstate basis $\{|i\rangle\}$ is given by

$$\hat{H}_{\mathrm{mat}} = \sum_i \hbar \omega_i |i\rangle\langle i|. \tag{1.84}$$

In the following, we will consider the single molecule to be coupled to a thermal bath, so that its evolution can be described by the equation

$$\frac{\partial}{\partial t} \hat{\rho}_{\mathrm{mat}}(t) = -\frac{i}{\hbar} \left(\hat{H}_{\mathrm{mat},-} - i\hat{\Gamma}_{+} \right) \hat{\rho}_{\mathrm{mat}}(t). \tag{1.85}$$

Here, the superoperator associated to $\hat{\Gamma} = \sum_j \hbar \gamma_j |j\rangle\langle j|$ describes the dissipation to the bath that has been traced over in order to obtain Eq. (1.85). γ_j represents the inverse lifetime of level j. The evolution according to Eq. (1.85) can be described through the superoperator Green's function

$$\hat{\mathcal{G}}(t) = \exp\left[-\frac{i}{\hbar} \left(\hat{H}_{\mathrm{mat},-} - i\hat{\Gamma}_{+} \right) t \right]. \tag{1.86}$$

The Fourier transform of the Green's function is then given by

$$\hat{\mathcal{G}}(\omega) = -i \int_0^{\infty} \mathrm{d}t \; \hat{\mathcal{G}}(t) e^{i\omega t} = \frac{1}{\omega - \frac{1}{\hbar}\hat{H}_{\mathrm{mat},-} + i\frac{1}{\hbar}\hat{\Gamma}_{+}} \tag{1.87}$$

Since both superoperators in Eq. (1.87) are diagonal in the eigenstate basis of the molecule, it is easily verified that

$$\hat{\mathcal{G}}(\omega)|a\rangle\langle b| = I_{ab}(\omega)|a\rangle\langle b|, \tag{1.88}$$

with

$$I_{ab}(\omega) = \frac{1}{\omega - \omega_{ab} + i\gamma_{ab}}, \tag{1.89}$$

Here, we have defined the transition frequencies $\omega_{ab} = \omega_a - \omega_b$ and $\gamma_{ab} = \frac{1}{2}(\gamma_a + \gamma_b)$.

Finally, by expressing the dipole operator in the eigenstate basis of the molecule $\hat{\mathcal{V}} = \sum_{a,b} \mu_{ab}|a\rangle\langle b|$, and assuming that it is initially in its ground state $\hat{\rho}_{\mathrm{mat}} = |g\rangle\langle g|$, we can calculate the second order susceptibility,

$$\begin{aligned}\chi^{(2)}_{+rs}(-(\omega_2+\omega_1);\omega_2,\omega_1) = \frac{2^{-1-[\mathrm{sgn}(r)+\mathrm{sgn}(s)]/2}}{\varepsilon_0\hbar^2}\sum_{a,b}\mu_{gb}\mu_{ba}\mu_{ag} \\ \times\left[I_{bg}(\omega_2+\omega_1)I_{ag}(\omega_1) + \mathrm{sgn}(s)I_{ab}(\omega_2+\omega_1)I_{gb}(\omega_1)\right. \\ + \mathrm{sgn}(r)\mathrm{sgn}(s)I_{ga}(\omega_2+\omega_1)I_{gb}(\omega_1) \\ \left. + \mathrm{sgn}(r)I_{ab}(\omega_2+\omega_1)I_{ag}(\omega_1)\right].\end{aligned} \tag{1.90}$$

1.5 Electro-optic sampling

In Sec. 1.1, the quantization of the electromagnetic field was derived. Its Hamiltonian in Eq. (1.19) was shown to be equivalent to a harmonic oscillator, where the electric and magnetic fields take on the roles of the position and momentum. Rewritten in terms of annihilation and creation operators, describing the annihilation and creation of photons, the Hamiltonian took on the form shown in Eq. (1.32). The second term of the Hamiltonian in Eq. (1.32) shows that even in the absence of photons, each wave vector mode $\mathbf{k}$ still possesses a nonvanishing energy resulting from vacuum fluctuations.

These vacuum fluctuations have been shown to be the cause for many physical phenomena such as the Lamb shift[31–33] or the Casimir effect [34, 35]. In quantum optics, the quantum statistics of electromagnetic radiation are typically studied through photon correlation measurements[1, 36] or homodyning measurements[37–39]. In both cases, however, the state under study needs to be amplified by a coherent electric field and the information about this state is averaged over multiple cycles of the field.

In classical optics, electro-optic sampling represents a well-established method for the characterization of classical electric field transients in the terahertz (THz) range with temporal resolutions much shorter than the typical time scales of the sampled field[40–45]. Here, a short near-infrared probe pulse is used to sample the trace of a classical THz transient with subcycle temporal resolution [40, 46, 47]. The fields interact in a second-order $\chi^{(2)}$ nonlinear crystal and the polarization of the near-infrared

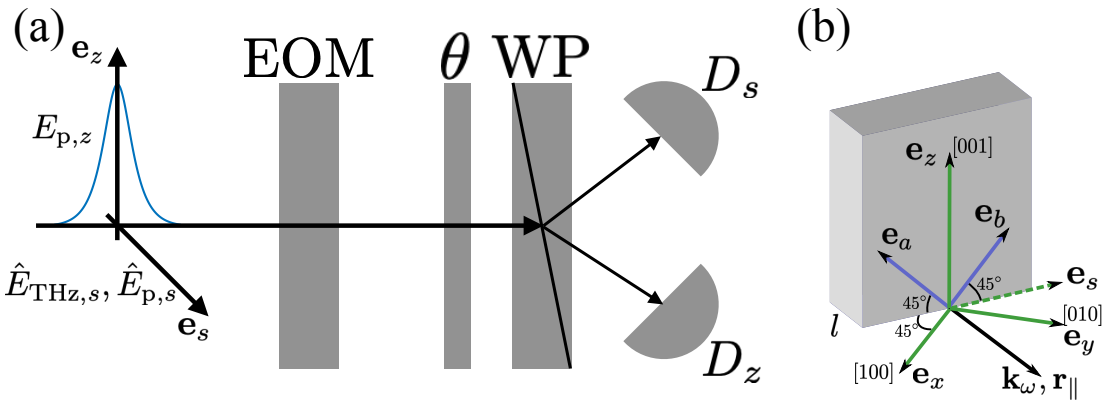

Figure 1.2: Experimental setup for electro-optic sampling and orientation of the zincblende-type electro-optic medium (EOM). (a) The setup consists of a nonlinear EOM, a waveplate inducing a phase shift of θ along its fast axis, a Wollaston prism (WP) separating the two polarization directions and two photon detectors D_s and D_z. An intense $\mathbf{e}_z$-polarized coherent near-infrared (NIR) probe pulse (blue) $\mathcal{E}_{\mathrm{p},z}$ is applied to probe a co-propagating quantum THz field $\hat{E}_{\mathrm{THz},s}$ polarized in the perpendicular $\mathbf{e}_s$ direction. $\hat{E}_{\mathrm{p},s}$ denotes the induced $\mathbf{e}_s$-polarized NIR quantum field.

probe changes proportionally to the local THz amplitude. This technique was recently extended into the quantum domain by applying it to THz fields with vanishing mean values such as e.g. vacuum fluctuations. The probe is sampling the statistics of the input on subcycle time scales by imprinting it onto its polarization state [6, 9]. The striking advantage of electro-optic sampling in comparison to standard homodyne detection [48] relies on providing information on the fluctuations of THz fields directly in the time domain, in complete analogy to its classical counterpart [8]. A slightly extended configuration also allows to characterize the spatio-temporal correlations of THz fields [9, 49–53] and might provide a useful spectroscopic tool to access, e.g., the linear dielectric function of materials without requiring the presence of photons in the sampled frequency region [54].

The setup for quantum electro-optic sampling is shown in Fig. 1.2(a). In standard electro-optic sampling, an ultrashort $\mathbf{e}_z$-polarized NIR probe pulse is used to sample a classical, $\mathbf{e}_s$-polarized THz transient. In order to obtain subcycle resolution, the probe has to be shorter than half of an optical cycle of the sampled field. The probe pulse and the THz field are sent into an electro-optic medium with a second-order nonlinearity, where the two fields interact with each other by means of both sum frequency and difference frequency generation (SFG nad DFG, respectively). This leads to the generation of an $\mathbf{e}_s$-polarized NIR field, whose amplitude is proportional to the local field strength of the sampled field at the maximum of the probe. The generated NIR field possesses an additional phase shift of $\pi/2$ with respect to the probe (ignoring the phase

of the sampled field), which leads to an elliptical polarization of the initially linearly polarized probe. This generated ellipticity is now measured by the ellipsometry part of the experimental setup, consisting of a quarter-wave plate ($\theta = \pi/2$), a Wollaston Prism (WP), and two NIR photon detectors D_s and D_z.

Here, a ZnTe crystal is employed as the EOM , whose crystallographic point group is given by $\overline{4}3m$ [30]. Figure 1.2(b) shows the orientation of the crystal. In order to achieve a maximal electro-optic signal, the polarization of the probe is aligned with the [001] crystallographic axis of the crystal and its propagation direction is chosen to be perpendicular to the (110) plane. In this case, the second-order polarization is given by

$$\hat{\mathcal{P}}_x^{(2)}(\mathbf{r},t) = 2\varepsilon_0 \chi_{+--}^{(2)} \hat{\mathcal{E}}_{\mathrm{THz},y}(\mathbf{r},t)\mathcal{E}_{\mathrm{p},z}(\mathbf{r},t), \tag{1.91}$$

$$\hat{\mathcal{P}}_y^{(2)}(\mathbf{r},t) = 2\varepsilon_0 \chi_{+--}^{(2)} \hat{\mathcal{E}}_{\mathrm{THz},x}(\mathbf{r},t)\mathcal{E}_{\mathrm{p},z}(\mathbf{r},t), \tag{1.92}$$

where the second-order nonlinearity is assumed to be frequency independent since all involved electric fields are far away from the resonant transitions of the crystal. This results in a local response of the crystal to the electric fields both in time and space. Note that the THz field is treated quantum while the probe field is treated classical due to its strong coherent amplitude. Ignoring the polarization directions, this form of the polarization can also be derived by extracting the corresponding polarizations from Eqs. (1.81) and (1.82) and adding them. In the (110) plane, the classical probe induces a polarization along the $\mathbf{e}_s$ axis,

$$\hat{\mathcal{P}}_s^{(2)}(\mathbf{r},t) = \frac{1}{\sqrt{2}}\left[\hat{\mathcal{P}}_y^{(2)}(\mathbf{r},t) - \hat{\mathcal{P}}_x^{(2)}(\mathbf{r},t)\right] = -\varepsilon_0 d \hat{\mathcal{E}}_{\mathrm{THz},s}(\mathbf{r},t)\mathcal{E}_{\mathrm{p},z}(\mathbf{r},t), \tag{1.93}$$

where $d = 2\chi_{+--}^{(2)}$.

This polarization acts as a source term in the inhomogeneous wave equation for the NIR field $\hat{\mathcal{E}}_{\mathrm{p},s}(\mathbf{r},t)$ [cf. Eq. (1.57)]. Both fields $\hat{\mathcal{E}}_{\mathrm{p},z}(\mathbf{r},t)$ and $\hat{\mathcal{E}}_{\mathrm{p},s}(\mathbf{r},t)$ can now be treated in the paraxial approximation by assuming that they are essentially only propagating along the $\mathbf{r}_\parallel$ axis in Fig. 1.2(b) [cf. Sec. 1.2]. In this case, the fields $\mathcal{F}(\mathbf{r},t) = \hat{\mathcal{E}}, \hat{\mathcal{P}}$ (and equivalently the classical probe) can be decomposed as $\hat{\mathcal{F}}(\mathbf{r},t) = \int_{-\infty}^{\infty} \mathrm{d}\omega\ \hat{F}(\mathbf{r};\omega)e^{i[k_\omega(r_\parallel + l/2) - \omega t]}$. Assuming that the envelope $\hat{F}(\mathbf{r};\omega)$ only varies slowly with respect to $e^{ik_\omega r_\parallel}$ during the propagation through the crystal, the term $\frac{\partial^2}{\partial r_\parallel^2}\hat{E}_{\mathrm{p},s}(\mathbf{r};\omega)$ can be neglected. This results in the paraxial wave equation for $\hat{E}_{\mathrm{p},s}(\mathbf{r};\omega)$,

$$\left[\nabla_\perp^2 + 2ik_\omega \frac{\partial}{\partial r_\parallel}\right] \hat{E}_{\mathrm{p},s}(\mathbf{r};\omega) = -\frac{\omega^2}{\varepsilon_0 c_0^2}\hat{P}_s^{(2)}(\mathbf{r};\omega), \tag{1.94}$$

where $\mathbf{r}_\perp = (r_z, r_s)^T$ lies in the (110), $\nabla_\perp^2 = \partial^2/\partial r_z^2 + \partial^2/\partial r_s^2$, and $\hat{P}^{(2)}(\mathbf{r};\omega) = -\varepsilon_0 d \int_{-\infty}^{\infty} \mathrm{d}\Omega\ \hat{E}_{\mathrm{THz},s}(\mathbf{r},\Omega) E_{\mathrm{p},z}(\mathbf{r},\omega-\Omega) e^{i(k_\Omega + k_{\omega-\Omega} - k_\omega) r_\parallel}$. Note that in this thesis, we will use Ω to denote THz frequencies and ω to denote NIR frequencies.

The probe is given by a fundamental Gaussian mode in the transverse spatial plane and a broadband frequency mode of $\alpha_{\mathrm{p}}(\omega)$,

$$E_{\mathrm{p},z}(\mathbf{r};\omega) = \alpha_{\mathrm{p}}(\omega)\mathrm{LG}_{00}(\mathbf{r}_\perp, \mathbf{r}_\parallel; k_\omega). \tag{1.95}$$

For a crystal of length l much shorter than the relevant THz frequencies Ω, i.e. $l \ll k_\Omega w_0^2/2$ with beam waist size w_0, the beam waist divergence of all involved fields inside the crystal can be neglected and the envelopes can be considered independent of $r_\parallel$, $\hat{F}(\mathbf{r}_\perp;\omega) = \hat{F}(\mathbf{r}_\perp, r_\parallel = 0;\omega)$. The total NIR field at the exit of the crystal $r_\parallel = l/2$ is then given by

$$\hat{\mathbf{E}}_{\mathrm{p}}(\mathbf{r}_\perp;\omega) = E_{\mathrm{p},z}(\mathbf{r}_\perp;\omega)\mathbf{e}_z + \left[\hat{E}_{\mathrm{p},s}(\mathbf{r}_\perp;\omega) + \hat{E}^{(1)}_{\mathrm{p},s}(\mathbf{r}_\perp;\omega)\right]\mathbf{e}_s, \tag{1.96}$$

where $\hat{E}_{\mathrm{p},s}(\mathbf{r}_\perp;\omega)$ denotes the initial vacuum field in the $\mathbf{e}_s$ polarization and $\hat{E}^{(1)}_{\mathrm{p},s}(\mathbf{r}_\perp;\omega)$ is its first order correction due to the electro-optic process. The first order correction is given by

$$\hat{E}^{(1)}_{\mathrm{p},s}(\mathbf{r}_\perp;\omega) = \int_{-\infty}^{\infty} \mathrm{d}\Omega \hat{E}_{\mathrm{THz},s}(\mathbf{r}_\perp;\Omega) E_{\mathrm{p},z}(\mathbf{r}_\perp;\omega-\Omega)\zeta_{\omega,\Omega}, \tag{1.97}$$

where $\zeta_{\omega,\Omega} = -idl\omega/(2c_0 n)\mathrm{sinc}\left[(n_\Omega - n_g)l\Omega/(2c_0)\right] e^{i(n_\Omega - n_g)l\Omega/(2c_0)}$ describes the phase matching between the three wave vectors. Here, the wave vector $k_{\omega-\Omega} \approx k_\omega - n_g\Omega/c_0$ has been Taylor expanded around the NIR frequency ω, and n and n_g describe the refractive index and the group refractive index $c_0\partial k_\omega/\partial\omega$ at the center frequency ω_c of the probe, respectively. The refractive index for the THz frequencies n_Ω is given by

$$n_\Omega = \Re\left\{\sqrt{\left[1 + \frac{(\hbar\omega_{\mathrm{LO}})^2 + (\hbar\omega_{\mathrm{TO}})^2}{(\hbar\omega_{\mathrm{TO}})^2 - (\hbar\Omega)^2 - i\hbar\gamma\Omega}\right]\epsilon_\infty}\right\}, \tag{1.98}$$

with $\Re\{\cdot\}$ denoting the real part, $\hbar\omega_{\mathrm{LO}} = 206\ \mathrm{cm}^{-1}$, $\hbar\omega_{\mathrm{TO}} = 177\ \mathrm{cm}^{-1}$, $\gamma = 3.07\ \mathrm{cm}^{-1}$, and $\epsilon_\infty = 6.7$.

The ellipsometry scheme in Fig. 1.2(a) consists of a quarter-wave plate, a Wollaston-Prism, and two photon detectors. The quarter-wave plate induces a phase shift of $\theta = \pi/2$ along the two directions $\mathbf{e}_a$ and $\mathbf{e}_b$. Its fast axis is therefore rotated by an angle of 45° degrees with respect to the probe field. This misalignment mixes the two polarization directions $\mathbf{e}_s$ and $\mathbf{e}_z$. Afterwards, the Wollaston prism separates the two

polarization components $\mathbf{e}_s$ and $\mathbf{e}_z$ and the signal $\hat{\mathcal{S}}$ is given by the difference in photon numbers between the two polarization directions,

$$\hat{\mathcal{S}} = \hat{N}_s - \hat{N}_z, \tag{1.99}$$

where the photon number operators for the polarizations $\alpha = z, s$ are given by

$$\hat{N}_\alpha = C \int \mathrm{d}^2 r_\perp \int_0^\infty \mathrm{d}\omega \frac{1}{\hbar\omega} \hat{E}'^{\dagger}_{\mathrm{p},\alpha}(\mathbf{r}_\perp;\omega) \hat{E}'_{\mathrm{p},\alpha}(\mathbf{r}_\perp;\omega), \tag{1.100}$$

with $C = 4\pi\varepsilon_0 c_0 n$. Note that $\hat{E}'_{\mathrm{p},\alpha}(\mathbf{r}_\perp;\omega)$ is the field after the quarter-wave plate and is given by a superposition of both $E_{\mathrm{p},z}(\mathbf{r}_\perp;\omega)$ and $\hat{E}_{\mathrm{p},s}(\mathbf{r}_\perp;\omega)$.

The signal $\hat{\mathcal{S}} = \hat{\mathcal{S}}_{\mathrm{eo}} + \hat{\mathcal{S}}_{\mathrm{sn}}$ in Eq. (1.99) can then be separated into an electro-optic part $\hat{\mathcal{S}}_{\mathrm{eo}}$ containing the generated field $\hat{E}^{(1)}_{\mathrm{p},s}(\mathbf{r}_\perp;\omega)$ and a shot noise part $\hat{\mathcal{S}}_{\mathrm{sn}}$ containing the initial vacuum field $\hat{E}_{\mathrm{p},s}(\mathbf{r}_\perp;\omega)$,

$$\begin{aligned} \hat{\mathcal{S}}_{\mathrm{eo}} &= C \int \mathrm{d}^2 r_\perp \int_0^\infty \mathrm{d}\omega \; g_{00}(\mathbf{r}_\perp) \frac{1}{\hbar\omega} E^*_{\mathrm{p},z}(\mathbf{r}_\perp;\omega) \hat{E}^{(1)}_{\mathrm{p},s}(\mathbf{r}_\perp;\omega), \\ &= \frac{dlN\omega_{\mathrm{p}}}{c_0 n} \int \mathrm{d}^2 r_\perp \int_{-\infty}^\infty \mathrm{d}\Omega \; g^2_{00}(\mathbf{r}_\perp) \hat{E}_{\mathrm{THz},s}(\mathbf{r}_\perp;\Omega) R(\Omega), \end{aligned} \tag{1.101a}$$

$$\hat{\mathcal{S}}_{\mathrm{sn}} = C \int \mathrm{d}^2 r_\perp \int_0^\infty \mathrm{d}\omega \; g_{00}(\mathbf{r}_\perp) \frac{1}{\hbar\omega} E^*_{\mathrm{p},z}(\mathbf{r}_\perp;\omega) \hat{E}_{\mathrm{p},s}(\mathbf{r}_\perp;\omega). \tag{1.101b}$$

Here, N is the photon number of the probe

$$N = C \int_0^\infty \mathrm{d}\omega \frac{1}{\hbar\omega} |\alpha_{\mathrm{p}}(\omega)|^2, \tag{1.102}$$

ωp is the average detected frequency

$$\omega_{\mathrm{p}} = \frac{\int_0^\infty \mathrm{d}\omega |\alpha_{\mathrm{p}}(\omega)|^2}{\int_0^\infty \mathrm{d}\omega |\alpha_{\mathrm{p}}(\omega)|^2/\omega}, \tag{1.103}$$

and $g_{00}(\mathbf{r}_\perp) = \mathrm{LG}_{00}(\mathbf{r}_\perp, r_\parallel = 0; k_\omega) = \sqrt{2/\pi} w_0^{-1} \exp(-r_\perp^2/w_0^2)$ is the Laguerre-Gaussian mode evaluated at the center of the crystal. The gating function

$$R(\Omega) = \mathrm{sinc}\left[(n_\Omega - n_g) l\Omega/(2c_0)\right] e^{i(n_\Omega - n_g) l\Omega/(2c_0)} f(\Omega) \tag{1.104}$$

with $f(\Omega) = \left[f^*_+(\Omega) + f_-(\Omega)\right]/2$ being defined through the autocorrelation functions

$$f_\pm(\Omega) = \frac{\int_0^\infty \mathrm{d}\omega \; \alpha^*_{\mathrm{p}}(\omega) \alpha_{\mathrm{p}}(\omega \pm \Omega)}{\int_0^\infty \mathrm{d}\omega \; |\alpha_{\mathrm{p}}(\omega)|^2}, \tag{1.105}$$

where $f_+(\Omega)$ [$f_-(\Omega)$] describes the DFG [SFG] contribution to the electro-optic signal.

For a classical THz input field, the operator $\hat{E}_{\mathrm{THz},s}(\mathbf{r}_\perp;\Omega)$ in Eq. (1.97) can be replaced by the corresponding coherent amplitude. In this case, the electro-optic process generates a coherent field polarized orthogonally to the probe. This results in a change in the polarization of the probe, which is subsequently measured using ellipsometry. If the incoming THz field is in the vacuum state, the expectation value of the polarization of the probe remains unchanged, $\langle\hat{\mathcal{S}}\rangle = 0$, but its fluctuations increase due to the electro-optic process. The fluctuations of the polarization are given by the variance of the signal $\left\langle\hat{\mathcal{S}}^2\right\rangle = \left\langle\hat{\mathcal{S}}^2_{\mathrm{eo}}\right\rangle + \left\langle\hat{\mathcal{S}}^2_{\mathrm{sn}}\right\rangle$ and can be separated into its shot noise part $\left\langle\hat{\mathcal{S}}^2_{\mathrm{sn}}\right\rangle$ and its electro-optic part $\left\langle\hat{\mathcal{S}}^2_{\mathrm{eo}}\right\rangle$, since the two are uncorrelated. The electro-optic fluctuations yield

$$\left\langle\hat{\mathcal{S}}^2_{\mathrm{eo}}\right\rangle = \left(\frac{N\omega_{\mathrm{p}}dl}{c_0 n}\right)^2 \frac{\hbar}{4\pi^2\varepsilon_0 c_0}\int_{\Omega_R}^{\infty}\mathrm{d}\Omega\ \frac{\Omega}{n_\Omega w_0^2}|R(\Omega)|^2. \tag{1.106}$$

Here, we have used the paraxial quantization

$$\hat{E}_{\mathrm{THz},s}(\mathbf{r}_\perp,\Omega) = i\sqrt{\frac{\hbar\Omega}{4\pi\varepsilon_0 c_0 n_\Omega}}\sum_{l,p}\mathrm{LG}_{lp}(\mathbf{r}_\perp, r_\parallel = 0; k_\Omega)\hat{a}_{slp}(\Omega) \tag{1.107}$$

for the THz field [cf. Eq. (1.52)], so that its vacuum fluctuations are given by

$$\langle 0_{\mathrm{THz},s}|\hat{E}_{\mathrm{THz},s}(\mathbf{r}'_\perp,\Omega')\hat{E}^\dagger_{\mathrm{THz},s}(\mathbf{r}_\perp,\Omega)|0_{\mathrm{THz},s}\rangle = \frac{\hbar\Omega}{4\pi\varepsilon_0 c_0 n_\Omega}\delta(\mathbf{r}_\perp - \mathbf{r}'_\perp)\delta(\Omega-\Omega'). \tag{1.108}$$

Note that a cut-off for frequencies $\Omega \leq \Omega_R = c_0/(w_0 n_\Omega)$ has been introduced to account for diffraction losses. This cut-off also excludes any contribution from frequencies close to the optical phononic resonance of ZnTe crystals and thus enables the treatment of the ZnTe crystal as effectively transparent for all relevant THz frequencies. Thus, only the real part n_Ω of the refractive index needs to be taken into account and the quantization procedure explained in Sec. 1.3 is applicable. The shot noise part $\left\langle\hat{\mathcal{S}}^2_{\mathrm{sn}}\right\rangle = N$ is simply given by the average photon number inside the probe.

Equation (1.106) shows that the fluctuations of the polarization of the probe are enhanced due to the electro-optic process. The additional fluctuations are essentially given by the vacuum fluctuations of the THz field, gated in time and space through the probe. The transversal gating can be controlled by the beam waist of the probe inside the crystal, while the spatial gating along the propagation direction and the temporal gating are controlled by the phase matching and the temporal duration of the probe. It is therefore necessary to use sufficiently short and tightly focused pulses in order to increase the contribution stemming from the THz vacuum fluctuations. Additionally,

short crystals are needed to ensure good phase matching conditions over the majority of sampled frequencies.

Alternative theoretical descriptions of the electro-optic fluctuations, employing a Green's function formalism have been presented [50–52]. Here, the quantization of the THz field can be performed exactly for all THz frequencies, including the lower frequencies at the optical phononic resonances of ZnTe by including the polarization noise mentioned in Sec. (1.3).

Chapter 2

Subcycle squeezing from a time flow perspective

All results in this chapter have been published in Ref. [55]. The analytical solution according to the methods of characteristics in Appendix A.1 and the specific form of the conformal time for the half- and single-cycle pulse as well as Appendices A.2 and A.4 have been obtained during my Master thesis [56]. The connections to analogue gravity effects have been developed by myself and Thiago Lucena de Macedo Guedes. The theory on the modelling of the electro-optic process as well as the measurement of the other field quadrature and the time-dependent intensity flux have been developed by myself. The text, structure and notation has been edited slightly in order to keep the consistency with the other chapters.

2.1 Introduction

The quantum nature and spatio-temporal structure of light is exploited in many intriguing applications ranging from novel spectroscopy methods of complex many-body phenomena [29] to quantum information processing [57–59] and subwavelength lithography [60, 61]. In conventional optics, there was no control over the absolute phase of a light pulse with respect to its envelope. This situation changed abruptly with the advent of femtosecond frequency combs[62, 63]. The carrier-envelope phase is especially relevant for few-cycle pulses which are at the heart of attosecond technology and extreme nonlinear optics[64–66]. So far, this area has exploited coherent states of light which come closest to the classical picture of an electromagnetic field with well-defined amplitude and phase. Only recently, quantum optics was carried to an analogous level with subcycle analysis of the noise properties of infrared electric fields by electro-optic

sampling with femtosecond laser pulses[6–9, 49]. Here, the concept of a carrier-envelope phase loses its meaning because highly nonclassical states of light may exhibit excessive phase fluctuations or no well-defined phase at all. Instead, it is the relative timing of a quantum noise pattern with respect to a subcycle probe which gains relevance. Interesting and unexpected phenomena may arise when the physics of such synchronal states of light is explored on a subcycle scale.

One of the most fundamental nonclassical states of light is the squeezed vacuum [39, 67, 68], which enables sensitivity below the shot-noise limit in an interferometer [69–71], and can potentially improve [72, 73] the metrology of gravitational waves [74]. Stationary squeezed vacuum states carry a persisting flux of photons [75], whereas there is a finite number of photons contained in a pulsed state. Pulsed squeezed light [76] with many optical oscillation cycles was realized based on parametric down-conversion [77]. The case of the generation of pulsed broadband ultrashort squeezing [78–80] was analyzed in terms of a large set of single-frequency or broadband shaped temporal modes [78, 81–83], where each mode is characterized separately. The alternative time-domain approach based on electro-optic sampling provided first insights into the temporally resolved dynamics of few-cycle squeezing supported by a simplified theoretical description [8]. This theory was restricted to the low squeezing regime or selected points in time. Furthermore, it has not yet incorporated a finite probe pulse duration for the detection of the temporal quantum noise patterns. Here, we present methods that overcome these limitations by considering extremely short (in terms of optical cycles) pulses of squeezed vacuum light and provide a general theoretical picture of their generation and subcycle-resolved detection. We predict that the expected asymmetry between the anti-squeezed and squeezed temporal noise, well known in conventional quantum optics, can in fact be reversed for ultrabroadband driving fields which are also within reach of state-of-the-art experiments. Our results shed light on the interplay between the quantum nature of electromagnetic fields and general relativity, leading to creation of particles out of vacuum on ultrashort time scales.

We consider the setup depicted schematically in Fig. 2.1(a). A coherent mid-infrared electric driving field with a classical amplitude $\mathcal{E}(z,t)$ propagates along the z-axis and is polarized along the x-axis. It enters a thin transparent optical generation crystal (GX), of length l and centered at $z=0$, with a non-vanishing second-order nonlinearity $\chi^{(2)}$. Far from material resonances $\chi^{(2)}$ can be treated as a dispersionless tensor, which in the simplest case is reducible to a single effective nonlinear coefficient d. Inside the GX $\mathcal{E}(z,t)$ interacts with the co-propagating quantum electric field component $\hat{\varepsilon}(z,t)$, which is polarized along the y-axis, belongs to the same frequency range, and corresponds to the vacuum field when entering the crystal (there are no incoming

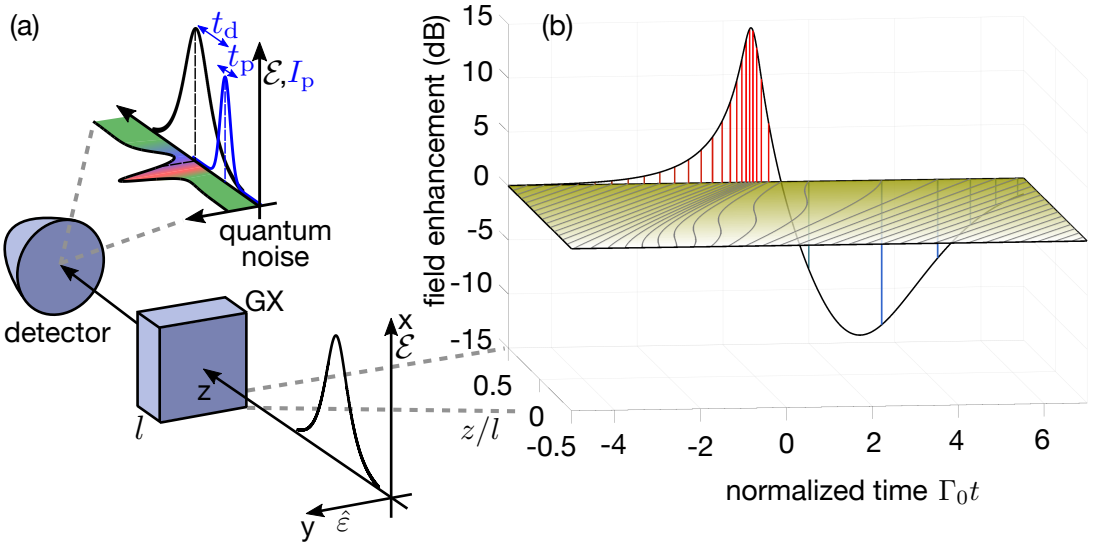

Figure 2.1: Scheme of the generation and detection setup and the corresponding evolution of the mid-infrared quantum field $\hat{\varepsilon}(z,t)$ inside the nonlinear crystal for a half-cycle mid-infrared driving field with effective squeezing strength $r = 5$. (a) A strong mid-infrared coherent field $\mathcal{E}(z,t)$ polarized along x-direction is sent into the nonlinear generating crystal (GX) of length l where it squeezes the co-propagating vacuum field $\hat{\varepsilon}(z,t)$. The quantum noise of the squeezed vacuum field is shown in the horizontal plane above the detector (green represents vacuum noise, red anti-squeezing and blue squeezing). The squeezed vacuum field is then detected using electro-optic sampling: a probe pulse polarized along x-direction with intensity envelope I_p plays the role of a temporal gating applied at various time points t_d. Statistical readout allows to obtain the time-resolved variance of $\hat{\varepsilon}(z,t)$. Subcycle resolution is achieved for sufficiently short probe pulse durations t_p. (b) Horizontal plane: Grey lines depict the world lines for $\hat{\varepsilon}(z,t)$ [determined by $\tau(z,t) = \mathrm{const}$, characteristic curves of Eq. (2.2)], shown for the case of a half-cycle driving field in Eq. (2.12) with duration Γ_0^{-1}. The equidistant spacing of the lines at the entrance is distorted as the quantum light propagates through the crystal. Vertical plane: Field enhancement at the crystal exit is shown together with the final spacing between the world lines. In the simplified picture, red (blue) lines correspond to anti-squeezing (squeezing).

photons with y-polarization). This gives rise to the y-component of the nonlinear polarization $\hat{P}^{(2)}(z,t) = -\epsilon_0 d\mathcal{E}(z,t)\hat{\varepsilon}(z,t)$, where ϵ_0 denotes the vacuum permittivity, but generates no x-component. Such a situation can be realized for various nonlinear crystals, e.g., for ZnTe in a configuration where the present unit vectors $\mathbf{e}_x$ and $\mathbf{e}_z$ would be aligned along the [001] and [110] crystallographic directions, respectively [84]. The driving field is assumed to be external but the situation is similar if this field is generated in the same crystal [8].

2.2 Wave equation

The nonlinear polarization $\hat{P}^{(2)}(z,t)$ provides a source term in the inhomogeneous wave equation for $\hat{\varepsilon}(z,t)$: $\left[\frac{\partial^2}{\partial z^2} - \frac{n^2}{c_0^2}\frac{\partial^2}{\partial t^2}\right]\hat{\varepsilon}(z,t) = \frac{1}{\epsilon_0 c_0^2}\frac{\partial^2}{\partial t^2}\hat{P}^{(2)}(z,t)$, where c_0 and n denote the vacuum speed of light and refractive index. We decompose $\hat{\varepsilon}(z,t) = \int_{-\infty}^{\infty} \mathrm{d}\Omega\ \hat{\varepsilon}(z;\Omega)e^{i(k_\Omega z - \Omega t)}$ and similarly $\mathcal{E}(z,t)$ and $\hat{P}^{(2)}(z,t)$ into plane waves [12], assuming an almost ideally linear dispersion $k_\Omega = \frac{n}{c_0}\Omega$. Here $\hat{\varepsilon}(z;\Omega) = \hat{\varepsilon}^\dagger(z;-\Omega)$ since the field is Hermitian. In the resulting frequency-domain integro-differential equation we assume that $\frac{\partial^2\hat{\varepsilon}(z;\Omega)}{\partial z^2}$ can be neglected in comparison with $k_\Omega\frac{\partial\hat{\varepsilon}(z;\Omega)}{\partial z}$, as for the slowly varying amplitude approximation (SVAA) [12, 30]. This leads to

$$\frac{\partial\hat{\varepsilon}(z;\Omega)}{\partial z} = -\frac{id\Omega}{nc_0}\int_{-\infty}^{\infty}\mathrm{d}\Omega_1\ \mathcal{E}^*(z;\Omega_1-\Omega)\hat{\varepsilon}(z;\Omega_1). \tag{2.1}$$

Integration over positive frequencies incorporates frequency-conversion processes, while integration over negative frequencies, with $\hat{\varepsilon}(z;\Omega) = \hat{\varepsilon}^\dagger(z;-\Omega)$, reflects parametric down-conversion processes[81]. Note that the assumption of a linear dispersion relation assures perfect phase matching [30] for the co-propagating waves. Most importantly, it prevents the distortion of the pulse shape [85] inside the GX. This approximation works well if the GX is thin enough and the dispersion nonlinearity is negligible in the relevant frequency range. For the following discussion of ultrabroadband mid-infrared fields with ZnTe as a typical nonlinear material, our estimations show that the GX should be thinner than 10-15 μm. However, the description of the generation process is quite general and may be applicable to other frequency ranges and appropriate nonlinear crystals [9, 47]. The perfect phase matching also constitutes the major difference to descriptions of conventional parametric down conversion setups commonly used for generation of squeezed vacuum states and entangled photon pairs [29, 81]. The corresponding bandwidth-limiting factor is absent in Eq. (2.1). The spatial (angular) separation of the outgoing photons may be neglected. All emitted photons propagate in z-direction.

Transforming Eq. (2.1) back into the time domain, by integrating on the left hand side $\int_{-\infty}^{\infty}\mathrm{d}\Omega\ \frac{\partial\hat{\varepsilon}(z;\Omega)}{\partial z}e^{i(k_\Omega z-\Omega t)} = \frac{\partial\hat{\varepsilon}(z,t)}{\partial z} + \frac{n}{c_0}\frac{\partial\hat{\varepsilon}(z,t)}{\partial t}$ and using on its right hand side the properties of the Fourier transform concerning products and derivatives, we obtain

$$\frac{\partial\hat{\varepsilon}}{\partial z} = \frac{d}{nc_0}\left[\frac{\partial\mathcal{E}}{\partial t}\hat{\varepsilon} + \left(\mathcal{E} - \frac{n^2}{d}\right)\frac{\partial\hat{\varepsilon}}{\partial t}\right]. \tag{2.2}$$

Note that as a result no central frequency and corresponding amplitude or envelope [85] were introduced in the time domain, in contrast to the conventional SVAA [30, 86, 87]. Therefore, also few-cycle and subcycle fields without unambiguously defined carrier

frequency and phase can be described by this approach. Essentially, the way to obtain Eq. (2.2) may be considered as a broadband version of the SVAA [12] (its limits of validity are discussed in Appendix A.2).

2.3 Interpretation in terms of accelerated reference frames

Equation (2.2) can be solved analytically by using the method of characteristics, according to which the initial conditions of the partial differential equation of interest are propagated along characteristic curves [see Appendix A.1]. To give a physical interpretation, it is insightful to realize that there are gravitational analogues of these curves termed world lines [88]. The analogy is based on the fact that the light-driven time dependence of the refractive index, leading to non-linear optical effects, has a closely related counterpart in general relativity [88, 89]. With the ansatz $\hat{\varepsilon}(z,t) = \hat{A}(z,t)\exp[i\phi(z,t)]$, with ϕ changing in space and time faster than $\hat{A}$, it is possible to rewrite either the mentioned inhomogeneous wave equation or Eq. (2.2) directly in terms of $k \equiv \nabla\phi$ and $\omega \equiv -\partial\phi/\partial t$. Separating terms that scale with different powers of the wavelength, to the lowest order in $d\mathcal{E}$ we obtain the same dispersion relation in both cases:

$$k^2 - \Big[\frac{n^2}{c_0^2} - \frac{2d\mathcal{E}}{c_0^2}\Big]\omega^2 = 0. \tag{2.3}$$

In general relativity the dispersion relation is given by the light cone equation $g^{\mu\nu}k_\mu k_\nu = 0$, where $k_\mu = (\omega/c_0, -\mathbf{k})$ is the four-momentum vector. This means that the metric tensor $g_{\mu\nu}$ can be extracted from Eq. (2.3), resulting (for the '1+1' space-time) in the interval

$$\mathrm{d}s^2 = g_{\mu\nu}\mathrm{d}x^\mu \mathrm{d}x^\nu = \frac{c_0^2}{n^2 - 2d\mathcal{E}}\mathrm{d}t^2 - \mathrm{d}z^2. \tag{2.4}$$

The world lines for the evolution of $\hat{\varepsilon}$ in the crystal with a refractive index modulated by $\mathcal{E}$ can be calculated with the help of the null geodesic equations[88] coinciding in their form with the equations for the characteristic curves. We summarize the conceptual correspondence between nonlinear (quantum) optics and general relativity in Table 2.1.

Each world line $z(t;t_0)$ can be uniquely represented via the corresponding implicit equation $\tau(z,t) = t_0$ with its own constant t_0. Specifically, at the crystal entrance, $z = -l/2$, we have $\tau(-l/2,t) = t = t_0$. The change of the density of the world lines upon propagation through the crystal at each fixed spatial position z [see Fig. 2.1(b)] determines the resulting difference in the flow of the local time $\tau(z,t)$ with respect to the lab time t. Note that $\tau(z,t)$ monotonically increases with t. Such a reparametrization of time can be formally introduced in connection with a conformal mapping $x^\mu \to x'^\mu$,

Nonlinear (quantum) optics	General relativity
Driving field $\mathcal{E}$ changes the effective refractive index, $n_{\text{eff}}^2 = n^2 - 2d\mathcal{E}$.	Massive/energetic bodies deform space-time, thus changing the metric $g_{\mu\nu}$, cf. Eq. (2.4).
Excitations of the field modes propagate/ evolve along characteristic lines.	Point-like bodies /particles move along world lines.
Time-dependent refractive index induces creation of photons in previously unoccupied modes.	Time-dependent metric leads to particle creation even in vacuum.

Table 2.1: Comparison between physically analogue frameworks: nonlinear (quantum) optics and general relativity.

i.e. a transformation preserving orientation and angles locally, particularly the shape of the light cones (see Appendix A.3). The existence of such a mapping as well as a similar reparametrization of time used in cosmology, when transforming between a curved and a flat (Minkowski) metric [90], suggests terming $\tau(z,t)$ *conformal time*.

Denoting the quantum field at the entrance of the generation crystal as $\hat{\varepsilon}_{\text{in}}(t) \equiv \hat{\varepsilon}(z = -l/2, t)$, the solution of equation (2.2) can be found as

$$\hat{\varepsilon}(z,t) = \frac{\partial\tau(z,t)}{\partial t}\hat{\varepsilon}_{\text{in}}(\tau(z,t)). \tag{2.5}$$

Note that back in the frequency domain Eq. (2.5) represents a broadband (position-dependent) Bogoliubov transformation for the creation and annihilation operators:

$$\hat{a}(z;\Omega) = \int_0^\infty \mathrm{d}\Omega'\, p_z(\Omega,\Omega')\hat{a}_{\text{in}}(\Omega') + \int_0^\infty \mathrm{d}\Omega'\, q_z(\Omega,\Omega')\hat{a}_{\text{in}}^\dagger(\Omega') \tag{2.6}$$

with coefficients $p_z(\Omega,\Omega') = -q_z(\Omega,-\Omega') = \frac{\sqrt{|\Omega'|}}{2\pi\sqrt{|\Omega|}}\int_{-\infty}^{\infty} e^{i\Omega[\tau^{-1}(z,t)-nz/c_0]-i\Omega'[t+nl/(2c_0)]}\mathrm{d}t$, where τ^{-1} denotes the inverse function of τ with respect to its second argument. For the vacuum input $\hat{\varepsilon}_{\text{in}} = \hat{\varepsilon}_{\text{vac}}$, the form of the outgoing squeezed vacuum field resulting from Eq. (2.5) at the exit of the crystal can be attributed to two different effects. Firstly, due to the driving field $\mathcal{E}(z,t)$ the wave propagation of the incoming vacuum field inside the crystal is governed by the conformal time $\tau(z,t)$. This effect is illustrated by the world lines in the horizontal plane of Fig. 2.1(b). Secondly, there is a modulation of the amplitude of the quantum field by the inverse conformal factor [90] $\frac{\partial\tau(z,t)}{\partial t}$. This factor is shown in the vertical plane of Fig. 2.1(b) at the crystal exit and is essentially related to the behaviour of $\frac{\partial\mathcal{E}(z,t)}{\partial t}$ (cf. Ref. [8]), as discussed below. Note that the quantum field is enhanced (suppressed) in the same time segments where the density of

the world lines is increased (decreased), see vertical lines in Fig. 2.1(b). In a simplified picture, neglecting the effect of the modified density of the world lines, the amplitude modulation of the quantum field leads to a corresponding modulation in the temporal profile of its quantum noise. The quantum fluctuations of $\hat{\varepsilon}$ are suppressed beneath the vacuum level in certain time segments while exceeding it in the neighbouring segments. Squeezing (anti-squeezing) can be connected to the deceleration (acceleration) of the local flow of the conformal time $\tau(z,t)$, determined by its derivative with respect to the lab time t.

2.4 Quantum electro-optic sampling

In this section, we will show how the squeezed vacuum fluctuations of the outgoing quantum electric field $\hat{\varepsilon}_{\mathrm{out}}(t) = \hat{\varepsilon}(z = l/2, t)$ can be measured using quantum electro-optic sampling. As explained in Sec. 1.5, electro-optic sampling is generally based on upconversion of the mid-infrared (THz, multi-THz) field to the near-infrared (NIR) range. More specifically, a second-order nonlinear interaction provides mixing between the mid-infrared (MIR) field and an ultrafast gate pulse of the probe field, which is of duration shorter than the half-cycle of the sampled field [42, 87]. Scanning the relative delay t_{d} between the MIR field and the centre of the probe pulse allows for mapping out the temporal evolution of the MIR waveform. It is extracted from the polarization state of the NIR photons, which are absorbed and counted in a pair of fast (i.e. ~ 1 GHz electronic bandwidth) balanced photodetectors. The technique can also be operated in the regime of statistical readout, where probability distributions based on millions of individual NIR pulses can be analyzed at each temporal delay between the MIR field and the gate pulse, providing access to the temporally resolved quantum statistics of the sampled field [6, 8, 9].

The variance of the outgoing quantum field $\hat{\varepsilon}'_{\mathrm{out}}(t')$ is calculated as a function of the relative delay time t_{d} with respect to the centre of an ultrashort higher-frequency probe pulse $\mathcal{E}'_{\mathsf{p}}(t')$. For convenience, we use a retarded reference frame with $t' = t - \frac{n}{c_0} z$, $z' = z$, $\tau'(z', t') = \tau(z,t) + \frac{nl}{2c_0}$, and $\mathcal{E}(z,t) = \mathcal{E}'(t')$ for all electric fields. The resulting operator of the sampled field is given by

$$\hat{\varepsilon}^{(\mathrm{d})}_{\mathrm{out}}(t_{\mathrm{d}}) = \int_{-\infty}^{\infty} \mathrm{d}t' \; R(t_{\mathrm{d}} - t') \hat{\varepsilon}'_{\mathrm{out}}(t'). \tag{2.7}$$

The detector function $R(t_{\mathrm{d}})$ is determined by the normalized intensity of the probe field that for a fast oscillating probe field can be replaced by the normalised intensity

envelope:

$$R(t_{\mathrm{d}}) = \frac{\left|\mathcal{E}'_{\mathsf{p}}(t_{\mathrm{d}})\right|^2}{\int_{-\infty}^{\infty}\mathrm{d}t'\,\left|\mathcal{E}'_{\mathsf{p}}(t')\right|^2} \approx \frac{I'_{\mathsf{p}}(t_{\mathrm{d}})}{\int_{-\infty}^{\infty}\mathrm{d}t'\,I'_{\mathsf{p}}(t')}. \tag{2.8}$$

Via Eq. (2.5) the conformal time directly links the squeezed vacuum field at the exit of the crystal at time t to the vacuum field at the entrance at time $\tau_{\mathrm{out}}(t) = \tau(z = l/2, t)$. According to Eq. (2.5) the modification of the variance of the quantum electric field after passing the crystal is given by $(\mathrm{d}\tau_{\mathrm{out}}/\mathrm{d}t)^2$ if considered at a fixed time moment. Experimentally, the information about the quantum field is collected over a finite time interval controlled via the duration of the probe pulse t_{p} [cf. Eq. (2.7)]. This is a significant aspect because apart from the change in its amplitude the quantum field of the incoming vacuum is effectively subjected to a modified flow of time at the crystal exit, as can be seen from Eq. (2.5). Alternatively we can say that in a reference frame using the conformal time $\tau_{\mathrm{out}}(t)$ in place of the lab time t the probe pulse shape and duration are modified according to the flow of $\tau_{\mathrm{out}}(t)$. This is evident if $\hat{\varepsilon}'_{\mathrm{out}}(t')$ in Eq. (2.7) is expressed via the incoming quantum field $\hat{\varepsilon}_{\mathrm{in}}(t)$ in the original reference frame as

$$\hat{\varepsilon}^{(\mathrm{d})}_{\mathrm{out}}(t_{\mathrm{d}}) = \int_{-\infty}^{\infty}\mathrm{d}t\,R\big(t_{\mathrm{d}} - \tau^{-1}_{\mathrm{out}}(t)\big)\hat{\varepsilon}_{\mathrm{in}}(t), \tag{2.9}$$

where $x = \tau^{-1}_{\mathrm{out}}(y)$ denotes the inverse function of $y = \tau_{\mathrm{out}}(x)$.

Let us consider the case where the incoming field corresponds to the vacuum state. Then Eq. (2.9) shows that sampling of the generated squeezed field by the probe pulse in an inertial reference frame can be alternatively viewed as sampling of the bare vacuum field in a reference frame with a non-uniform time flow given by $\tau^{-1}_{\mathrm{out}}(t)$. In the latter reference frame the shape of the used probe pulse is then effectively transformed.

In order to characterize the dynamics of the resulting quantum fluctuations $V(t_{\mathrm{d}}) = \left\langle[\hat{\varepsilon}^{(\mathrm{d})}_{\mathrm{out}}(t_{\mathrm{d}})]^2\right\rangle$ we evaluate the relative detected variance (RDV) that is given by

$$\mathrm{RDV}(t_{\mathrm{d}}) = \frac{V(t_{\mathrm{d}}) - (\Delta\hat{\varepsilon}_{\mathrm{vac}})^2}{(\Delta\hat{\varepsilon}_{\mathrm{vac}})^2}. \tag{2.10}$$

Here, $(\Delta\hat{\varepsilon}_{\mathrm{vac}})^2 = \left\langle[\hat{\varepsilon}^{(\mathrm{d})}_{\mathrm{in}}]^2\right\rangle$ denotes the detected variance of the incoming quantum vacuum field, which does not depend on the delay time t_{d}.

The experimental realization of quantum electro-optic sampling involves an additional contribution to the detected variance originating from the shot noise of the probe pulse. This contribution is an important issue but is tractable experimentally by refer-

encing the signal with respect to the vacuum level. In the considered situation, this can be accomplished by producing sets of two immediately consecutive measurements with and without the squeezing process initiated in the GX crystal, respectively. Therefore, the relevant quantity measured experimentally, and connected to the calculated RDV, is the relative differential noise (RDN) [8], incorporating the shot noise (SN) contribution $(\Delta\mathcal{E}_{\mathrm{p,SN}})^2$. The RDN is given by

$$\mathrm{RDN}(t_\mathrm{d}) = \left(\sqrt{V(t_\mathrm{d})} - \Delta\hat{\varepsilon}_\mathrm{vac}\right) \frac{\Delta\hat{\varepsilon}_\mathrm{vac}}{(\Delta\mathcal{E}_{\mathrm{p,SN}})^2} \tag{2.11}$$

[see Eq. (2.10) for comparison].

The detection setup can be operated under conditions when the probe pulse intensity is high enough so that the shot noise equivalent field amplitude $\Delta\mathcal{E}_{\mathrm{p,SN}}$ (inversely proportional to the square root of the intensity of the probe field) is reduced to an appropriate level, which is still higher than but comparable with both the root mean square values of the detected vacuum field $\Delta\hat{\varepsilon}_\mathrm{vac}$ and the deviation induced due to the squeezing $\sqrt{V(t_\mathrm{d})} - \Delta\hat{\varepsilon}_\mathrm{vac}$. Additionally a large enough number of repetitions (millions in practice) are required to suppress the uncertainty in the detected variances for the generated quantum field and the bare vacuum. Under such conditions, an appropriate signal-to-error ratio can be reached for the RDN. Knowing the particular relevant probe intensity determining the shot noise level, one can straightforwardly recalculate the RDV from the RDN and vice versa.

For the corresponding calculations in this paper we used a Gaussian shape of the probe intensity envelope with the FWHM duration t_p so that $R(t_\mathrm{d}) = \frac{2\sqrt{\ln 2}}{\sqrt{\pi}t_\mathrm{p}} \exp\left(-\frac{4\ln 2\, t_\mathrm{d}^2}{t_\mathrm{p}^2}\right)$.

2.5 Half-cycle pulse driving

In this section, we convey the essence of the effect and its detection for the case of an idealized half-cycle driving pulse; in the next section, we study the single-cycle case. Figure 2.2(a) depicts the evolution of the conformal time in the retarded reference frame through the crystal resulting from a half-cycle driving field of the form (see Appendix A.4)

$$\mathcal{E}'(t') = \mathcal{E}_0 \,\mathrm{sech}(\Gamma_0 t'), \tag{2.12}$$

where $\mathcal{E}_0$ is the amplitude of the field and Γ_0 determines its duration. It is useful to introduce a dimensionless parameter $r = |\mathcal{E}_0 d|\Gamma_0 l/(nc_0) > 0$ which characterizes the effective strength of the driving inducing the squeezing and we call squeezing strength. At the entrance of the crystal the conformal time matches the lab time: $\tau(z = -l/2, t) =$

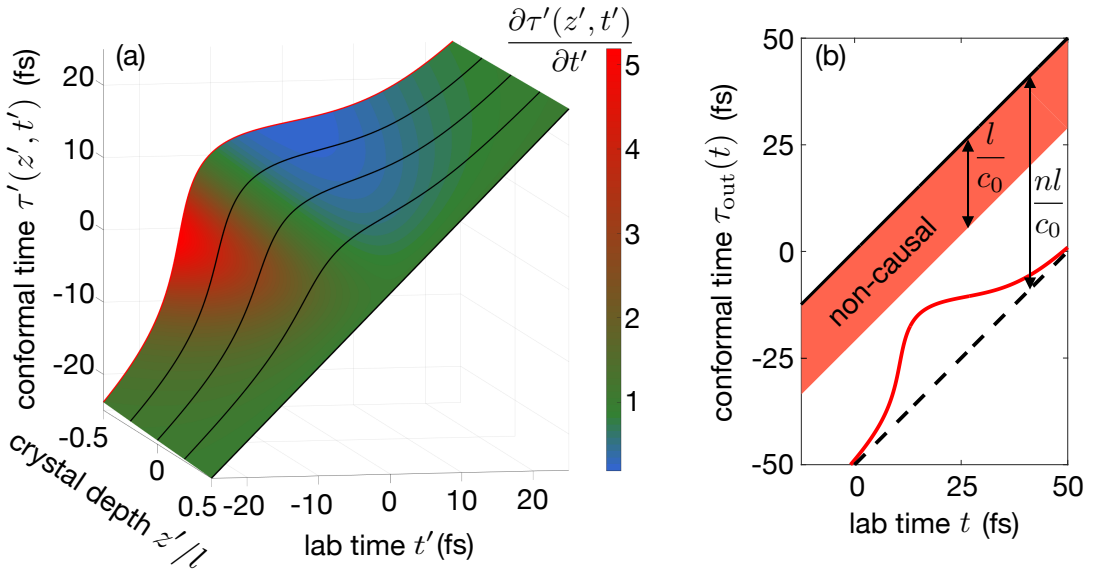

Figure 2.2: Behaviour of the conformal time with respect to the lab time illustrated for the half-cycle pulse [cf. Eq. (2.12)] with $r = 5$ and $\Gamma_0/(2\pi) = 26$ THz. (a) Conformal time $\tau'(z', t')$ as a function of the lab time t' and the propagation length inside the crystal $z' = z$. The retarded reference frame is used. $\tau'(z', t')$ coincides with t' at the entrance of the crystal $z' = -l/2$ and starts to deviate from it for $z' > -l/2$. The graph is coloured according to the values of the inverse conformal factor $\frac{\partial\tau'(z',t')}{\partial t'}$. In the simplified picture, which does not yet incorporate the detection process influenced also by the change in the local density of the world lines, departure from green towards blue (red) leads to squeezing (anti-squeezing) of the vacuum fluctuations. The black lines support visualization of the surface. (b) Red line: final conformal time $\tau_{\rm out}(t) = \tau(z = l/2, t)$ at the exit of the crystal as a function of the lab time t, shown in the original reference frame. Dashed black line: same without the driving field — delayed by nl/c_0 with respect to t. Full black line: the run of the lab time t is shown for comparison. Values of $\tau_{\rm out}(t)$ must stay below the red area defined by the delay time $t_{\rm d,0} = l/c_0$ in order not to violate causality (cf. Appendix A.2).

t and $\tau'(z' = -l/2, t') = t'$. With the interaction turned on, while the quantum field propagates through the crystal its conformal time starts to deviate from the lab time.

Figure 2.3(b) depicts the RDV for the case of the half-cycle pulse Eq. (2.12), a very short detection time $t_{\rm p} = 0.49$ fs and different squeezing strengths r. For $r = 0.1$, RDV($t_{\rm d}$) is an almost perfectly odd function (red line) with respect to the centre of the driving pulse at $t_{\rm d} = 0$ fs. In this case, the temporal trace nearly coincides with the waveform proportional to the third derivative of the driving field $\mathrm{d}^3\mathcal{E}'(t_{\rm d})/\mathrm{d}t_{\rm d}^3$ (dashed black line). The latter corresponds to the exact analytic solution in the limit of small r and $t_{\rm p}$, which can be obtained via the squeezing operator in the frequency domain[88]. This dynamics differs from the simplified picture where for each fixed time moment

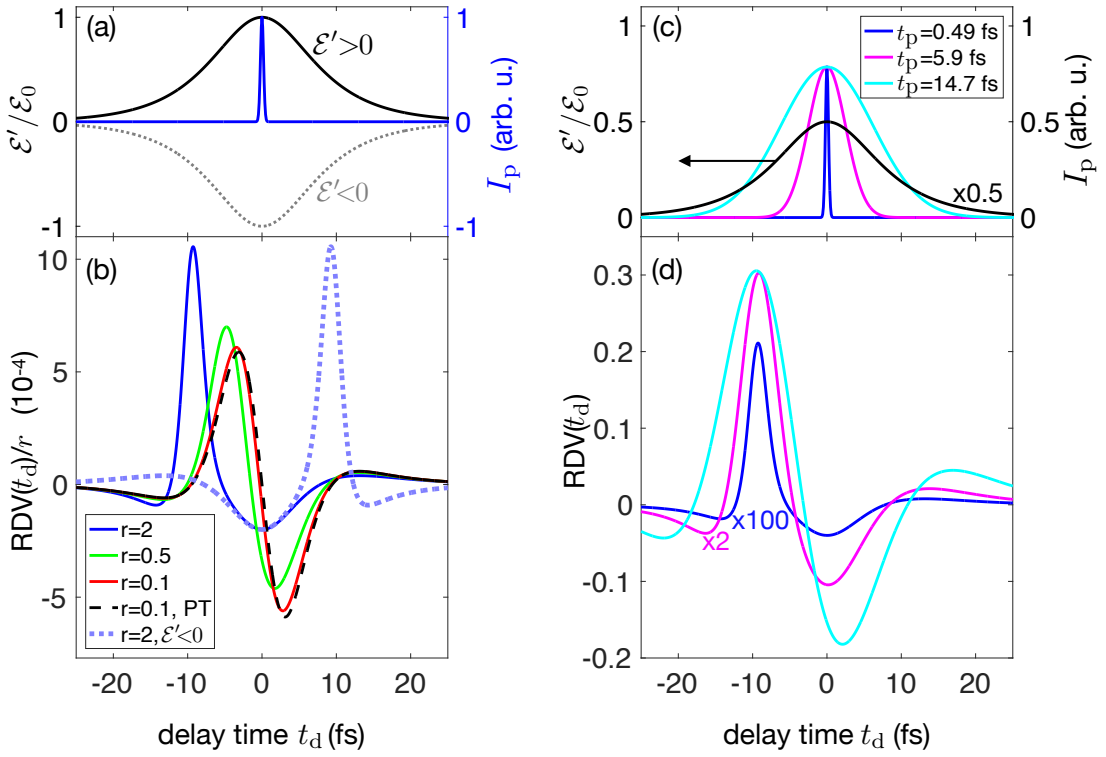

Figure 2.3: Relative detected variance (RDV) in dependence on the strength of the half-cycle driving field and probe pulse duration. (a) Temporal profiles of the driving field $\mathcal{E}'$ with two opposite polarities and probe pulse intensity envelope I_p with duration $t_\mathrm{p} = 0.49$ fs (blue). (b) Dynamics of the normalized RDV for a fixed probe pulse duration $t_\mathrm{p} = 0.49$ fs and different squeezing strengths r=0.1 (red), 0.5 (green) and 2 (blue), proportional to the driving field amplitude. The normalization by r is chosen to keep the signal magnitude in the same range. For comparison, the exact analytical result within the first-order perturbation theory (PT) in r and limit of vanishing t_p is shown (black dashed line). The light blue dotted line shows the RDV for the half-cycle pulse with $\mathcal{E}' < 0$ for $r = 2$. (c) Temporal profiles of the driving field $\mathcal{E}'$ (black, normalized by its amplitude $\mathcal{E}_0$) and probe pulse intensity envelope I_p for different probe pulse durations $t_\mathrm{p} = 0.49$ fs (blue), 5.9 fs (magenta) and 14.7 fs (cyan) are shown on the same time scale as the RDV. (d) Dynamics of the RDV for a fixed $r = 2$ and the same probe pulse durations as in the upper panel (note different scaling factors).

the variance of the squeezed vacuum field is determined by $[\mathrm{d}\tau_\mathrm{out}/\mathrm{d}t]^2$ and in the low squeezing regime ($r \ll 1$) leads to temporal profiles following the first derivative $\mathrm{d}\mathcal{E}'(t_\mathrm{d})/\mathrm{d}t_\mathrm{d}$ [8]. Notice that the deviation becomes less significant if multi-cycle, more narrowband driving fields are considered.

For small r, the RDV scales linearly with r and therefore remains symmetric. A build-up of asymmetry between the time segments with reduced and excess quantum noise can be clearly observed when r is increased. Firstly, we can see that the magnitude

of the detected quantum fluctuations becomes more pronounced in the anti-squeezing period with respect to the squeezing period. This can be attributed to the fact that the conformal time $\tau_{\mathrm{out}}(t)$ must always increase monotonically with t. As the slope of $\tau_{\mathrm{out}}(t)$ approaches zero, the flow of time comes to a halt and according to Eq. (2.5) $\hat{\varepsilon}_{\mathrm{out}}(t)$ must vanish. In the simplified picture, looking only at the prefactor in Eq. (2.5), this would lead to an almost complete elimination of the quantum noise and squeezing limited by 100%. In contrast, acceleration in the flow of time in principle may lead to arbitrarily large prefactors determining the magnitude of $\hat{\varepsilon}$ in Eq. (2.5) and therefore to an arbitrarily strong enhancement of the quantum noise. In the full picture including detection, the decrease (increase) caused by the prefactor in Eq. (2.5) is partly counteracted by the slower (quicker) flow of the conformal time in $\hat{\varepsilon}_{\mathrm{in}}(\tau_{\mathrm{out}}(t))$ in the case of squeezing (anti-squeezing). The duration of the probe pulse seen by the incoming vacuum field thus effectively becomes smaller (larger) for squeezing (anti-squeezing) and the detected variance $V(t_{\mathrm{d}})$ increases (decreases) due to this effect [6]. Equivalently, the effect of the lower (higher) local world line densities [see Fig. 2.1(b)] alone would enhance (suppress) the detected quantum noise. Still, after the unperturbed vacuum contribution $(\Delta\hat{\varepsilon}_{\mathrm{vac}})^2$ is subtracted in Eq. (2.5), the asymmetry in the RDV(t_{d}) is preserved to a large extent for sufficiently short detection times t_{p}. Secondly, with increasing r the time segments of squeezing become broader while the time segments of anti-squeezing narrow down. This additional asymmetry can be comprehended from Fig. 2.2(b). It is clear that the time intervals with steep slopes in the flow of the conformal time $\tau_{\mathrm{out}}(t)$ (anti-squeezing) take less space on the horizontal axis, representing the lab time t, than the intervals with flat slopes (squeezing). This is what we observe for the case of r=2 in Fig. 2.3(b) (blue line). Uniquely to the strong squeezing in the time domain, polarity reversal of the driving field [Fig. 2.3(a)] does not change the position of the squeezing valley while reversing the arrival time of the anti-squeezing burst.

In Fig. 2.3(d), the dynamics of the RDV is shown for different probe pulse durations t_{p} and a fixed squeezing strength $r = 2$. As t_{p} grows [cf. Fig. 2.3(c)], higher frequencies in $\hat{\varepsilon}_{\mathrm{out}}(t)$ are not captured anymore leading to a flattening of the detected temporal traces. The narrow anti-squeezing peaks are affected more strongly by such changes than the valley regions of squeezing. When the probe pulse duration approaches the oscillation time of the driving field, the asymmetry is almost completely lost.

2.6 Single-cycle driving

We now switch our attention to the case of a single-cycle driving pulse [Fig. 2.4(a)]. Figure 2.4(b) shows the resulting dynamics of the RDV, also in terms of the degree of

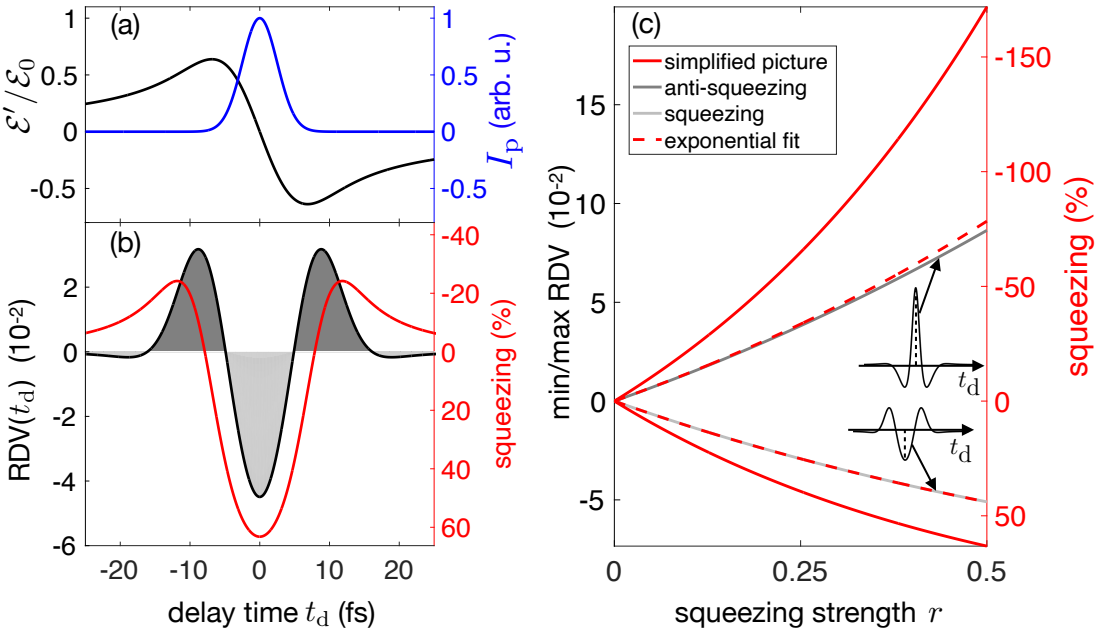

Figure 2.4: Pulsed squeezing for single-cycle driving. (a) Temporal profiles of the driving field $\mathcal{E}'(t') = \mathcal{E}_0 \left[\exp\left(-\Gamma_0^2 t'^2\right) - 1\right]/(\Gamma_0 t')$ with $\Gamma_0/(2\pi) = 26$ THz (black) and probe pulse intensity envelope I_p with $t_\mathrm{p} = 5.9$ fs (blue). (b) Corresponding dynamics of the RDV for $r = 0.5$ (black line). Dark grey (light grey) areas denote anti-squeezing (squeezing). The red line depicts the noise trace obtained within the simplified picture, where the degree of squeezing (right axis) can be extracted directly from the ratio between the variances of the squeezed and bare vacuum field at each $t_\mathrm{d} = t$. Negative values for the degree of squeezing correspond to anti-squeezing. (c) Values of the RDV at $t_\mathrm{d} = 0$ fs plotted against r for two different polarities of the driving field. Depending on the polarity, it is the maximum (anti-squeezing, dark grey line, upper inset) or the minimum (squeezing, light grey line, lower inset) value of the RDV. The degree of squeezing (dashed red lines) results from an exponential fit (cf. Appendix A.5). The RDV in (b) is then rescaled according to this fit to obtain the degree of squeezing at arbitrary times. The red lines in (c) show the degree of squeezing calculated within the simplified picture. For a vanishing probe pulse duration $t_\mathrm{p} \to 0$, the squeezing and anti-squeezing curves obtained from the RDV converge towards this result.

squeezing (see Appendix A.5). For the given amplitude of the driving field, the maximum positive degree of squeezing amounts to 49.6% while the minimum negative degree of squeezing (corresponding to anti-squeezing) constitutes only -35%. Therefore, the previously described asymmetry in favour of higher absolute values for anti-squeezing is reversed in this case. At first sight, one might wonder whether Heisenberg's uncertainty principle is violated in the described situation. Through the inspection of the RDV trace for the polarity-switched drive [inset in Fig. 2.4(c)], we discover that the amplitude of anti-squeezing is in fact nearly twice that of the squeezing [Fig. 2.4(b)].

It is only in this temporally non-local sense that we are able to restore the familiar dependence of quantum noise on the squeezing strength [Fig. 2.4(c)], and hence directly recover Heisenberg's uncertainty principle.

The calculated values of the RDV typically are small compared to the values of RDV and respective degrees of squeezing that would follow directly from the simplified picture [see Fig. 2.4(b)]. The reason for this is that the RDV [cf. Eq. (2.10)] is defined as the relative difference between the detected variance of the generated field and that of the unperturbed vacuum fluctuations. In order to resolve the signal in the time-domain the probe duration has to be much shorter than the typical time scales of the signal. Thus the frequency spectrum of the probe has to be much broader than that of the coherent field driving the squeezing. This means that the probe pulse will not only sample modes at the frequencies that are affected by the driving field but also modes at higher frequencies which remain untouched. Therefore, the contribution of the unperturbed vacuum fluctuations to the RDV has to be significantly larger than the contribution from the frequency range affected by the generation process in order to appropriately resolve the temporal squeezing pattern. This can be interpreted as an admixture of vacuum fluctuations to the signal that can be modelled by losses. However, it is important to note that rather than being losses that can be avoided, these losses are inherent to the measurement process and are necessary in order to appropriately resolve the signal in time. Nevertheless, losses do not necessarily represent an obstacle for the reconstruction of the degree of the generated squeezing [8], which is shown in Fig. 2.4(c).

2.7 Other field quadrature and time-dependent intensity flux

In order to analyze further the quantum aspects of the generated signals in our time-resolved detection theory, it is elucidating to consider the positive $\hat{\varepsilon}'^{(+)}_{\mathrm{out}}(t')$ and negative $\hat{\varepsilon}'^{(-)}_{\mathrm{out}}(t')$ frequency parts [4] of the generated quantum field $\hat{\varepsilon}'_{\mathrm{out}}(t') = \hat{\varepsilon}'^{(+)}_{\mathrm{out}}(t') + \hat{\varepsilon}'^{(-)}_{\mathrm{out}}(t')$. These parts contain only annihilation or only creation operators, respectively. The sampling of the corresponding field parts, which are non-Hermitian, can be performed by combining the information on the full field itself $\hat{\varepsilon}'_{\mathrm{out}}(t')$ and the same field with $\pi/2$-shifted carrier-envelope phase $\hat{\varepsilon}'_{\mathrm{out},\frac{\pi}{2}}(t')$: $\hat{\varepsilon}'^{(\pm)}_{\mathrm{out}}(t') = \left[\hat{\varepsilon}'_{\mathrm{out}}(t') \mp i\hat{\varepsilon}'_{\mathrm{out},\frac{\pi}{2}}(t')\right]/2$. Such a phase shift can be implemented experimentally by inserting an appropriate broadband carrier-envelope phase shifter [91] or in a variation of the electro-optic detection setup [92]. Mathematically, the corresponding operation represents the Hilbert transform [93] of the original generated field $\hat{\varepsilon}'_{\mathrm{out}}(t')$. In the time-resolved detection we

get

$$\hat{\varepsilon}^{(\mathrm{d})}_{\mathrm{out},\frac{\pi}{2}}(t_{\mathrm{d}}) = \int_{-\infty}^{\infty} \mathrm{d}t'\; R(t_{\mathrm{d}} - t')\hat{\varepsilon}'_{\mathrm{out},\frac{\pi}{2}}(t') = \int_{-\infty}^{\infty} \mathrm{d}t'\; R_{\frac{\pi}{2}}(t_{\mathrm{d}} - t')\hat{\varepsilon}'_{\mathrm{out}}(t'), \tag{2.13}$$

where $R_{\frac{\pi}{2}}(t)$ is obtained from $R(t)$ via the shift of the carrier-envelope phase by $\pi/2$. In the frequency domain, $R_{\frac{\pi}{2}}(\omega) = iR(\omega)$ for $\omega > 0$ and $R_{\frac{\pi}{2}}(\omega) = -iR(\omega)$ for $\omega < 0$. We can also express $\hat{\varepsilon}^{(\mathrm{d})}_{\mathrm{out},\frac{\pi}{2}}(t_{\mathrm{d}})$ via the input field $\hat{\varepsilon}_{\mathrm{in}}(t)$, in the same way as in Eq. (2.9). Measurements on $\hat{\varepsilon}'_{\mathrm{out}}(t')$ and $\hat{\varepsilon}'_{\mathrm{out},\frac{\pi}{2}}(t')$ can be performed simultaneously, in parallel, after a beam splitter. Note that in the described detection scheme, giving local temporal access to the generated quantum field, it is more natural and advantageous to operate with $\hat{\varepsilon}'^{(-)}_{\mathrm{out}}(t')$ and $\hat{\varepsilon}'^{(+)}_{\mathrm{out}}(t')$ in place of the time-domain version of the creation $a^{\dagger}(t')$ and annihilation $a(t')$ operators, which are also possible to introduce [93]. This access enables deeper study of the intrinsically quantum properties of the generated field. For example, taking the input vacuum field having zero intensity flux our generation process leads to appearance of the time-dependent short-living intensity flux, which is not possible to replicate with stochastical quasi-classical models for the field. Figure 2.5(a) shows the time-dependent detected intensity flux $\langle \hat{\varepsilon}^{(-),(\mathrm{d})}_{\mathrm{out}}(t_{\mathrm{d}})\hat{\varepsilon}^{(+),(\mathrm{d})}_{\mathrm{out}}(t_{\mathrm{d}})\rangle$ of the squeezed vacuum field generated by the half-cycle driving [Eq. (2.12)]. In Fig. 2.5(b) we illustrate the corresponding dynamics of the RDV for the generated squeezed vacuum field and its counterpart with $\pi/2$-shifted carrier-envelope phase ("conjugated quadrature" in the time domain), which is possible to detect simultaneously.

2.8 Conclusion

Our work provides a consistent time-domain theory of the generation and sub-cycle-resolved detection of ultrabroadband waveforms of pulsed squeezed radiation, linking these processes directly to a change in the local flow of time induced by the coherent driving field. This constitutes a non-perturbative analytical solution for the operator of the generated squeezed vacuum field and the electro-optically sampled traces of its quantum noise. This solution is valid at any time and also in the high-driving regime, restricted only by conditions underlying the broadband version of the slowly varying amplitude approximation and causality. We applied our theory to predict time traces of the detected variance and corresponding degrees of squeezing belonging to ultrashort squeezed vacuum fields created by half-cycle and single-cycle driving. The results for the detected variance show that the use of electro-optic sampling for a time-resolved measurement of the noise pattern of a squeezed field inherently introduces an admixture of vacuum fluctuations. However, the asymmetries between squeezing and

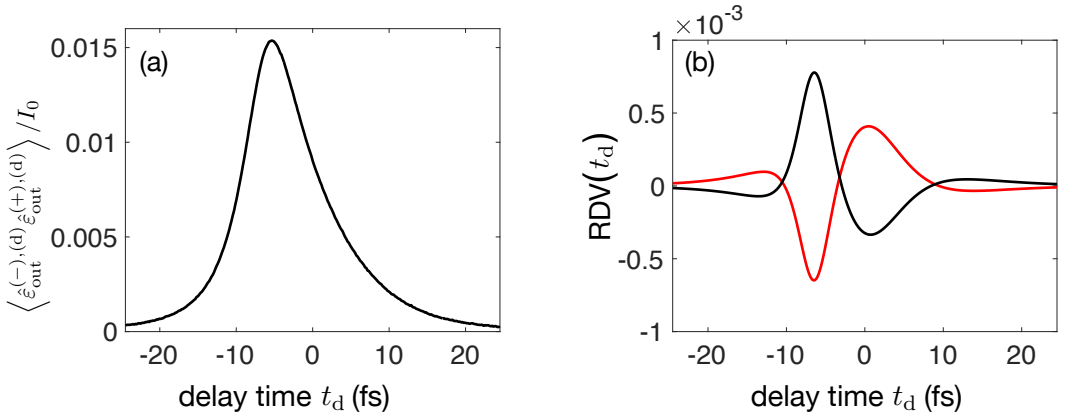

Figure 2.5: (a) Dynamics of the detected intensity flux, normalized by $I_0 = \hbar\Gamma_0^2/(4\pi n\varepsilon_0 c_0 A)$. (b) Comparison of the RDV dynamics for $\hat{\varepsilon}'_{\mathrm{out}}(t')$ (black line) and $\hat{\varepsilon}'_{\mathrm{out},\frac{\pi}{2}}(t')$ (red line). The squeezing strength for the generated pulsed squeezed vacuum state is $r = 1$ and other generation and detection parameters are as in Fig. 2.3(a).

anti-squeezing are preserved by this measurement technique for sufficiently short probe pulses. Finally, we theoretically predict an effect that at first glance looks paradoxical: the conventionally observed asymmetry between squeezing and anti-squeezing can be reversed for specially designed driving fields.

Chapter 3

Quantum susceptibilities in time-domain sampling of electric field fluctuations

All results in this chapter have been published in Ref. [94]. All of the calculations have been performed by myself. The text, structure and notation has been edited slightly in order to keep the consistency with the other chapters.

3.1 Introduction

Nonlinear optics with laser light serves as one of the fundamental tools in modern experimental physics. In three-wave mixing spectroscopy, for example, materials are examined by irradiating them with optical fields and measuring the light emitted into a new direction. The spectral and temporal shape as well as the amplitude and phase of the incoming fields can be varied to study different effects. These options lead to a wide range of classical techniques such as, e.g., coherent anti-Stokes Raman [95], photon echo [96] and two-dimensional femtosecond spectroscopy [97]. Exploiting strong coherent states of laser light justifies a classical treatment of the electric fields. The corresponding processes inside a material are then described by a classical response in terms of causal nonlinear susceptibilities [13, 30, 98]. Such a scenario involving quantum matter and classical fields underlies the area of classical nonlinear optics. In contrast to classical fields, quantum fields exhibit a larger number of degrees of freedom. This fact allows to exploit phenomena such as quantum superposition [99] and entanglement [100, 101] in order to enhance classical spectroscopic tools [26].

Usually, the nonlinear susceptibilities are calculated separately from the electric

fields involved and then inserted into an effective Hamiltonian describing the nonlinear interaction [30, 98]. This description requires that all light fields remain in a classical limit and correlations between them may be neglected. Theories relying on effective Hamiltonians can also accurately describe the interaction between quantum fields and nonlinear matter in an off-resonant regime. Nonlinear processes such as four-wave mixing [25] or parametric downconversion [22–24] far from resonance are typically exploited to generate nonclassical states of light. In the vicinity of resonant transitions, the classical susceptibilities alone fail to accurately describe the response of nonlinear matter to quantum fields. Here, the physics is most adequately described by quantum susceptibilities that are influenced by higher-order fluctuations of the nonlinear medium [27–29].

In its standard application, electro-optic sampling represents a typical example for classical nonlinear optics. In chapter 1.5, we have seen how this technique can be extended in order to sample the fluctuations of quantum THz fields. Theoretical models have so far relied on a macroscopic description of the second-order nonlinear interaction inside the crystal based on a classical susceptibility $\chi^{(2)}$ [7, 50]. Here, the sampling of a classical THz field is straightforwardly extended to the quantum regime. We investigate the limitations of this approach and demonstrate when quantum effects of the nonlinear response must be taken into account.

To this end, a time-domain quantum electrodynamic theory of electro-optic sampling is developed. A system of three-level noninteracting molecules is employed to model the nonlinear medium and to calculate its frequency response in amplitude and phase. We demonstrate how fluctuations of the phase-dependent quadratures of the generated electro-optic signal can be measured and that a full quantum tomography of the generated signal is feasible. Our theory focuses on the nature of the nonlinear electro-optic response and pinpoints under which conditions a straightforward reconstruction of the quantum fluctuations is possible. Two types of quantum corrections are identified: quantum susceptibilities and cascading processes which lead to an effective intermolecular interaction mediated by THz fluctuations. Previous theories [7, 50] did not include these effects. We show that the ultrashort temporal duration of the probe pulse leads to time-ordering for the cascading processes that squeeze the generated near-infrared field for certain phase shifts. Conditions under which electro-optic sampling might be employed as a spectroscopic tool to study quantum susceptibilities are explored. Finally, we describe how the probability distribution of the THz fluctuations can be reconstructed from the measured probability distribution of the electro-optic signal and find that quantum corrections can affect this reconstruction.

3.2 The setup

The geometry of the setup is shown in Fig. 1.2(a) and the level scheme exploited to describe the nonlinear medium is sketched in Figs. 3.1, where we assume an effective three-level electro-optic medium (EOM) that exhibits a second-order nonlinear susceptibility tensor with a zincblende-type symmetry. The EOM is modeled by a large number of independent quantum systems which we term *molecules*. An intense near-infrared (NIR) probe field in a strong multimode coherent state $|\{E_{\mathrm{p},z}\}\rangle$ with a large amplitude $E_{\mathrm{p},z}(\omega) = \left\langle \{E_{\mathrm{p},z}\} \left| \hat{E}_{\mathrm{p},z}(\omega) \right| \{E_{\mathrm{p},z}\} \right\rangle$ and a terahertz (THz) field $\hat{E}_{\mathrm{THz},s}(\Omega)$ are sent into the EOM. These beams are linearly polarized along the $\mathbf{e}_z$ and $\mathbf{e}_s$ directions, respectively. While propagating through the nonlinear medium, the two fields undergo sum- (SFG) and difference-frequency generation (DFG). Both three-wave mixing processes generate an $\mathbf{e}_{\mathrm{s}}$-polarized weak contribution to $\hat{E}_{\mathrm{p},s}$. A waveplate then shifts the two polarization components of the NIR field after the EOM by the angle θ with respect to each other, effectively mixing the two contributions.

We consider a tunable waveplate that can introduce arbitrary phase shifts θ. If the fast axis of the waveplate is rotated by an angle α against $\mathbf{e}_z$, the total NIR electric

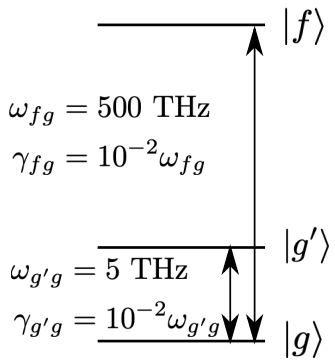

Figure 3.1: Model for the molecules representing the EOM, comprising three levels $i, j = g, g', f$ with transition frequencies ω_{ij} and lifetime broadenings γ_{ij}.

field after it can be expressed as [102]

$$\begin{pmatrix} \hat{E}'_{\mathrm{p},s} \\ \hat{E}'_{\mathrm{p},z} \end{pmatrix} = \begin{pmatrix} \cos\alpha & \sin\alpha \\ -\sin\alpha & \cos\alpha \end{pmatrix} \begin{pmatrix} e^{-i\theta/2} & 0 \\ 0 & e^{i\theta/2} \end{pmatrix} \begin{pmatrix} \cos\alpha & -\sin\alpha \\ \sin\alpha & \cos\alpha \end{pmatrix} \begin{pmatrix} \hat{E}_{\mathrm{p},s} \\ \hat{E}_{\mathrm{p},z} \end{pmatrix}, \tag{3.1}$$

where $\hat{E}_{\mathrm{p},s}, \hat{E}_{\mathrm{p},z}$ are the polarization components of the probe field arriving at the waveplate whereas $\hat{E}'_{\mathrm{p},s}, \hat{E}'_{\mathrm{p},z}$ represent these components at its output.

After the waveplate, the light is sent through a Wollaston prism which separates the two polarization directions. Finally, the number of photons in these beams, $\hat{N}'_s$ and $\hat{N}'_z$, are measured with the detectors D_s and D_z, respectively. The electro-optic signal is given by their difference

$$\begin{aligned} \hat{\mathcal{S}}(\theta) \equiv \hat{N}'_z - \hat{N}'_s &= C \int_0^\infty \mathrm{d}\omega \frac{1}{\hbar\omega} \left(\hat{E}'^{\dagger}_{\mathrm{p},z}(\omega) \hat{E}'_{\mathrm{p},z}(\omega) - \hat{E}'^{\dagger}_{\mathrm{p},s}(\omega) \hat{E}'_{\mathrm{p},s}(\omega) \right) \\ &= C \int_0^\infty \mathrm{d}\omega \frac{1}{\hbar\omega} \left[\left(\sin^2\frac{\theta}{2} \sin 4\alpha + i \sin\theta \sin 2\alpha \right) \hat{E}^\dagger_{\mathrm{p},z}(\omega) \hat{E}_{\mathrm{p},s}(\omega) + H.c. \right] \\ &\quad + \left(\cos^2\frac{\theta}{2} + \sin^2\frac{\theta}{2} \cos 4\alpha \right) \left(\hat{N}_z - \hat{N}_s \right), \end{aligned} \tag{3.2}$$

where the operator $\hat{N}_z - \hat{N}_s$ denotes the difference in photon numbers before the waveplate, $C = 4\pi\varepsilon_0 A c_0$ with A being the effective transverse area determined by the beam waist of the probe field, c_0 the speed of light in vacuum, and ε_0 the vacuum permittivity. For a balanced detection, the second term on the right hand side of Eq. (3.2) must vanish. This can be achieved by adjusting the angle of the fast axis α for each phase shift θ so that

$$\cos^2\frac{\theta}{2} + \sin^2\frac{\theta}{2} \cos 4\alpha = 0.$$

This condition is satisfied by $\alpha = \arccos\left(-\cot^2\frac{\theta}{2}\right)/4$ for $\pi/2 \leq \theta \leq 3\pi/2$. In this case, the balanced electro-optic signal is given by

$$\hat{\mathcal{S}}(\theta) = \hat{N}'_z - \hat{N}'_s = C \int_0^\infty \mathrm{d}\omega \, \frac{1}{\hbar\omega} \left[P(\theta) \hat{E}^\dagger_{\mathrm{p},z}(\omega) \hat{E}_{\mathrm{p},s}(\omega) + H.c. \right], \tag{3.3}$$

with $P(\theta) = \sqrt{-\cos(\theta)} + i\sqrt{2}\cos(\theta/2)$. A phase shift of $\theta = \pi/2$ or $\theta = \pi$ is induced by a quarter- or half-wave plate, respectively [102] [see Fig. 1.2(a)].

The mean value of the electro-optic signal $\hat{\mathcal{S}}(\theta)$ is proportional to that of the sampled THz field [40]. The temporal profile of an electrical transient can therefore be sampled by measuring the mean value of $\hat{\mathcal{S}}(\theta)$ for different delay times between the

probe and the THz field. To achieve subcycle temporal resolution, the NIR probe field must be shorter than the characteristic period of the input field. To gain insight into the quantum character of light, higher moments of the electric field are of interest. To access them experimentally, the statistics of $\hat{\mathcal{S}}(\theta)$ needs to be collected. The relative likelyhood of each measurement result $\mathcal{S}$ builds up a histogram representing the probability distribution $P(\mathcal{S},\theta)$ equivalently to standard balanced homodyne tomography. As explained, the electro-optic signal is obtained by measuring the difference between the detected numbers of the $\mathbf{e}_z$-polarized and $\mathbf{e}_s$-polarized photons. In order to calculate $P(\mathcal{S},\theta)$, we therefore start with the joint probability to measure n_z $\mathbf{e}_z$-polarized photons and n_s $\mathbf{e}_s$-polarized photons [48],

$$\begin{aligned} P(n_z,n_s) &= \left\langle : \frac{\hat{N}_z'^{n_z}}{n_z!} e^{-\hat{N}_z'} \frac{\hat{N}_s'^{n_s}}{n_s!} e^{-\hat{N}_s'} : \right\rangle \\ &\approx \left\langle : \frac{1}{\sqrt{2\pi\hat{N}_z'}} e^{-\frac{(n_z-\hat{N}_z')^2}{2\hat{N}_z'}} \frac{1}{\sqrt{2\pi\hat{N}_s'}} e^{-\frac{(n_s-\hat{N}_s')^2}{2\hat{N}_s'}} : \right\rangle, \end{aligned} \tag{3.4}$$

where we assumed a lossless detector and approximated the Poissonian function as a Gaussian in the second line because of the strong coherent probe resulting in large expected photon numbers for both polarization directions. We are interested in the probability to measure $\mathcal{S} = n_z - n_s$, which can be derived according to

$$\begin{aligned} P(\mathcal{S}) &= \sum_{n_z} P(n_z, n_z - \mathcal{S}) \\ &= \int \mathrm{d}x P(x, x-\mathcal{S}) \\ &= \left\langle : \frac{1}{\sqrt{2\pi\hat{N}_\mathrm{T}'}} e^{-\frac{(\mathcal{S}-\hat{\mathcal{S}}(\theta))^2}{2\hat{N}_\mathrm{T}'}} : \right\rangle, \end{aligned}$$

with $\hat{N}_\mathrm{T}' = \hat{N}_z' + \hat{N}_s'$ as the total detected photon number. Here, we replaced the discrete sum by an integral because of the large expected total photon number and then used the fact that a convolution of two Gaussians also results in a Gaussian distribution. The total detected photon number may then be well approximated by the mean number of photons in the probe N, resulting in

$$\begin{aligned} P(\mathcal{S},\theta) &= \left\langle : \frac{1}{\sqrt{2\pi N}} e^{-\frac{(\mathcal{S}-\hat{\mathcal{S}}(\theta))^2}{2N}} : \right\rangle, \\ &= \frac{1}{\sqrt{2\pi N}} \sum_{k=0}^{\infty} \frac{1}{(2N)^{k/2} k!} H_k(\mathcal{S}/\sqrt{2N}) \exp\left(-\frac{\mathcal{S}^2}{2N}\right) \langle : \hat{\mathcal{S}}^k(\theta) : \rangle, \end{aligned} \tag{3.5}$$

where $N = C\int_0^\infty \mathrm{d}\omega\,|E_{\mathrm{p},z}(\omega)|^2/\hbar\omega$ is the mean number of photons of the probe, $H_k(x)$ is the kth-order Hermite polynomial and the colons denote normal ordering.

3.3 Superoperator representation of classical and quantum nonlinear susceptibilities

In this work, we want to ignore corrections to the probability distribution related to the mean value of the signal $\langle{:}\hat{\mathcal{S}}(\theta){:}\rangle$ since they only provide information about the classical characteristics of the THz input. We thus focus on the normally-ordered second moment of the signal, $\Gamma = \langle{:}\hat{\mathcal{S}}^2(\theta){:}\rangle$. The variance of $\hat{\mathcal{S}}(\theta)$ is given by $\langle\hat{\mathcal{S}}^2(\theta)\rangle = N + \Gamma$, where N is the shot noise of the probe. Instead, the influence of the fluctuations of these THz fields on Γ is studied. Moreover, we consider the sampling of THz vacuum fluctuations since they represent a natural resource in the experiment and the physics remains maximally transparent. An expression for Γ that describes the sampling of arbitrary quantum fields is derived in Appendix B. We employ the superoperator formalism [13] which offers a compact quantum treatment of both the matter system and the electric fields to derive a microscopic expression for Γ. The evolution of the system is determined by the dipole light-matter interaction Hamiltonian $H_{\mathrm{int}}(t) = -\sum_{\alpha=z,s}\sum_i\ \hat{\mathcal{E}}_\alpha(\mathbf{r}_i,t)\hat{\mathcal{V}}_{\alpha,i}(t)$ where $\mathbf{r}_i$ denotes the location of the molecules. The corresponding superoperator $\hat{H}_{\mathrm{int},-}(t)$ is given by [27]

$$\hat{H}_{\mathrm{int},-}(t) = -\sum_{\alpha=z,s}\sum_i\ \left[\hat{\mathcal{E}}_{\alpha,+}(\mathbf{r}_i,t)\hat{\mathcal{V}}_{\alpha,i,-}(t) + \hat{\mathcal{E}}_{\alpha,-}(\mathbf{r}_i,t)\hat{\mathcal{V}}_{\alpha,i,+}(t)\right], \tag{3.6}$$

where we have used the fact that the dipole and the electric field operators commute. Here, $\alpha = z,s$ represents the two possible mutually perpendicular polarizations, $\hat{\mathcal{E}}_\alpha(\mathbf{r},t) = \hat{E}_{\mathrm{p},\alpha}(\mathbf{r},t) + \hat{E}_{\mathrm{THz},\alpha}(\mathbf{r},t) + H.c.$ is the sum of all relevant field modes and $\hat{\mathcal{V}}_{\alpha,i}(t) = \hat{V}_{\alpha,i}(t) + \hat{V}^\dagger_{\alpha,i}(t)$ denotes the dipole operator of the ith molecule in the interaction picture with $\hat{V}_{\alpha,i} = \mu_{\alpha,\mathrm{gg}'}\,|g\rangle_{ii}\langle g'| + \mu_{\alpha,\mathrm{gf}}\,|g\rangle_{ii}\langle f| + \mu_{\alpha,\mathrm{g'f}}\,|g'\rangle_{ii}\langle f|$ and $\mu_{\alpha,mn}$ as the dipole moment for the $n \to m$ transition $(m,n = g,g',f)$.

The normally-ordered second moment of the electro-optic signal Γ is calculated from the time-dependent density matrix of the entire system of field and matter $\hat{\rho}$,

$$\Gamma \equiv \langle{:}\hat{\mathcal{S}}^2(\theta){:}\rangle = \mathrm{tr}\left\{{:}\hat{\mathcal{S}}^2(\theta){:}\,\mathcal{T}\exp\left(-\frac{i}{\hbar}\int_{-\infty}^{\infty}\mathrm{d}t\hat{H}_{\mathrm{int},-}(t)\right)\hat{\rho}_{\mathrm{in}}\right\}. \tag{3.7}$$

Here, $\hat{\rho}_{\mathrm{in}} = \hat{\rho}_{\mathrm{field}} \otimes \hat{\rho}_{\mathrm{mat}}$ denotes the initial density matrix given by a direct product of the density matrices for field and matter and $\mathcal{T}$ represents the time-ordering operator for the superoperators. We assume $\hat{\rho}_{\mathrm{field}} = |\{E_{\mathrm{p},z}\}\rangle\langle\{E_{\mathrm{p},z}\}| \otimes |0_{\mathrm{s}}\rangle\langle 0_{\mathrm{s}}|$, i.e. the electric

field consists of a multimode coherent state in the $\mathbf{e}_z$-polarized NIR range and the electromagnetic vacuum in both the $\mathbf{e}_s$-polarized NIR and THz ranges. The matter system consists of an ensemble of noninteracting molecules initially in the ground state. Since the trace operation is invariant under cyclic permutation, we can let the time evolution according to the interaction Hamiltonian in Eq. (3.6) act on $:\hat{\mathcal{S}}^2(\theta):$. The trace can then be factorized into a product of traces over the field and the matter degrees of freedom. The matter trace is given by a time-ordered product of n Green's functions of superoperators for the $(n+1)$th-order perturbation term in $\hat{H}_{\mathrm{int},-}(t)$, resulting in the nth-order susceptibility [see chapter 1.4].

3.4 Normally-ordered second moment of the THz vacuum field

In this section, we calculate the normally-ordered second moment Γ. Since both the NIR $\hat{E}_{\mathrm{p},s}$ and the THz $\hat{E}_{\mathrm{THz},s}$ field modes are initially in the vacuum state, each of them must interact at least twice to give a non-vanishing contribution to Eq. (3.7). Therefore, we need to have two interactions with $\hat{E}_{\mathrm{p},z}$, $\hat{E}_{\mathrm{p},s}$ and $\hat{E}_{\mathrm{THz},s}$, each. It is now mandatory to expand the exponential in Eq. (3.7) to sixth order in $\hat{H}_{\mathrm{int},-}$. Linear contributions may be neglected. Due to the large number of molecules, the dominant contribution to the signal comes from pairs of molecules each interacting three times with the dipole operator. We are thus considering two second-order processes instead of a single fifth-order process. The probe will be treated classical because of its strong coherent amplitude, i.e. we only take into account interactions of the form $\hat{E}_{\mathrm{p},z,+}$ since $\hat{E}_{\mathrm{p},z,-}$ vanishes for a classical field. This approximation does not apply to the quantum fields $\hat{E}_{\mathrm{p},s}$ and $\hat{E}_{\mathrm{THz},s}$. The leading diagrams for Γ that survive the rotating wave approximation (RWA) are given in Fig. 3.2. Note that the RWA has not been applied in our calculations which are based on Eq. (3.6) and include the full set of diagrams given in Appendix B. In Fig. 3.2(I), the pair of molecules that generate the signal interact with the THz vacuum through $\hat{E}_{\mathrm{THz},s,+}$. In this case, the time ordering of these two interactions is immaterial and the nonlinear processes are completely independent of each other. In contrast, the remaining diagrams describe shared fluctuations between two molecules that involve the commutator of two THz field modes. The first interaction with $\hat{E}_{\mathrm{THz},s,-}$ on molecule b, e.g., emits a THz photon which is then absorbed by molecule a through the interaction with $\hat{E}_{\mathrm{THz},s,+}$. Therefore, the intermolecular time ordering of these interactions with the THz field is crucial. It leads to an effective interaction between molecules a and b that is mediated by the THz vacuum fluctuations. These processes can only be understood in the joint

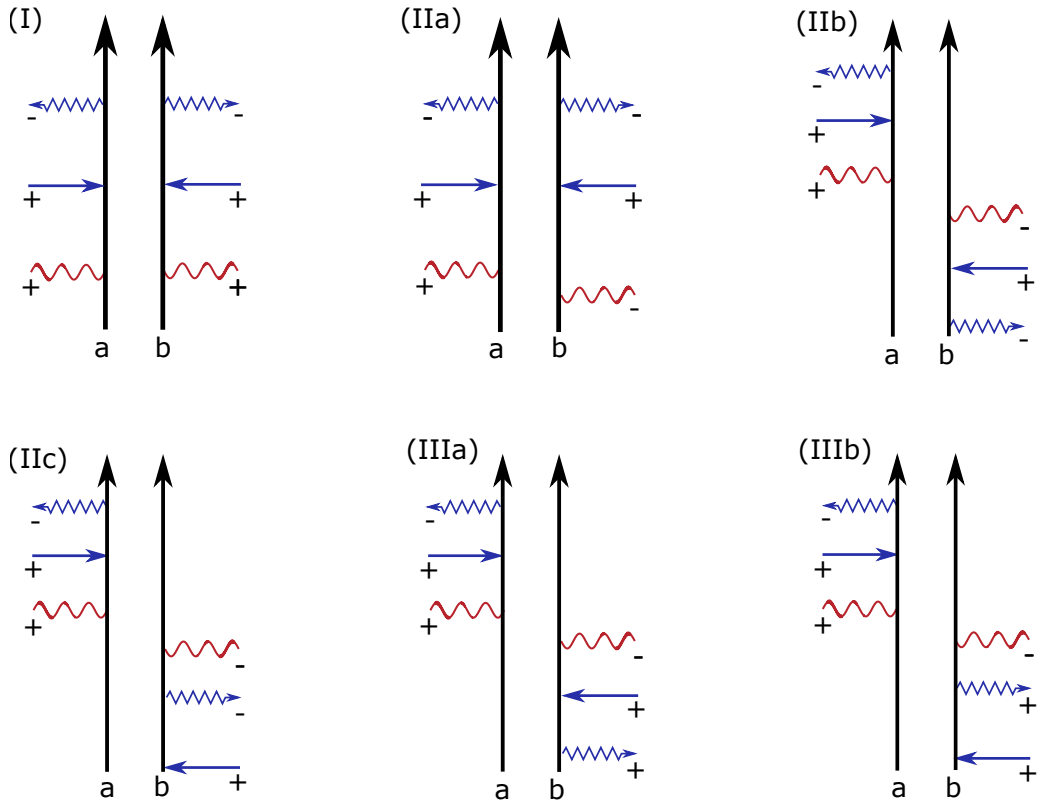

Figure 3.2: Diagrams representing the leading contributions to electro-optic sampling of THz vacuum fluctuations [Eq. (3.8)] for two molecules a and b. Each diagram depicts interactions between the electric field modes and the density matrix of the matter system. The vertical arrows indicate the time evolution of molecules a and b from the past (bottom) to the present (top), respectively. The red wavy lines denote an interaction with either $\hat{E}_{\mathrm{THz},s}$ or $\hat{E}^{\dagger}_{\mathrm{THz},s}$, the blue zigzag arrows pointing to the left (right) represent interactions with $\hat{E}^{\dagger}_{\mathrm{p},s}$ ($\hat{E}_{\mathrm{p},s}$) and the straight blue arrows pointing to the left (right) denote interactions with the coherent probe field $E^{*}_{\mathrm{p},z}$ ($E_{\mathrm{p},z}$), respectively. The $\pm$ signs next to the horizontal arrows denote the type of superoperator interaction for the corresponding field mode. (I) A process that can be described by classical susceptibilities. This diagram is the only one captured by the classical treatment. (IIa)$-$(IIc) Processes that involve quantum susceptibilities due to two $'-'$-type interactions of molecule b with $\hat{E}_{\mathrm{p},s}$ and $\hat{E}_{\mathrm{THz},s}$. (IIIa) and (IIIb) Cascading processes that can be described by classical susceptibilities but are not captured by the classical treatment described in the main text. The diagrams depicted here survive the rotating wave approximation (RWA). For a detailed calculation and the full set of diagrams see Appendix B.

space of both molecules. We note that initially and in the final state, all molecules are uncoupled. The coupling exists during the interaction process initiated by the probe field, where an excited molecule can transfer its excitation to another molecule

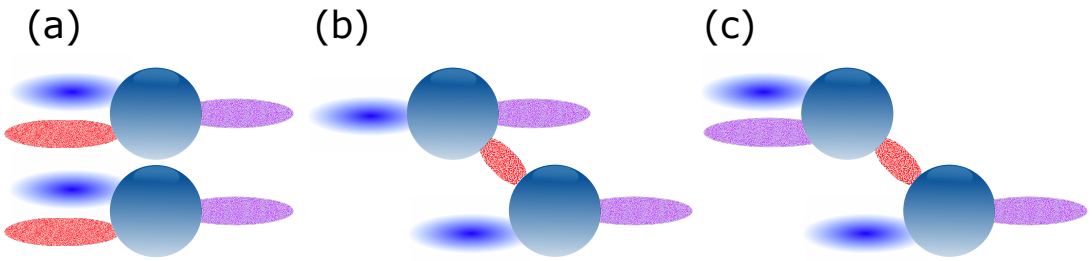

Figure 3.3: Visualization of the three different types of responses. (a) The probe $E_{\mathrm{p},z}$ (blue) and the THz vacuum $\hat{E}_{\mathrm{THz},s}$ (red) interact with two molecules (spheres) to generate the NIR field $\hat{E}_{\mathrm{p},s}$ (violet). The two processes happen independently of each other and belong to the classical response Γ_I in Eq. (3.9). (b) The probe interacts with one molecule to generate both a THz and a NIR field. The generated THz field together with the probe then interacts with a second molecule to generate an additional NIR field. The first $\chi^{(2)}$ process is described by quantum susceptibilities and the response is given by Eq. (3.11). (c) The probe and the NIR vacuum interact with one molecule to generate a THz field. The generated THz component together with the probe then interacts with a second molecule to generate a NIR field. These are cascading processes which are described by Eq. (3.13).

via the THz vacuum. No classical field is generated at any point during this process. We split the normally-ordered second moment Γ of the electro-optic signal into three contributions

$$\Gamma = \Gamma_{\mathrm{I}} + \Gamma_{\mathrm{II}} + \Gamma_{\mathrm{III}}, \tag{3.8}$$

which will be discussed in detail below.

The first contribution Γ_{I} is given by

$$\Gamma_{\mathrm{I}} = \left(\frac{N\omega_{\mathrm{p}} L\rho_0}{c_0}\right)^2 \int_0^\infty d\Omega \frac{\hbar\Omega}{C}\left[1 + \mathrm{sinc}^2\left(2\Omega L/c_0\right)\right] |D(\Omega,\theta)|^2 , \tag{3.9}$$

where $\omega_{\mathrm{p}} = \int_0^\infty \mathrm{d}\omega\, |E_{\mathrm{p},z}(\omega)|^2 \,/\, \int_0^\infty \mathrm{d}\omega\, (1/\omega)\, |E_{\mathrm{p},z}(\omega)|^2$ is the average detected frequency, L is the length of the nonlinear medium along the propagation direction, and ρ_0 is the density of the molecules. In the following, ω and Ω denote frequencies in the NIR and THz range, respectively. We have further introduced the gating function $D(\Omega,\theta)$ which

depends on the classical susceptibilities $\chi^{(2)}_{+--}$

$$D(\Omega,\theta) = \frac{1}{2}\int_0^\infty \mathrm{d}\omega f_+^*(\omega,\Omega,\theta)\left(\chi^{(2)*}_{+--}(-\omega;-\Omega,\omega+\Omega)+\chi^{(2)*}_{+--}(-\omega;\omega+\Omega,-\Omega)\right) - \frac{1}{2}\int_0^\infty \mathrm{d}\omega f_-(\omega,\Omega,\theta)\left(\chi^{(2)}_{+--}(-\omega;\Omega,\omega-\Omega)+\chi^{(2)}_{+--}(-\omega;\omega-\Omega,\Omega)\right), \tag{3.10}$$

with the autocorrelation functions $f_\pm(\omega,\Omega,\theta) = P(\theta)E^*_{\mathrm{p},z}(\omega)E_{\mathrm{p},z}(\omega\pm\Omega)/\int_0^\infty \mathrm{d}\omega\,|E_{\mathrm{p},z}(\omega)|^2$. The leading diagram to this contribution is depicted in Fig. 3.2(I). Here, both molecules interact independently with the THz vacuum and the matter response can be described in the single-molecule space. In that sense, the THz vacuum may be treated as a classical field in analogy to the response of conventional electro-optic sampling which is why the matter response is given by classical susceptibilities $\chi^{(2)}_{+--}$ [cf. Eq. (1.79)]. Figure 3.3(a) provides a visual representation of these processes. The same result may be also obtained by calculating the third-order correction to the electro-optic signal $\hat{\mathcal{S}}(\theta)$ in Eq. (3.3) and squaring it [see the result for arbitrary THz fields in Eq. (B.1) of Appendix B]. Γ_I represents the classical contribution to the normally-ordered second moment Γ and always remains positive. These are the only processes that depend on the state of the THz field and are actually sampling its fluctuations [cf. Eq. (B.1) in Appendix B]. We thus have a quantum extension of classical electro-optic sampling which not only provides access to the temporally resolved mean value of the THz input but also its fluctuations.

The other two contributions Γ_II and Γ_III in Eq. (3.8) constitute genuine quantum corrections. Here, the first interaction of the matter system with the THz field is given by the superoperator $\hat{E}_{\mathrm{THz},s,-}$, generating a THz field which propagates further and interacts with a second molecule according to $\hat{E}_{\mathrm{THz},s,+}$. This process leads to an intermolecular time ordering of the two $\chi^{(2)}$ processes and an effective intermolecular interaction which is only understandable in the two-molecule space. The intermolecular time ordering is reflected in interference terms that may also reduce the fluctuations of the electro-optic signal. Contributions of this type involve the commutator of the THz field operators and are independent of their state. They therefore represent byproducts of the nonlinear interaction that do not provide any information on the THz input.

Γ_{II} is given by

$$\Gamma_{\mathrm{II}} = \left(\frac{N\omega_{\mathsf{p}}L\rho_0}{c_0}\right)^2 \int_0^\infty d\Omega \frac{\hbar\Omega}{C}\left[1+\mathrm{sinc}^2\left(2\Omega L/c_0\right)\right]\Re\left\{D(\Omega,\theta)D_{\mathrm{q}}(\Omega,\theta)\right\} - \left(\frac{N\omega_{\mathsf{p}}L\rho_0}{c_0}\right)^2 \int_0^\infty d\Omega \frac{\hbar c_0}{CL}\left[3+\mathrm{sinc}^2\left(2\Omega L/c_0\right)\right]\Im\left\{D(\Omega,\theta)D_{\mathrm{q}}(\Omega,\theta)\right\}, \tag{3.11}$$

where $\Re\{\cdot\}$ and $\Im\{\cdot\}$ denote the real and imaginary part, respectively. Here, the classical gating function $D(\Omega,\theta)$ is given in Eq. (3.10) and the gating function $D_{\mathrm{q}}(\Omega,\theta)$, which depends on quantum susceptibilities, is given by

$$\begin{aligned} D_{\mathrm{q}}(\Omega,\theta) = &\int_0^\infty \mathrm{d}\omega f_+(\omega,\Omega,\theta)\left(\chi^{(2)}_{++-}(-\Omega;-\omega,\omega+\Omega)+\chi^{(2)}_{+-+}(-\Omega;\omega+\Omega,-\omega)\right) \\ &+\int_0^\infty \mathrm{d}\omega f_+(\omega,\Omega,\theta)\left(\chi^{(2)}_{++-}(-\omega;-\Omega,\omega+\Omega)+\chi^{(2)}_{+-+}(-\omega;\omega+\Omega,-\Omega)\right) \\ &+\int_0^\infty \mathrm{d}\omega f_-^*(\omega,\Omega,\theta)\left(\chi^{(2)*}_{++-}(\Omega;-\omega,\omega-\Omega)+\chi^{(2)*}_{+-+}(\Omega;\omega-\Omega,-\omega)\right) \\ &+\int_0^\infty \mathrm{d}\omega f_-^*(\omega,\Omega,\theta)\left(\chi^{(2)*}_{++-}(-\omega;\Omega,\omega-\Omega)+\chi^{(2)*}_{+-+}(-\omega;\omega-\Omega,\Omega)\right). \end{aligned} \tag{3.12}$$

D_{q} involves quantum susceptibilities of the form $\chi^{(2)}_{++-}$ and $\chi^{(2)}_{+-+}$ [cf. Eq. (1.79)]. Figure 3.3(b) demonstrates these types of processes. The leading diagrams are depicted in Figs. 3.2(IIa)-(IIc). Observing features related to these susceptibilities therefore assures that a genuinely nonclassical field was involved in the responsible nonlinear process.

Finally, Γ_{III} is given by

$$\Gamma_{\mathrm{III}} = \left(\frac{N\omega_{\mathsf{p}}L\rho_0}{c_0}\right)^2 \int_0^\infty d\Omega \frac{\hbar\Omega}{C}\left[1+\mathrm{sinc}^2\left(2\Omega L/c_0\right)\right]\Re\left\{D(\Omega,\theta)D_{\mathrm{casc}}(\Omega,\theta)\right\} - \left(\frac{N\omega_{\mathsf{p}}L\rho_0}{c_0}\right)^2 \int_0^\infty d\Omega \frac{\hbar c_0}{CL}\left[3+\mathrm{sinc}^2\left(2\Omega L/c_0\right)\right]\Im\left\{D(\Omega,\theta)D_{\mathrm{casc}}(\Omega,\theta)\right\}, \tag{3.13}$$

where the gating function $D_{\mathrm{casc}}(\Omega,\theta)$ which depends on the classical susceptibilities

$\chi^{(2)}_{+--}$ is given by

$$D_{\mathrm{casc}}(\Omega,\theta) = \frac{1}{2}\int_0^\infty \mathrm{d}\omega f_+(\omega,\Omega,\theta)\left(\chi^{(2)}_{+--}(-\Omega;-\omega,\omega+\Omega)+\chi^{(2)}_{+--}(-\Omega;\omega+\Omega,-\omega)\right) + \frac{1}{2}\int_0^\infty \mathrm{d}\omega f_-^*(\omega,\Omega,\theta)\left(\chi^{(2)*}_{+--}(\Omega;-\omega,\omega-\Omega)+\chi^{(2)*}_{+--}(\Omega;\omega-\Omega,-\omega)\right). \tag{3.14}$$

Γ_{III} constitutes a quantum correction even though the gating function $D_{\mathrm{casc}}(\Omega,\theta)$ only involves classical susceptibilities of the type $\chi^{(2)}_{+--}$. Here, we deal with cascading processes where for example a photon is emitted into the THz vacuum by molecule b and then reabsorbed at molecule a. Figure 3.3(c) gives a visual representation of this kind of processes. The leading diagrams are shown in Fig. 3.2(IIIa) and (IIIb). The cascading processes can also be obtained within an effective Hamiltonian since they only involve classical susceptibilities. Eq. (3.13) contains two terms. In the first, energy conservation holds for each single $\chi^{(2)}$ process whereas in the second, energy is conserved only for both $\chi^{(2)}$ processes combined.

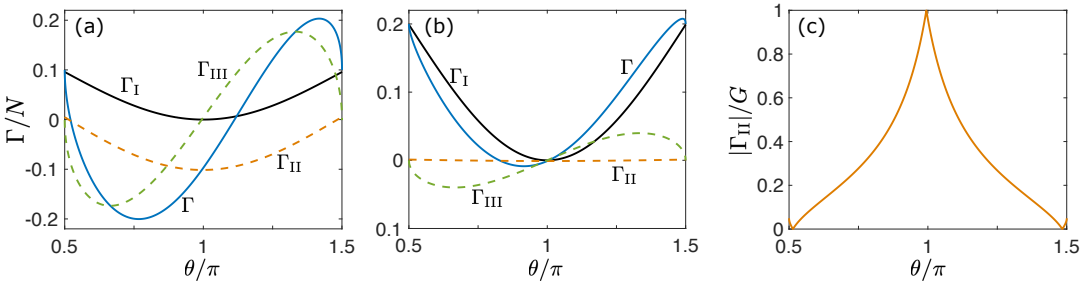

Figure 3.4: Normally-ordered second moment Γ of the electro-optic signal calculated according to Eqs. (3.9), (3.11) and (3.13) for different phase shifts θ. (a) Γ according to the level scheme shown in Fig. 3.1. The blue line depicts Γ for the full quantum treatment given by Eq. (3.8). It is given by the sum of the classical contribution Γ_{I} [black line, cf. Eq. (3.9)], the contribution stemming from the quantum susceptibilities Γ_{II} [dashed orange line, cf. Eqs. (3.11)] and the cascading contribution Γ_{III} [dashed green line, cf. Eqs. (3.13)]. (b) Off-resonant case with $\omega,\Omega \ll \omega'_{g'g},\omega'_{fg}$. The length L of the nonlinear medium with respect to the strength of the nonlinear susceptibilities is chosen such that the maximal value of Γ can still be regarded as a small correction to the shot noise. In this case, a maximum contribution of $0.2N$ was adopted. (c) Ratio of the absolute strength of the quantum contribution $|\Gamma_{\mathrm{II}}|$ to the combined absolute strengths of each contribution $G = |\Gamma_{\mathrm{I}}| + |\Gamma_{\mathrm{II}}| + |\Gamma_{\mathrm{III}}|$ for the level scheme shown in Fig. 3.1. The normally-ordered second moment Γ is almost entirely determined by the quantum contribution Γ_{II} for the half-wave plate configuration, given by $\theta = \pi$.

3.5 Simulation results for the three-level model

To illustrate the difference between the classical and quantum response of matter, we have calculated them for the three-level scheme shown in Fig. 3.1 and a length L of 10 μm for the nonlinear medium. We assume a rectangular spectral envelope of the probe field with a center frequency of $\omega_c/(2\pi) = 255$ THz and a spectral width of $\Delta\omega/(2\pi) = 150$ THz. Therefore, the probe is off-resonant with respect to both transition frequencies while the THz vacuum can include frequencies resonant with the $g \to g'$ transition. Figure 3.4(a) depicts the normally ordered second moment Γ in Eq. (3.8) together with its three components: the classical response Γ_{I}, the response described by the quantum susceptibilities Γ_{II} and the response according to the cascading processes Γ_{III}. Γ_{I} samples the THz vacuum fluctuations which are uncorrelated with the shot noise of the probe. Therefore, it can only enhance the fluctuations of the electro-optic signal. In contrast, both quantum corrections can also lead to a reduction of the noise due to the effective interaction between the molecules mediated by the THz vacuum. Interestingly, there are certain phase shifts θ where one of the three contributions is dominant. Figures 3.4(a) and (c) demonstrate that for a quarter-wave plate ($\theta = \pi/2$) the quantum contributions are small compared to the classical response while for a half-wave plate ($\theta = \pi$), the quantum contribution Γ_{II} constitutes almost the entire electro-optic signal. Outcomes for intermediate phase shifts are dominated by the cascading contribution Γ_{III}. The fact that both the classical and the cascading contributions almost vanish in the half-wave plate configuration ($\theta = \pi$) is remarkable and suggests that electro-optic sampling could also be used as a spectroscopic tool to study the pure quantum susceptibilities of different materials.

As demonstrated in Fig. 3.4(b), the quantum susceptibilities involved in the gating function D_{q} almost vanish in the off-resonant case. However, the cascading processes [103] described by the gating function D_{casc} still constitute a significant contribution even if all fields involved are off resonance with respect to the transition frequencies of the material. Figure 3.4(b) shows the off-resonant normally-ordered second moment Γ in Eq. (3.8) where we have now assumed a three-level model with transition frequencies $\omega, \Omega \ll \omega'_{g'g}, \omega'_{fg}$. The cascading processes can lead to substantial corrections for intermediate phase shifts of $\pi/2 < \theta < \pi$ and $\pi < \theta < 3\pi/2$. These corrections are given by the second term in Eq. (3.13). They are thus originating from processes where an energy excess or deficiency is created in the first $\chi^{(2)}$ process only to be compensated by the second $\chi^{(2)}$ process. This exchange of energy between the two nonlinear steps can only happen within a certain distance determined by the frequency of the generated THz field. This fact also explains why the second term in Eq. (3.13) scales just linearly with the length of crystal. The presence of this effect is therefore owed to the short

length of the crystal and the broadband nature of the sampling.

In previous experiments [6, 9], electro-optic sampling was carried out with a phase shift of $\theta = \pi/2$. Interestingly, Fig. 3.4(b) shows that while the cascading processes result in distinct contributions for various phase shifts, they can be neglected and thus remain hidden in this configuration so that the classical treatment provides a good approximation. However, their presence can be inferred, e.g., if spectral filtering is introduced into the measurement according to Fig. 3.5(a) where only half of the probe spectrum is exploited for detection. The corresponding electro-optic signal is given by

$$\hat{\mathcal{S}}_{\mathrm{cut}}(\tilde{\omega}) = C \int_{\tilde{\omega}-\Delta\omega/4}^{\tilde{\omega}+\Delta\omega/4} \mathrm{d}\omega \, \frac{1}{\hbar\omega} \left[i\hat{E}_{\mathrm{p},z}^{\dagger}(\omega)\hat{E}_{\mathrm{p},s}(\omega) + H.c. \right], \tag{3.15}$$

where the frequency window is centered at $\tilde{\omega}$. Figure 3.5(a) depicts the spectral cut for $\tilde{\omega} = \omega_c - \Delta\omega/4$, which generally begins in the lower half of the probe spectrum at $\tilde{\omega} - \Delta\omega/4$ and ends in the upper half at $\tilde{\omega} + \Delta\omega/4$. Figure 3.5(b) illustrates how the normally-ordered second moment Γ based on Eq. (3.15) changes upon varying the position of $\tilde{\omega}$. To gain an additional insight, we now compare Γ to the case when the cascading processes are excluded from the calculation. Note that these contributions add noise in the lower half of the probe spectrum while subtracting noise in the upper half. The corresponding contributions are cancelled out almost completely when the entire probe spectrum is detected.

We next use the results for Γ to calculate the first correction due to the THz field to the probability distribution in Eq. (3.5), which is given by

$$P(\mathcal{S}, \theta) = \frac{1}{\sqrt{2\pi N}} \exp\left(-\frac{\mathcal{S}^2}{2N}\right) \left(1 + \frac{1}{2N^2}\left(\mathcal{S}^2 - N\right)\Gamma\right). \tag{3.16}$$

The correction to the bare probability distribution of the probe is represented by a single-photon state of the $\mathbf{e}_s$-polarized NIR field scaling linearly with the normally-ordered second moment of the electro-optic signal Γ in Eq. (3.8). Figure 3.6(a) compares the contour plot of the probability distribution in Eq. (3.16) to that for the bare shot noise of the probe and the probability distribution obtained by only considering the classical contribution Γ_{I}. Here, the polar angle does not represent θ, which corresponds to the phase shift induced by the waveplate shown in Fig. 1.2(a), but rather the corresponding phase shift $\varphi = \arccos\left(\sqrt{-\cos\theta}\right)$ induced in the electro-optic signal itself, which is given by $e^{i\varphi(\theta)} = P(\theta)$ [cf. Eq. (3.3)]. The noise added by the classical contribution Γ_{I} turns the rotationally symmetric probability distribution for the shot noise of the probe into an ellipse with the long axis along the direction of $\varphi = \pi/2$. The quantum correction given mainly by the cascading processes Γ_{III} then rotates the

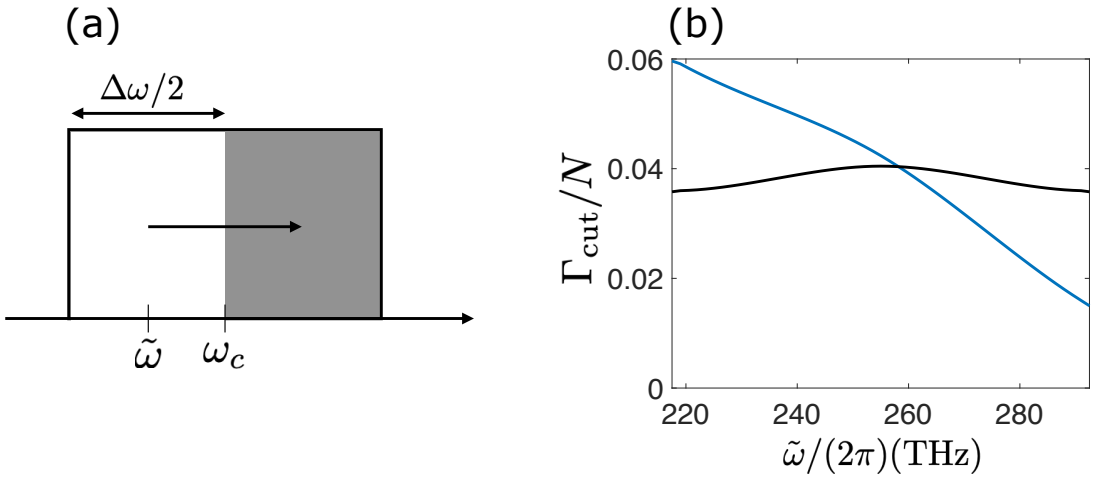

Figure 3.5: Spectral filtering in electro-optic sampling and effects of the cascading processes. (a) Spectral filtering in the gating function. For $\tilde{\omega}/(2\pi) = 217.5$ THz, the lower half of the probe spectrum is detected while $\tilde{\omega}/(2\pi) = 292.5$ THz constitutes a measurement of the upper half of the probe spectrum. (b) Comparison of the normally-ordered second moment Γ according to Eq. (3.15) between the classical treatment (black line), where only Γ_{I} is taken into account, and the full quantum treatment (blue line) involving also the cascading processes.

long axis of this ellipse and squeezes the generated NIR field $\hat{E}_{\mathrm{p},s}$ for phase shifts of $0.8\pi \lesssim \varphi \leq \pi$.

Ellipsometry enables a full tomography of the generated NIR field $\hat{E}_{\mathrm{p},s}$, as in standard balanced homodyne detection [104]. We now discuss whether the statistics of the THz field itself can be reconstructed from the statistics of the generated NIR field. Figure 3.6(b) shows this type of reconstruction for a phase shift of $\varphi = \pi/2$. In this case, the quantum corrections to Γ are negligible and the fluctuations added on top of the shot noise are mainly given by the classical contribution Γ_{I} which samples the fluctuations of the THz field and is therefore uncorrelated with the shot noise. Here, the probability distribution of the THz input is given by a simple deconvolution of the probability distribution in Eq. (3.16) with the Gaussian probability distribution for the shot noise of the probe. In contrast, the quantum correction dominated by the cascading processes Γ_{III} introduces an additional contribution for other phase shifts that is independent on the state of the THz field and cannot be understood as simply sampling the THz vacuum fluctuations. The cascading processes lead to interference with the $\mathbf{e}_s$-polarized NIR field $\hat{E}_{\mathrm{p},s}$ and therefore with the shot noise. A simple deconvolution of the probability distribution for the corresponding phase shifts φ would fail to give the correct statistics of the THz vacuum.

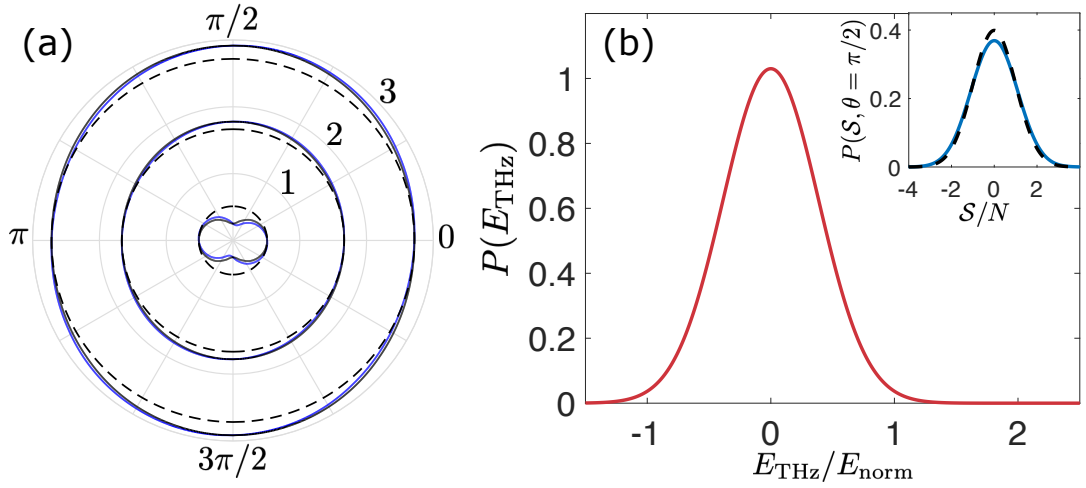

Figure 3.6: Statistics of the measured electro-optic signal $\hat{\mathcal{S}}(\theta)$ [cf. Eq. (3.3)] and reconstructed statistics of the THz vacuum. (a) Contour plot of the probability distribution of the electro-optic signal $\hat{\mathcal{S}}(\theta(\varphi))$. The blue line depicts the probability distribution according to Eq. (3.8), the black line shows the probability distribution resulting from the classical treatment, and the black dashed line depicts the probability distribution of the shot noise of the probe. (b) Reconstructed statistics of the THz vacuum with $E_{\mathrm{norm}} = \frac{c_0}{L\omega_{\mathrm{p}}\chi^{(2)}_{+--}}$. Note that the nonlinearity is independent of the frequency entries in the off-resonant case and can be treated as a constant prefactor. The blue line in the inset depicts the probability distribution of $\hat{\mathcal{S}}(\theta = \pi/2)$ and the dashed black line corresponds to the shot noise of the probe. Their deconvolution leads to the THz statisitics shown in the main figure.

3.6 Conclusion

We have employed the superoperator formalism to develop a microscopic theory for time-domain electro-optic sampling of electric field fluctuations. Three contributions to the electro-optic signal variance were identified: a classical contribution reproducing the results of previous theoretical models [7] and two quantum responses. One part originates from a contribution stemming from quantum susceptibilities and another one from cascaded nonlinear processes. The quantum corrections strongly depend on the intermolecular time-ordering of the THz interactions in the $\chi^{(2)}$ processes. Here, an effective interaction between the molecules mediated by the THz vacuum fluctuations is established. To demonstrate the difference between the classical and quantum responses, we compared the respective phase-dependent electro-optic contributions for an effective nonlinear medium described by a system of three-level non-interacting molecules. For a configuration involving a quarter-wave plate, we found that the quantum corrections to the normally-ordered second moment of the electro-optic signal van-

ish. In this case, the electro-optic signal is described by the conventional response also used for classical electro-optic sampling. For other phase shifts, however, the quantum response significantly influences the measured statistics and can also lead to a reduction of the fluctuations below the shot-noise limit of the probe field. For the configuration with a half-wave plate, the classical as well as the cascading processes can be suppressed completely, opening up the possibility to use electro-optic sampling as a novel spectroscopic tool to study quantum susceptibilities. The contribution due to the cascading processes should already be observable with slight changes in present experimental setups by either introducing spectral filtering or studying the electro-optic signal for certain phase shifts in the ellipsometry part. Finally, we describe how the probability distribution of the THz vacuum can be reconstructed from the one of the electro-optic signal as has been achieved experimentally [6]. We note that a reconstruction for other phase shifts would need to take into account the additional quantum contributions. We have shown that the ellipsometry enables detection of the probability distribution of the generated NIR field for phase shifts within an interval of length π, thus providing a full quantum tomography of its state. A method for reconstructing the statistics of the THz input for arbitrary phase shifts would pave a way for quantum tomography of nonclassical fields with subcycle temporal resolution. Our theory provides a firm basis for addressing the challenging issue of the extraction of these statistics under realistic experimental conditions.

Chapter 4

Effective Hamiltonian description of electro-optic sampling beyond paraxial approximation

4.1 Introduction

In the last chapter, we showed that the electro-optic process can be described by classical susceptibilities in the off-resonant case. This means that the microscopic theory can be replaced by a macroscopic description relying on an effective Hamiltonian. Here, the matter degrees of freedom can be traced out from the beginning and the effective Hamiltonian only describes the evolution of the field degrees of freedom. Furthermore, we showed in Fig. 3.4(b) that the cascading processes lead to an additional contribution to the electro-optic fluctuations for intermediate phase shifts of $\pi/2 < \theta < \pi$ and $\pi < \theta < 3\pi/2$. This contribution stems from time-ordering effects that can not be neglected due to the ultrashort sampling of the THz field by the probe. Alternatively, this effect can be explained through a coupling between the forwards and backwards propagating THz fields that is neglected by the slowly varying amplitude approximation employed in Ref. [7]. The fact that the backwards propagation of the THz field has to be taken into account suggests that contributions from other propagation directions need to be considered, too. Time-ordering effects have already been considered in frequency conversion and parametric down-conversion processes [81]. However, these models still rely on the SVAA where the frequency bandwidth of the involved fields is much shorter than their central frequencies and backwards propagating fields can be neglected.

In this chapter, we will develop an effective Hamiltonian describing the electro-optic

process. We take into account all propagation directions of the THz field in order to investigate their contribution to the fluctuations of the electro-optic signal. In order to do so, we go beyond the paraxial approximation for the description of the THz field. Arbitrary propagation directions of the THz field as well as field quantization effects due to resonances in the refractive index have already been described in terms of Green functions [50]. However, cascading effects were not considered in this case. We use the results of this work as an orientation for our own description and show that our effective Hamiltonian leads to the same results. Afterwards, we use our theory to also describe the cascading and time-ordering effects discovered in chapter 3 and extend them by including arbitrary propagation directions and phase-matching.

4.2 Effective Hamiltonian and field quantization

The electro-optic process can be described in terms of sum and difference frequency contributions (SFG and DFG, respectively). Therefore, the effective Hamiltonian is given by

$$\hat{H}_{\mathrm{int}}(t) = \varepsilon_0 d \int_V \mathrm{d}^3 r E_{p,z}(\mathbf{r},t) \left(\hat{E}_{\mathrm{THz},s}(\mathbf{r},t) + \hat{E}^{\dagger}_{\mathrm{THz},s}(\mathbf{r},t) \right) \hat{E}^{\dagger}_{p,s}(\mathbf{r},t) + H.c., \tag{4.1}$$

where d describes the strength of the second order susceptibility [7] and V is given by the volume of the nonlinear crystal. Note that we again assume a ZnTe-type crystal geometry since we already selected the respective vector components of the electric fields.

The NIR fields can be described well within the paraxial approximation [50]. Therefore, we will use the paraxial quantization [7, 15]

$$\hat{E}_{\mathrm{p},s}(\mathbf{r}_\perp;\omega) = i \sum_{l,p} \sqrt{\frac{\hbar\omega}{4\pi\epsilon_0 c_0 n}} \hat{a}_{s,l,p}(\omega) \mathrm{LG}_{l,p}(\mathbf{r}_\perp, r_\parallel = 0; k_\omega) \tag{4.2}$$

for the generated NIR field and Eq. (1.95) to describe the probe field $E_{\mathrm{p},z}$. Note that as in Ref. [7], n denotes the refractive index of ZnTe at the central frequency of the probe, $\mathrm{LG}_{l,p}$ denotes the Laguerre Gaussian polynomials [15, 105], and the crystal is considered short enough so that the beam waist of the fields can be considered constant over the entire crystal length. Furthermore, $\hat{a}_{s,l,p}(\omega)$ annihilates a photon of frequency ω, polarization s, and spatial mode $\mathrm{LG}_{l,p}$.

For the THz field, all propagation directions will be taken into account. In order to

do so, we start with the general quantization of the electric field in free space,

$$\hat{E}_{\mathrm{THz},s}(\mathbf{r},t) = i\sum_{\lambda}\int \mathrm{d}^3q\sqrt{\frac{\hbar\omega(q)}{16\pi^3\varepsilon_0}}\epsilon_s^{(\lambda)}(\mathbf{q})\hat{a}_\lambda(\mathbf{q})e^{i(\mathbf{q}\mathbf{r}-\omega(q)t)}. \tag{4.3}$$

Here, we sum over all polarization directions λ, while $\epsilon_s^{(\lambda)}$ denotes the s component of the respective polarization vector. The frequency $\omega(q) = c_0 q$ is given by the dispersion relation in the vacuum and $\hat{a}_\lambda(\mathbf{q})$ annihilates a photon with the wave vector $\mathbf{q}$ and the polarization λ. Now, we consider the wave vector in the form $\mathbf{q} = (\mathbf{q}_\perp, q_\parallel)^T$ with $\mathbf{q}_\perp = (q_s, q_z)^T$ as the wave vectors in the plane perpendicular to the propagation direction of the probe $E_{\mathrm{p},z}$. We can now split the integration over $q_\parallel$ into a positive and a negative part, describing the forwards and backwards propagating fields along the $q_\parallel$-axis, respectively. This leads to

$$\begin{aligned}\hat{E}_{\mathrm{THz},s}(\mathbf{r},t) = i\sum_{\lambda}\int \mathrm{d}^2q_\perp\int_0^\infty \mathrm{d}q_\parallel\sqrt{\frac{\hbar\omega(q)}{16\pi^3\varepsilon_0}}\epsilon_s^{(\lambda)}(\mathbf{q})e^{i(\mathbf{q}_\perp\mathbf{r}_\perp-\omega(q)t)} \\ \times\left[\hat{a}_\lambda(q_\parallel,\mathbf{q}_\perp)e^{iq_\parallel r_\parallel}+\hat{b}_\lambda(q_\parallel,\mathbf{q}_\perp)e^{-iq_\parallel r_\parallel}\right],\end{aligned} \tag{4.4}$$

where $\hat{b}_\lambda(q_\parallel,\mathbf{q}_\perp) = \hat{a}_\lambda(-q_\parallel,\mathbf{q}_\perp)$ annihilates a backwards propagating photon. Finally, we change the integral over $q_\parallel$ into an integral over the frequency of the field Ω using $q_\parallel = \sqrt{\Omega^2/c_0^2 - q_\perp^2}$ and $\mathrm{d}q_\parallel/\mathrm{d}\Omega = \Omega/(c_0^2 q_\parallel)$,

$$\begin{aligned}\hat{E}_{\mathrm{THz},s}(\mathbf{r},t) = i\sum_{\lambda}\int_0^\infty \mathrm{d}\Omega\int_{q>q_\perp}\mathrm{d}^2q_\perp\sqrt{\frac{\hbar\Omega^2}{16\pi^3\varepsilon_0 c_0^2 q_\parallel}}\epsilon_s^{(\lambda)}(\Omega,\mathbf{q}_\perp)e^{i(\mathbf{q}_\perp\mathbf{r}_\perp-\Omega t)} \\ \times\left[\hat{a}_\lambda(\Omega,\mathbf{q}_\perp)e^{iq_\parallel r_\parallel}+\hat{b}_\lambda(\Omega,\mathbf{q}_\perp)e^{-iq_\parallel r_\parallel}\right].\end{aligned} \tag{4.5}$$

Note that in changing the arguments of the annihilation operators, we used the rule $\hat{a}_\lambda(\mathbf{q}) = \sqrt{\mathrm{d}\Omega/\mathrm{d}q_\parallel}\,\hat{a}_\lambda(\Omega,\mathbf{q}_\perp)$, which ensures the conservation of the commutation relations

$$\left[\hat{a}_\lambda(\mathbf{q}),\hat{a}_\lambda^\dagger(\mathbf{q}')\right] = \delta(\mathbf{q}-\mathbf{q}') \equiv \frac{\mathrm{d}\Omega}{\mathrm{d}q_\parallel}\delta(\Omega-\Omega')\delta(\mathbf{q}_\perp-\mathbf{q}'_\perp) = \frac{\mathrm{d}\Omega}{\mathrm{d}q_\parallel}\left[\hat{a}_\lambda(\Omega,\mathbf{q}_\perp),\hat{a}_\lambda^\dagger(\Omega',\mathbf{q}'_\perp)\right].$$

Eq. (4.5) represents the quantization of the electric field in free space.

Inside media with refractive index n_Ω (and in cases where any resonances of this medium can be neglected, i.e. $\Im\{n_\Omega\} \ll 1$) the parallel wave vector $q_\parallel = \sqrt{(n_\Omega\Omega/c_0)^2 - q_\perp^2}$ simply has to be adjusted to account for the new dispersion relation $q = n_\Omega\Omega/c_0$. Eq. (4.5) represents a more general form of the quantized THz field than the planar

waves used in chapter 3 or the paraxial quantization used in Ref. [7].

4.3 Classical contribution

Here, we derive the classical contribution of the THz field to Γ. We show that our results coincide with the ones obtained in Ref. [50] verifying the correctness of the effective Hamiltonian given in Eq. (4.1) and the quantization of the THz field in Eq. (4.5).

The signal is given by

$$\hat{\mathcal{S}}(\theta) = 4\pi\varepsilon_0 c_0 n \int_0^\infty \mathrm{d}\omega \int \mathrm{d}^2 r_\perp \frac{1}{\hbar\omega} \left[P(\theta) E^*_{\mathrm{p},z}(\mathbf{r}_\perp;\omega) \hat{E}_{\mathrm{p},s}(\mathbf{r}_\perp;\omega) + H.c. \right]. \tag{4.6}$$

As in the last chapter, we are interested in the normally-ordered variance Γ of the electro-optic signal, which can be separated into a classical contribution Γ_{class} and a cascading contribution Γ_{casc},

$$\Gamma(\theta) = \langle :\hat{\mathcal{S}}^2(\theta): \rangle = \Gamma_{\mathrm{class}}(\theta) + \Gamma_{\mathrm{casc}}(\theta). \tag{4.7}$$

First, we want to focus on the classical contribution Γ_{class} which results from the first order correction to $\hat{E}_{\mathrm{p},s}$,

$$\hat{E}^{(1)}_{\mathrm{p},s}(\mathbf{r}_\perp,\omega) = \frac{i}{\hbar} \int_{-\infty}^{\infty} \mathrm{d}t \left[\hat{H}_{\mathrm{int}}(t), \hat{E}_{\mathrm{p},s}(\mathbf{r}_\perp,\omega) \right], \tag{4.8}$$

and is given by

$$\Gamma_{\mathrm{class}}(\theta) = \left(\frac{N\omega_p dl}{c_0 n} \right)^2 \frac{\hbar}{4\pi^2 \varepsilon_0 c_0} \int_0^\infty \mathrm{d}\Omega \; s(\Omega,\theta), \tag{4.9}$$

with

$$\begin{aligned} s(\Omega,\theta) = \int_{q>q_\perp} \mathrm{d}^2 q_\perp \frac{\Omega^2}{4\pi c_0 q_\parallel} \left(1 - \frac{q_s^2}{n_\Omega^2 \Omega^2 / c_0^2} \right) e^{-q_\perp^2 w_0^2/4} \\ \times g(\Omega,\theta) \left(\mathrm{sinc}^2 \left(\Delta k_- \frac{L}{2} \right) + \mathrm{sinc}^2 \left(\Delta k_+ \frac{L}{2} \right) \right). \end{aligned} \tag{4.10}$$

Here, we use the notation introduced in Ref. [7], i.e. N is given by Eq. (1.102) and ω_p is given by Eq. (1.103). We have introduced the sampling window

$$g(\Omega,\theta) = \left[|f_+(\Omega)|^2 - \Re\left\{ P(\theta)^2 f_+(\Omega) f_-(\Omega) \right\} \right], \tag{4.11}$$

with $f_\pm(\Omega)$ as the autocorrelation functions defined in Eq. (1.105). For the wave vector

mismatch $\Delta k_\pm = n_g\Omega/c_0 \pm q_\parallel$ we have approximated $k_{\omega\pm\Omega} - k_\omega = \pm n_g\Omega/c_0$, where $n_g = c_0\partial k/\partial\omega$ is the group refractive index evaluated at the center frequency ω_c.

Eq. (4.10) seems complicated but can be broken down into smaller building blocks. The first factor of its integrand originates from the first factor in the integrand of Eq. (4.5). The second factor $\sum_\lambda \epsilon_s^{(\lambda)}(\Omega, \mathbf{q}_\perp)^2 = 1 - q_s^2/(n_\Omega\Omega/c_0)^2$ originates from the polarization vectors and describes the contribution strength of the different propagation directions [11]. Note that fields propagating along the $\mathbf{e}_s$-direction do not contribute to the signal since only the s-component of the THz field interacts with the probe. The third factor $e^{-q_\perp^2 w_0^2/4}$ is essentially given by the Fourier transform of the spatial mode of the probe field, the fourth factor describes the sampling window of the THz vacuum fluctuations and the fifth factor describes the phase-matching for the forwards (Δk_-) and backwards (Δk_+) propagating THz fields.

Figure 4.1 compares the integrand $s(\Omega, \theta = \pi/2)$ for the full solution in Eq. (4.10) to the one obtained from the paraxial solution, where

$$s_{\text{parax}}(\Omega,\theta) = \frac{\Omega}{n_\Omega w_0^2} g(\Omega,\theta)\text{sinc}^2\left((n_g - n_\Omega)\frac{L\Omega}{2c_0}\right). \tag{4.12}$$

The paraxial approximation is obtained by neglecting all off-axis propagation directions ($q_\perp \approx 0$ and $q_\parallel = n_\Omega\Omega/c_0$) as well as the backwards propagation. Note that using this approximation in Eq. (4.9) leads to the same result as in Eq. (1.106). As discussed in Ref. [50], the paraxial approximation overestimates the contribution of the lower frequencies to the fluctuations of the electro-optic signal, since it considers the fields of all frequencies to propagate along the $r_\parallel$-axis. However, if an additional cut-off for frequencies $\nu \leq 20$ THz so that $n_\Omega\Omega > \pi c_0/w_0$ is introduced for the paraxial approximation, it serves as a reasonable approximation [50].

4.4 Cascading contribution

Having derived the classical contribution Γ_{class}, we now want to focus on the cascading contributions which result from the second order correction to $\hat{E}_{\text{p},s}$,

$$\begin{aligned}\hat{E}^{(2)}_{\text{p},s}(\mathbf{r}_\perp,\omega) &= -\frac{1}{\hbar^2}\int_{-\infty}^{\infty}\text{d}t\int_0^\infty \text{d}t'\left[\hat{H}_{\text{int}}(t),\left[\hat{H}_{\text{int}}(t-t'),\hat{E}_{\text{p},s}(\mathbf{r}_\perp,\omega)\right]\right]\\ &= \frac{d^2\varepsilon_0\omega}{4\pi\hbar c_0 n}\int_{-\infty}^{\infty}\text{d}t\int_0^\infty\text{d}t'\int_0^L\text{d}r_\parallel\int_V\text{d}^3r'\left(E_{\text{p},z}(\mathbf{r}',t)\hat{E}^\dagger_{\text{p},s}(\mathbf{r}',t) + H.c.\right)\\ &\qquad\times E_{\text{p},z}(\mathbf{r},t-t')\left[\hat{E}_{\text{THz},s}(\mathbf{r}',t) + H.c., \hat{E}_{\text{THz},s}(\mathbf{r},t-t') + H.c.\right].\end{aligned} \tag{4.13}$$

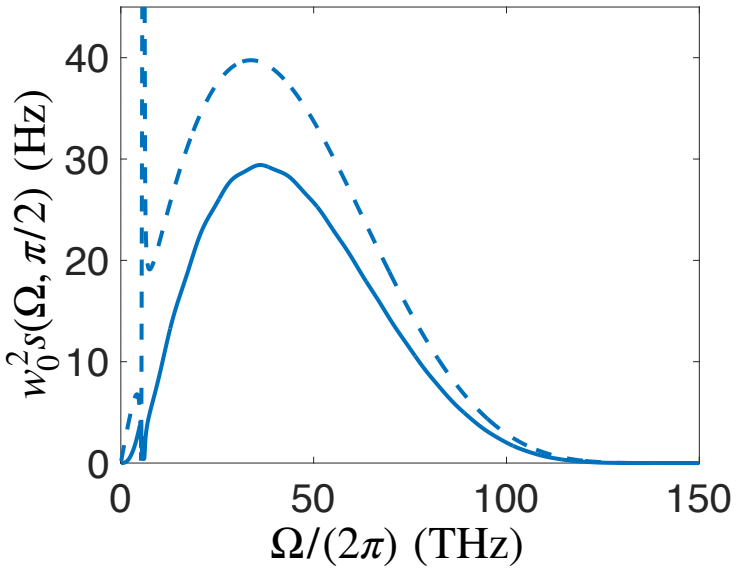

Figure 4.1: Classical contribution Γ_{class} to the fluctuations of the electro-optic signal including phase matching. The full line shows the solution including all propagation directions according to Eq. 4.10. The dashed line shows the solution according to the paraxial approximation in Eq. 4.12. The refractive index n_Ω is given in Eq. (1.98). We used a length of $L = 7$ μm, a beam waist of $w_0 = 3$ μm and a group refractive index of $n_g = 2.9$. The parameters used are taken from Ref. [7].

Note that the same transformation as in Appendix B has been applied here to avoid time-dependent integral boundaries due to the time ordering. In this case t' denotes the time interval between the two interactions of the THz field with the probe field. As discussed in chapter 3, the cascading contribution does not depend on the state of the THz field. This can also be seen here, since Eq. 4.13 involves the commutator of the THz fields. Physically, this describes the generation of a THz photon during the first $\chi^{(2)}$ process and its subsequent absorption in a second $\chi^{(2)}$ process.

Using Eq. (4.13), Γ_{casc} can be calculated to

$$\Gamma_{\text{casc}}(\theta) = \left(\frac{N\omega_p dL}{c_0 n}\right)^2 \frac{\hbar}{4\pi^2 \varepsilon_0 c_0} \int_0^\infty \mathrm{d}\Omega \; s_{\text{casc}}(\Omega, \theta) \tag{4.14}$$

with

$$s_{\mathrm{casc}}(\Omega,\theta) = \frac{1}{2\pi}\int_{q>q_\perp} \mathrm{d}^2 q_\perp \frac{\Omega^2}{4\pi c_0 q_\parallel}\left(1-\frac{q_s^2}{n_\Omega^2\Omega^2/c_0^2}\right) e^{-q_\perp^2 w_0^2/4} \\ \times \mathrm{p.v.}\int_{-\infty}^{\infty}\mathrm{d}\Omega' \frac{1}{\Omega-\Omega'}\Im\left\{P(\theta)^2 f_-(\Omega')f_+(\Omega')\right\} \\ \times\left(\mathrm{sinc}^2\left((n_g\Omega'-q_\parallel)\frac{L}{2c_0}\right)+\mathrm{sinc}^2\left((n_g\Omega'+q_\parallel)\frac{L}{2c_0}\right)\right). \tag{4.15}$$

Here, p.v. denotes the Cauchy principal value of the followed integral [106]. The factor $\frac{1}{\Omega-\Omega'}$ is a direct consequence of the time-ordering of the expansion and originates from the integration over the time interval between the two $\chi^{(2)}$ processes t' in Eq. (4.13),

$$\int_0^\infty \mathrm{d}t' e^{-i(\Omega-\Omega')t'} = \pi\delta(\Omega-\Omega') - \frac{i}{\Omega-\Omega'}. \tag{4.16}$$

Here, the δ-function describes the part of the process where energy is conserved at each single $\chi^{(2)}$ process. In this case, the time ordering is represented by the fact that the integral is bounded from below, which ensures that the first $\chi^{(2)}$ process happens before the second one. Removing the lower bound would only result in a δ function. Therefore, the second term in Eq. (4.16) describes the case where energy is transferred between the first and the second $\chi^{(2)}$ interaction so that it is only conserved for both processes combined. Equation 4.15 shows that Γ_{casc} is solely given by processes where energy is not conserved at each single $\chi^{(2)}$ process.

Note that the sampling window $g(\Omega,\theta)$ in Eq. (4.11) differs from $|D(\Omega,\theta)|^2$ in Eq. (3.9)[1]. In this chapter, no contribution is obtained from pure SFG processes, which is apparent due to the lack of any term proportional to $|f_-(\Omega)|^2$ in Eq. (4.11), while the contribution due to pure DFG processes $|f_+(\Omega)|^2$ is twice as large as in $|D(\Omega,\theta)|^2$. In contrast, $|D(\Omega,\theta)|^2$ does involve pure SFG processes. However, these terms are counteracted by identical contributions of opposite signs from cascading processes in Eq. (3.13) that are absent in the cascading contribution derived in Eq. (4.14). These additional cascading contributions ensure the equivalence of the results for Γ derived here and in the previous chapter. Note that the classical contribution in Ref. [7] is identical to $|D(\Omega,\theta)|^2$. It gives the correct result for the electro-optic fluctuations if the signal is measured over the entire probe spectrum (as is the case described there) but needs to be corrected by the cascading contribution if only part of the probe spectrum is measured. In summary, both descriptions lead to identical results but offer different

[1]Note that $D(\Omega,\theta)$ defined in Eq. (3.10) still involves the susceptibilities $\chi^{(2)}$. For this discussion, we consider the off-resonant case in which the susceptibilities become frequency independent and neglect their presence in the definition of $D(\Omega,\theta)$ for the moment. The same argument holds for $D_{\mathrm{casc}}(\Omega,\theta)$ in Eq. (3.14) in the following argument.

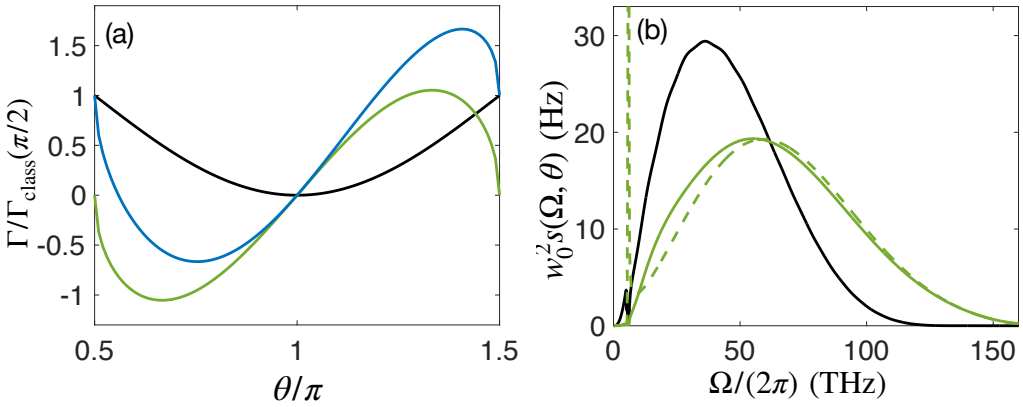

Figure 4.2: Comparison of the classical and cascading contributions to Γ. The values for the beam waist of the probe and the length of the crystal are the same as for Fig. 4.1. (a) The classical contribution (black line), the cascading contribution Γ_{casc} (green line), and their sum Γ (blue line) are shown. (b) Comparison of the THz vacuum fluctuations contributing to Γ_{class} for $\theta = \pi/2$ (black line) and to Γ_{casc} for $\theta_{\mathrm{max}} = 4\pi/3$ (green line) according to Eqs. (4.10) and (4.15), respectively. The green dashed line depicts the cascading contributions in the paraxial approximation.

physical interpretations for the generation of the electro-optic fluctuations.

Figure 4.2(a) depicts the phase dependence of the classical and cascading contributions and shows that their respective maximal values are almost identical. Figure 4.2(b) compares $s_{\mathrm{casc}}(\Omega, \theta_{\mathrm{max}})$ to $s(\Omega, \theta = \pi/2)$ for the values specified in the caption of Fig. 4.1. Here, $\theta_{\mathrm{max}} = 4\pi/3$ is the phase shift which maximizes $\int_0^\infty \mathrm{d}\Omega\ s_{\mathrm{casc}}(\Omega, \theta)$. The figure shows that $s_{\mathrm{casc}}(\Omega, \theta_{\mathrm{max}})$ decays much slower than $s(\Omega, \theta = \pi/2)$. Therefore, contributions from THz vacuum fluctuations of higher frequencies are stronger for Γ_{casc} compared to Γ_{class}. Equation (4.15) shows that this can be explained due to better phase-matching conditions for the cascading processes. In comparison to $s(\Omega, \theta)$, the two sinc-functions in $s_{\mathrm{casc}}(\Omega, \theta)$ show two different frequencies Ω and Ω' in their arguments which are a result of the energy transfer between the two successive $\chi^{(2)}$ processes. This frequency mismatch can compensate the phase mismatch between the NIR fields and the THz field. Therefore, the relaxed energy conservation for the single $\chi^{(2)}$ processes leads to overall better phase matching conditions. Additionally, the dashed line in Fig. 4.2(b) shows $s_{\mathrm{casc}}(\Omega, \theta_{\mathrm{max}})$ in the paraxial approximation for the THz field which is obtained equivalently to Eq. (4.12) for the classical contribution. It is apparent that the off-axis propagating THz fields (with respect to the probe) are only relevant for lower THz frequencies and overall play a negligible role for Γ_{casc}; neglecting them leads to a decrease of 2% in Γ_{casc}.

In chapter 3, we derived the cascading contribution for the case of perfect phase

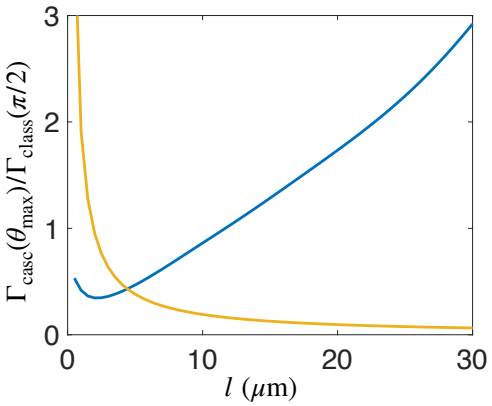

Figure 4.3: Comparison of the relative contribution of $\Gamma_{\mathrm{casc}}(\theta_{\mathrm{max}})$ with respect to $\Gamma_{\mathrm{class}}(\pi/2)$. The blue line depicts the case including the phase matching and is calculated according to Eqs. (4.9) and (4.14). The yellow line shows the case of perfect phase matching where $n_g = n_\Omega = 1$. Here, a large beam waist of $w_0 = 100$ μm was used such that propagation directions not aligned with the $q_\parallel$-axis can be neglected.

matching, where $n_g = n_\Omega = 1$. Figure 4.3(a) compares the relative size of Γ_{casc} with respect to Γ_{class} to the case of perfect phase matching (Γ_{III} given in Eq. (3.13) for the off-resonant case). A directly opposite behaviour of the curves can be observed. Equation (3.13) shows that in the case of perfect phase matching, the cascading contribution scales linearly with the length of the crystal L, while the classical contribution scales quadratically with L. This was explained by the fact that the energy transfer between successive $\chi^{(2)}$ processes can only happen within a certain distance, determined by the respective generated THz field, while the classical contribution does not limit the distance between the two independent $\chi^{(2)}$ processes. Therefore, the cascading contribution becomes negligible for longer crystals. In contrast, increasing the crystal length leads to larger relative cascading contributions if phase matching is included. This effect can be explained due to the fact that the phase matching counteracts the quadratic scaling of the classical contribution with respect to the crystal length and eventually also reverts the scaling such that increasing the crystal length reduces the classical contribution. For Γ_{casc}, however, the phase matching can be counteracted with the relaxed energy conservation law as explained in the previous paragraph, which means that almost no change in the scaling behaviour of the cascading contributions with respect to the crystal length can be observed.

The classical contribution involves the detection window $g(\Omega, \theta)$, given in Eq. (4.11). In comparison, the cascading contribution involves the autocorrelation function $\Im\left\{P(\theta)^2 f_-(\Omega') f_+(\Omega')\right\}$. This suggests that the cascading contribution can be suppressed if only part of the probe spectrum is measured. The autocorrelation function

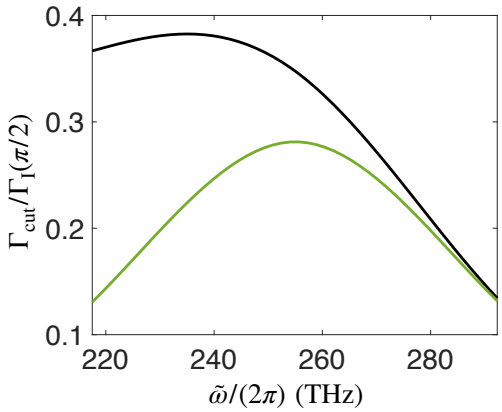

Figure 4.4: Spectrally filtered classical and cascading contribution to the electro-optic fluctuations. The black line shows the classical contribution spectrally filtered according to Eq. (4.17) for a phase shift of $\theta = \pi/2$. The green line shows the corresponding cascading conrtibution for $\theta = \theta_{\max}$.

$f_-(\Omega)$ is associated with SFG processes and therefore is most dominant if the upper half of the probe spectrum is measured. In contrast, $f_+(\Omega)$ is most dominant if the lower half of the probe spectrum is measured since it is associated with DFG processes. The cascading contribution results from the emission of a THz photon due to a DFG process and its subsequent reabsorption in a SFG process. Therefore, its contribution should be strongest in the middle of the probe spectrum since both SFG and DFG processes contribute equally in that frequency range and vanish in the wings of the probe spectrum where either DFG or SFG processes are suppressed.

In Fig. 4.4, we compare the cascading contribution to the classical contribution for different cases of spectral filtering as in Fig. 3.5(a). The signal is given analogous to Eq. (3.15),

$$\hat{\mathcal{S}}_{\mathrm{cut}}(\tilde{\omega},\theta) = 4\pi\varepsilon_0 c_0 n \int_{\tilde{\omega}-\Delta\omega/4}^{\tilde{\omega}+\Delta\omega/4} \mathrm{d}\omega \int \mathrm{d}^2 r_\perp \frac{1}{\hbar\omega} \left[P(\theta) E^*_{\mathrm{p},z}(\mathbf{r}_\perp;\omega) \hat{E}_{\mathrm{p},s}(\mathbf{r}_\perp;\omega) + H.c. \right]. \tag{4.17}$$

The cascading contribution indeed has its maximum when the middle of the probe spectrum is measured. The classical contribution results from both a mixture of DFG and SFG processes and pure DFG processes. As is visible in Fig. 4.4, this means that it is most dominant if only frequencies in the lower half of the probe spectrum are measured. In conclusion, this shows that the cascading contribution can be suppressed if only the lower half of the probe spectrum is measured. In this case, the electro-optic fluctuations are mainly given by DFG processes. Measuring even smaller frequency

windows at the lower end of the frequency spectrum of the probe would increase this effect.

4.5 Conclusion

In this chapter, we have provided an effective Hamiltonian that can model the electro-optic process in the off-resonant regime. In general, the effective Hamiltonian in Eq. (4.1) can be used as a general starting point. Different levels of approximations for the quantization of the fields and their propagation directions can then be employed.

Here, we have kept the generated NIR field $\hat{E}_{\mathrm{p},s}$ in the paraxial approximation and allowed for arbitrary propagation directions of the THz field. The resulting classical contribution agrees with alternative results relying on a Green function approach for the propagation of the involved fields [50, 51], which confirms the validity of the quantization of the THz field derived in this chapter. Extending the results presented in the mentioned references, we also discuss effects due to cascading processes. Here, we extend the description of the cascading process of chapter 3 to also include off-axis propagation of the THz field and phase matching. We find that both effects increase the relative strength of the cascading contribution, which is given by processes where energy transfer happens between the consecutive $\chi^{(2)}$ processes. Here, the relaxed energy conservation law for each single $\chi^{(2)}$ processes is able to counteract the phase mismatch between the interacting fields, which means that phase matching affects the classical contribution more than the cascading contribution. Finally, we have also seen that the cascading contribution results from a DFG process, emitting a THz photon and it's consecutive reabsorption due to a SFG process, while the classical contribution is given by either a mixture of DFG and SFG process or two DFG processes. Therefore, their relative contribution to the electro-optic fluctuations can not only be controlled via the induced phase shift θ, but also by introducing spectral filtering.

So far, we have assumed that the crystal is short enough to ensure a constant beam waist of the NIR fields across its entire length. The beam divergence can be considered by taking into account the full z-dependence of the Laguerre Gaussian polynomials $\mathrm{LG}_{l,p}(\mathbf{r}_\perp, z; \omega)$ in Eq. (4.2), as was already done for the classical contribution in Ref. [51]. Furthermore, small corrections to the effective Hamiltonian in Eq. (4.1) can be used to describe the squeezing process in chapter 2, since the squeezing results from essentially the same electro-optic process that is described in this chapter. This modified Hamiltonian and the derived quantization for the fields can then be used to investigate the effect of the energy transfer between consecutive $\chi^{(2)}$ processes. We expect the resulting corrections to the field fluctuations to be small since the two involved

fields are both THz fields with similar spectra so that the phase matching between the fields is almost perfect.

Chapter 5

Quantum tomography of few-cycle modes

5.1 Introduction

Quantum state tomography describes the complete experimental characterization of quantum states [107]. In quantum optics, homodyne detection is a ubiquitous tool for the characterization of quantum states of light. Here, the probability distribution of the field quadratures is measured by amplifying the investigated field with a classical local oscillator [108, 109]. Afterwards, the Wigner function can be obtained from the measured probability distribution [10, 48, 110]. The local oscillator employed in homodyne detection selects a mode of the field, in which it is being sampled.

Temporal modes can be used if the investigated field consists of a pulsed state [48]. In order to characterize the full state, the field needs to be probed in a complete basis state of modes. Usually, the mode of the local oscillator is matched to the sampled field, so that only a few number of modes actually need to be sampled in order to fully characterize the state. In order to obtain an estimation of the temporal profile of the investigated field, the modal overlap for different delay times between the local oscillator and the sampled field can be studied [111]. Alternatively, the Wigner function can also be directly sampled by photon resolving detectors [112]. Usually, even broadband temporal modes still possess a well defined central frequency which is bigger than their bandwidth.

In the fields of quantum information science and technology, temporal modes play an important role since they provide a natural basis in which information can be encoded [113–115]. Here, SFG and DFG processes can be used as beam-splitter-like processes where two separated frequency intervals replace the two input ports of con-

ventional beam splitters [114, 116]. This suggests that electro-optic sampling can also be viewed equivalently as a balanced homodyne detection scheme of an upconverted THz temporal mode. Electro-optic sampling thus provides a couple of advantages in comparison to standard balanced homodyne detection. First, the development of highly sensitive and efficient THz photon detectors is a challenging and ongoing task. Electro-optic sampling circumvents this problem by upconverting the sampled THz state into the NIR frequency range, where photon detectors with very high quantum efficiencies are readily available. Secondly, the electro-optic process, acting like a nonlinear beam splitter, could in principle be used to select specific THz modes for balanced homodyne detection, thus leaving the other modes intact for further processing. Lastly, the electro-optic process can be used to probe ultrashort temporal profiles of the THz field corresponding to few-cycle pulses.

Here, we show that the probability distribution of the sampled THz field can indeed be reconstructed from the measured probability distribution of the electro-optic signal, from which the corresponding Wigner function can be obtained by tomographic means. In this case, the sampled temporal mode of the THz field is given by a femtosecond few-cycle pulse. In order to reconstruct the probability distribution of the sampled THz field and to obtain the shape of its temporal mode, the measured probability distribution needs to be deconvolved with a Gaussian function, whose variance is given by the shot noise of the probe and a small correction due to the electro-optic process. A precise theoretical model of the electro-optic process for the sampling of the THz vacuum field is needed to calculate these corrections to the shot noise and to obtain the shape of the temporal mode of the THz field selected by the probe.

As a proof of concept, we give an example of such a reconstruction and the shape of the temporal THz mode selected by the probe for the case of an ultrashort, few-cycle THz cat state. In order to do so, we use the analytical solution derived in chapter 2 to model the electro-optic process. The results of chapter 4 can be used in the future to obtain more precise models of the electro-optic process.

5.2 Setup

We consider the same setup shown in Fig. 1.2(a), where the signal is given by

$$\hat{\mathcal{S}}(\theta) = C \int_0^\infty \mathrm{d}\omega \, \frac{\mathcal{F}(\omega)}{\hbar\omega} \left[P(\theta) E^*_{\mathrm{p},z}(\omega) \hat{E}_{\mathrm{p},s}(\omega) + H.c. \right]. \tag{5.1}$$

Here, $C = 4\pi\varepsilon_0 A c_0$ with A as the effective transverse area determined by the beam waist of the probe field, c_0 the speed of light in vacuum, ε_0 the vacuum permittivity and

$P(\theta) = \sqrt{-\cos(\theta)} + i\sqrt{2}\cos(\theta/2)$. We have also inserted a spectral filtering function $\mathcal{F}(\omega)$ which describes the case when only a part of the spectrum of the probe is measured. Note that in contrast to Eq. (3.3), we are considering the probe to be classical already in the definition of the signal.

This signal can also be rewritten in terms of a multimode annihilation operator $\hat{b}(\theta)$,

$$\hat{\mathcal{S}}(\theta) = \hat{b}(\theta) + \hat{b}^\dagger(\theta), \tag{5.2}$$

where

$$\hat{b}(\theta) = \sqrt{N}P(\theta)\int_0^\infty \mathrm{d}\omega\ h(\omega)\hat{a}_s(\omega), \tag{5.3}$$

$N = C\int_0^\infty \mathrm{d}\omega |\mathcal{F}(\omega)E_{\mathrm{p},z}(\omega)|^2/(\hbar\omega)$ is the shot noise of the spectrally filtered probe, and $\hat{a}_s(\omega)$ annihilates an s-polarized photon of frequency ω. In order to match Eq. (5.2) to Eq. (5.1), we define the ultrabroadband frequency mode

$$h(\omega) = i\frac{\mathcal{F}(\omega)E^*_{\mathrm{p},z}(\omega)/\sqrt{\omega}}{\sqrt{\int_0^\infty \mathrm{d}\omega |\mathcal{F}(\omega)E_{\mathrm{p},z}(\omega)|^2/\omega}}, \tag{5.4}$$

such that $\int_0^\infty \mathrm{d}\omega |h(\omega)|^2 = 1$ and therefore $\left[\hat{b}(\theta), \hat{b}^\dagger(\theta)\right] = N$. The signal can thus be alternatively understood as a homodyne detection of the s-polarized state according to a local oscillator mode $h(\omega)$ essentially given by the probe $E_{\mathrm{p},z}$. This means that the ellipsometry scheme in Fig. 1.2(a), consisting of the waveplate, the Wollaston Prism and the two detectors, can be regarded as equivalent to a homodyne detection setup, where the waveplate is used to control the phase of the local oscillator, the Wollaston Prism replaces the beam splitter, and the two polarization directions act as the two input ports of the beam splitter.

In the case of electro-optic sampling, we are specifically interested in the NIR field generated through the interaction of the probe with a given THz quantum field inside the electro-optic crystal. The goal is then to reconstruct the statistics of said THz field from the statistics of the generated NIR field. As derived in chapter 3, the probability

distribution of the electro-optic signal is given by

$$\begin{aligned} P(\mathcal{S},\theta) &= \frac{1}{\sqrt{2\pi N}}\langle 0_{\mathrm{NIR}}, \Psi_{\mathrm{THz}}|\hat{U}^\dagger : e^{-\frac{(\mathcal{S}-\hat{\mathcal{S}}(\theta))^2}{2N}} : \hat{U}|\Psi_{\mathrm{THz}}, 0_{\mathrm{NIR}}\rangle \\ &= \frac{1}{\sqrt{2\pi N}}\sum_{k=0}^{\infty}\frac{1}{(2N)^{k/2}k!}H_k(\mathcal{S}/\sqrt{2N})\exp\left(-\frac{\mathcal{S}^2}{2N}\right) \\ &\qquad \times \langle 0_{\mathrm{NIR}}, \Psi_{\mathrm{THz}}|\hat{U}^\dagger : \hat{\mathcal{S}}^k(\theta) : \hat{U}|\Psi_{\mathrm{THz}}, 0_{\mathrm{NIR}}\rangle, \end{aligned} \tag{5.5}$$

with $H_k(x)$ as the Hermite polynomials. Here, the evolution operator $\hat{U}$ is used to describe the electro-optic process inside the crystal and $|\Psi_{\mathrm{THz}}, 0_{\mathrm{NIR}}\rangle = |\Psi_{\mathrm{THz}}\rangle \otimes |0_{\mathrm{NIR}}\rangle$ denotes the initial (separable) state of the s-polarized THz and NIR field, respectively.

5.3 Theoretical reconstruction of the THz statistics

We have seen in the previous chapters, that the electro-optic process results from both DFG processes, which couple annihilation and creation operators, and SFG processes, which couple annihilation operators of different frequencies. Therefore, the evolution of $\hat{b}$ under $\hat{U}$ can be described in general by a Bogoliubov transformation of the form

$$\hat{U}^\dagger\hat{b}(\theta)\hat{U} = \hat{\alpha}(\theta) + \hat{\beta}^\dagger(\theta), \tag{5.6}$$

where we have separated the operator $\hat{U}^\dagger\hat{b}(\theta)\hat{U}$ into its annihilation

$$\hat{\alpha}(\theta) = \sqrt{N}P(\theta)\iint_0^\infty \mathrm{d}\omega\mathrm{d}\overline{\omega}\; h(\omega)p(\omega,\overline{\omega})\hat{a}_s(\overline{\omega}) \tag{5.7}$$

and creation

$$\hat{\beta}^\dagger(\theta) = \sqrt{N}P(\theta)\iint_0^\infty \mathrm{d}\omega\mathrm{d}\overline{\omega}\; h(\omega)q(\omega,\overline{\omega})\hat{a}_s^\dagger(\overline{\omega}) \tag{5.8}$$

part, such that $\hat{\alpha}(\theta)|0\rangle = 0$ and $\hat{\beta}(\theta)|0\rangle = 0$. Here, we use the most general form of the Bogoliubov transformation, which means that the only restriction to the operators $\hat{\alpha}(\theta)$ and $\hat{\beta}(\theta)$ is

$$\left[\hat{b}(\theta), \hat{b}^\dagger(\theta)\right] = \left[\hat{U}^\dagger\hat{b}(\theta)\hat{U}, \hat{U}^\dagger\hat{b}^\dagger(\theta)\hat{U}\right] = \left[\hat{\alpha}(\theta), \hat{\alpha}^\dagger(\theta)\right] - \left[\hat{\beta}(\theta), \hat{\beta}^\dagger(\theta)\right] = N, \tag{5.9}$$

so that, accordingly, $\int_0^\infty \mathrm{d}\omega\;\left[p(\omega_1,\omega)p^*(\omega_2,\omega) - q(\omega_1,\omega)q^*(\omega_2,\omega)\right] = \delta(\omega_1-\omega_2)$. Note that the operator $\hat{b}(\theta)$ in Eq. (5.3) only acts on NIR frequencies due to the selected broadband mode $h(\omega)$ of the probe, given in Eq. (5.4). In contrast, the transformed operator $\hat{U}^\dagger\hat{b}(\theta)\hat{U}$ in Eq. (5.6) acts on both the NIR and THz frequencies, since the

Bogoliubov transformation couples these two frequency regimes through the functions $p(\omega,\overline{\omega})$ and $q(\omega,\overline{\omega})$ in Eqs. (5.7) and (5.8).

We can now use this Bogoliubov transformation to bring the operator $\hat{U}^\dagger :\hat{\mathcal{S}}^k(\theta):\hat{U}$ in the third line of Eq. (5.5) into its normally-ordered form

$$\begin{aligned}
\hat{U}^\dagger :\hat{\mathcal{S}}^k:\hat{U} &= \sum_{l=0}^{k}\binom{k}{l}(\hat{\alpha}^\dagger+\hat{\beta})^{k-l}(\hat{\alpha}+\hat{\beta}^\dagger)^l \\
&= \sum_{l=0}^{k}\binom{k}{l}\sum_{i,j=0}^{k-l}\sum_{s,t=0}^{l} I_{i,j}^{(k-l)}\left([\hat{\beta},\hat{\alpha}^\dagger]\right) I_{s,t}^{(l)}\left([\hat{\alpha},\hat{\beta}^\dagger]\right)\hat{\alpha}^{\dagger i}\hat{\beta}^j\hat{\beta}^{\dagger s}\hat{\alpha}^t \\
&= \sum_{l=0}^{k}\binom{k}{l}\sum_{i,j=0}^{k-l}\sum_{s,t=0}^{l}\sum_{r=0}^{\min(j,s)} I_{i,j}^{(k-l)}\left([\hat{\beta},\hat{\alpha}^\dagger]\right) I_{s,t}^{(l)}\left([\hat{\alpha},\hat{\beta}^\dagger]\right)\binom{j}{r}\binom{s}{r} \\
&\qquad\qquad \times r![\hat{\beta},\hat{\beta}^\dagger]^r\hat{\alpha}^{\dagger i}\hat{\beta}^{\dagger s-r}\hat{\beta}^{j-r}\hat{\alpha}^t,
\end{aligned} \tag{5.10}$$

where we have omitted the dependencies on θ. In the first line, we have used the unitarity $\hat{U}\hat{U}^\dagger = 1$ of the operator $\hat{U}$ to transform both $\hat{b}$ and $\hat{b}^\dagger$. In the second line, we used the formula $(\hat{\alpha}+\hat{\beta}^\dagger)^l = \sum_{s,t=0}^{l} I_{s,t}^{(l)}\left([\hat{\alpha},\hat{\beta}^\dagger]\right)\hat{\beta}^{\dagger s}\hat{\alpha}^t$, with

$$I_{s,t}^{(l)}(x) = \begin{cases} \frac{l!}{2^{\frac{l-s-t}{2}}(\frac{l-s-t}{2})!s!t!}x^{\frac{l-s-t}{2}} & \text{if } l-s-t \text{ even} \\ 0 & \text{if } l-s-t \text{ odd} \end{cases} \tag{5.11}$$

which can be derived by equating coefficients in the Baker-Campbell-Hausdorff formula $e^{z(\hat{\alpha}+\hat{\beta}^\dagger)} = e^{z\hat{\beta}^\dagger}e^{z\hat{\alpha}}e^{z^2[\hat{\alpha},\hat{\beta}^\dagger]/2}$. In the last line, we have transformed the operator $\hat{\beta}^j\hat{\beta}^{\dagger s}$ into its normally-ordered form, which can also be done by equating coefficients in the Baker-Campbell-Hausdorff formula $e^{z\hat{\beta}}e^{z\hat{\beta}^\dagger} = e^{z\hat{\beta}^\dagger}e^{z\hat{\beta}}e^{z^2[\hat{\beta},\hat{\beta}^\dagger]}$.

Equation (5.10) can now be simplified further by first combining the annihilation operators and then the creation operators. The creation and annihilation operators can then also be combined using normal ordering $:\bullet:$,

$$\hat{U}^\dagger :\hat{\mathcal{S}}^k:\hat{U} = \sum_{m=0}^{k}\binom{k}{m}(k-m-1)!!\kappa^{\frac{k-m}{2}} :\left(\hat{\alpha}+\hat{\beta}+\hat{\alpha}^\dagger+\hat{\beta}^\dagger\right)^m:, \tag{5.12}$$

where $(k-m-1)!! = \frac{(k-m)!}{2^{\frac{k-m}{2}}\frac{k-m}{2}!}$ if $k-m$ is even and $(k-m-1)!! = 0$ if $k-m$ is odd. Here,

$$\kappa(\theta) = 2\left[\hat{\beta}(\theta),\hat{\beta}^\dagger(\theta)\right] + \left(\left[\hat{\alpha}(\theta),\hat{\beta}^\dagger(\theta)\right] + H.c.\right) = \langle 0_{\text{NIR}},0_{\text{THz}}|\hat{U}^\dagger :\hat{\mathcal{S}}^2(\theta):\hat{U}|0_{\text{THz}},0_{\text{NIR}}\rangle \tag{5.13}$$

is given by the normally ordered second moment of the electro-optic signal for $|\Psi_{\mathrm{THz}}\rangle = |0_{\mathrm{THz}}\rangle$ and the corresponding normally ordered kth-moment is given by $(k-1)!!\kappa^{\frac{k}{2}}(\theta)$. Note that the commutator $\left[\hat{\alpha}(\theta), \hat{\alpha}^{\dagger}(\theta)\right]$ does not contribute to $\kappa(\theta)$, while the commutator $\left[\hat{\beta}(\theta), \hat{\beta}^{\dagger}(\theta)\right]$ contributes twice. This is a result of the normal ordering in Eq. (5.5). The operator $\hat{\alpha}(\theta)$ can be essentially identified as the SFG contribution, which does not generate any photons from the vacuum. Correspondingly, $\hat{\beta}(\theta)$ is identified with the DFG contribution, which generates both NIR and THz photons.

Inserting Eq. (5.12) back into Eq. (5.5), we finally obtain

$$P(\mathcal{S},\theta) = \frac{1}{\sqrt{2\pi[N+\kappa(\theta)]}}\langle 0_{\mathrm{NIR}}, \Psi_{\mathrm{THz}}| : \exp\left(-\frac{\left(\mathcal{S}-\hat{U}^{\dagger}\hat{\mathcal{S}}(\theta)\hat{U}\right)^2}{2(N+\kappa(\theta))}\right) : |\Psi_{\mathrm{THz}}, 0_{\mathrm{NIR}}\rangle. \tag{5.14}$$

Equation (5.14) looks very similar to the first line of Eq. (5.5), however, we have replaced the shot noise $N = \langle 0_{\mathrm{NIR}}|\hat{\mathcal{S}}^2(\theta)|0_{\mathrm{NIR}}\rangle$ by $N+\kappa(\theta) = \langle 0_{\mathrm{NIR}}, 0_{\mathrm{THz}}|\hat{U}^{\dagger}\hat{\mathcal{S}}^2(\theta)\hat{U}|0_{\mathrm{THz}}, 0_{\mathrm{NIR}}\rangle$ and have pulled the evolution operators inside of the normal-ordering operation $: \bullet :$. As a result, the transformed electro-optic signal $\hat{U}^{\dagger}\hat{\mathcal{S}}(\theta)\hat{U} = \hat{\alpha}(\theta)+\hat{\beta}(\theta)+H.c.$ now not only acts on the s-polarized NIR state $|0_{\mathrm{NIR}}\rangle$, but also on the THz state $|\Psi_{\mathrm{THz}}\rangle$. Therefore, the electro-optic process preserves the Gaussian properties of incoming states[1], so that, e.g., for $|\Psi_{\mathrm{THz}}\rangle = |0\rangle$ the initial variance N in Eq. (5.5) for $\hat{U} = \mathbb{1}$ is simply changed to the variance $N+\kappa(\theta)$ in Eq. (5.14). This is not surprising since it results from a mixture of SFG and DFG processes, and squeezing processeses are known to have this property [117].

The probability distribution in Eq. (5.14) is given by a normally-ordered operator and the s-polarized NIR state is in the ground state $|0_{\mathrm{NIR}}\rangle$. Thus, it is easy to see that we only need to take into account the part of the transformed electro-optic signal $\hat{U}^{\dagger}\hat{\mathcal{S}}(\theta)\hat{U}$ that acts on the THz state. In order to do so, we split the transformed electro-optic signal into a part $\hat{\tilde{\mathcal{S}}}_{\mathrm{NIR}}(\theta)$ that acts on the NIR state and a part $\hat{\tilde{\mathcal{S}}}_{\mathrm{THz}}(\theta)$ that acts on the THz state,

$$\hat{U}^{\dagger}\hat{\mathcal{S}}\hat{U} = \hat{\tilde{\mathcal{S}}}_{\mathrm{NIR}} + \hat{\tilde{\mathcal{S}}}_{\mathrm{THz}} = \left(\hat{\alpha}_{\mathrm{NIR}} + \hat{\beta}_{\mathrm{NIR}} + H.c.\right) + \left(\hat{\alpha}_{\mathrm{THz}} + \hat{\beta}_{\mathrm{THz}} + H.c.\right), \tag{5.15}$$

where we have omitted the θ dependence for brevity. Here, the operators $\hat{\alpha}_{\mathrm{NIR}}(\theta)$ and

[1] Note that we assumed that the probe is classical.

$\hat{\alpha}_{\mathrm{THz}}(\theta)$ are defined as

$$\hat{\alpha}_{\mathrm{NIR}}(\theta) = \sqrt{N}P(\theta)\int_0^\infty \mathrm{d}\omega \int_{\Omega_{\max}}^\infty \mathrm{d}\overline{\omega}\; h(\omega)p(\omega,\overline{\omega})\hat{a}_s(\overline{\omega}) \tag{5.16a}$$

$$\hat{\alpha}_{\mathrm{THz}}(\theta) = \sqrt{N}P(\theta)\int_0^\infty \mathrm{d}\omega \int_0^{\Omega_{\max}} \mathrm{d}\Omega\; h(\omega)p(\omega,\Omega)\hat{a}_s(\Omega), \tag{5.16b}$$

where we have used the integration variables $\overline{\omega}$ and Ω to portray the fact that $\hat{\alpha}_{\mathrm{NIR}}(\theta)$ acts on the NIR frequencies $\overline{\omega}$ and $\hat{\alpha}_{\mathrm{THz}}(\theta)$ acts on the THz frequencies Ω. The operators $\hat{\beta}_{\mathrm{NIR}}(\theta)$ and $\hat{\beta}_{\mathrm{THz}}(\theta)$ can be obtained in an equivalent way to Eqs. (5.16a) and (5.16b), respectively. The frequency $\Omega_{\max}$ denotes the boarder between the NIR and THz frequencies and should be chosen with respect to the spectral width of $h(\omega)$ in Eq. (5.4), such that $h(\Omega_{\max}) \ll 1$. We can now calculate the expectation value with respect to the NIR state $|0_{\mathrm{NIR}}\rangle$, which is given by

$$P(\mathcal{S},\theta) = \frac{1}{\sqrt{2\pi[N+\kappa(\theta)]}}\langle\Psi_{\mathrm{THz}}|:\exp\left(-\frac{\left(\mathcal{S}-\hat{\tilde{\mathcal{S}}}_{\mathrm{THz}}(\theta)\right)^2}{2[N+\kappa(\theta)]}\right):|\Psi_{\mathrm{THz}}\rangle. \tag{5.17}$$

We see that the statistics of the electro-optic signal are indeed given by the statistics of the sampled THz field.

The operator inside the expectation value of Equation (5.17) is effectively given by a Gaussian function. The fact that this Gaussian function is normally ordered indeed means that we can treat the operator $\hat{\tilde{\mathcal{S}}}_{\mathrm{THz}}(\theta)$ in its exponent as basically a normal c-number instead of an operator, since annihilators and creators commute within a normally ordered product $:\hat{a}\hat{a}^\dagger:=:\hat{a}^\dagger\hat{a}:=\hat{a}^\dagger\hat{a}$ [118]. We can thus write Eq. (5.17) as a convolution of two probability distributions $P'(\mathcal{S},\theta)$ and $P_{\mathrm{THz}}(\mathcal{S},\theta)$

$$P(\mathcal{S},\theta) = \int_{-\infty}^\infty \mathrm{d}\mathcal{S}' P'(\mathcal{S}-\mathcal{S}',\theta)P_{\mathrm{THz}}(\mathcal{S}',\theta). \tag{5.18}$$

The probability distribution $P'(\mathcal{S},\theta)$ is given by

$$P'(\mathcal{S},\theta) = \frac{1}{\sqrt{2\pi\tilde{\kappa}(\theta)}}\exp\left(-\frac{\mathcal{S}^2}{2\tilde{\kappa}(\theta)}\right), \tag{5.19}$$

where $\tilde{\kappa} = N + 2\left[\hat{\beta}_{\mathrm{NIR}},\hat{\beta}^\dagger_{\mathrm{NIR}}\right] + \left(\left[\hat{\alpha}_{\mathrm{NIR}},\hat{\beta}^\dagger_{\mathrm{NIR}}\right] + H.c.\right) - \left[\hat{\alpha}_{\mathrm{THz}},\hat{\alpha}^\dagger_{\mathrm{THz}}\right] + \left[\hat{\beta}_{\mathrm{THz}},\hat{\beta}^\dagger_{\mathrm{THz}}\right]$.

This means that the probability distribution $P_{\mathrm{THz}}(\mathcal{S},\theta)$ is given by

$$P_{\mathrm{THz}}(\mathcal{S},\theta)=\frac{1}{\sqrt{2\pi\Delta\tilde{\mathcal{S}}^2_{\mathrm{THz}}(\theta)}}\langle\Psi_{\mathrm{THz}}|:\exp\left(-\frac{\left(\mathcal{S}-\hat{\tilde{\mathcal{S}}}_{\mathrm{THz}}(\theta)\right)^2}{2\Delta\tilde{\mathcal{S}}^2_{\mathrm{THz}}(\theta)}\right):|\Psi_{\mathrm{THz}}\rangle, \tag{5.20}$$

where

$$\begin{aligned}\Delta\tilde{\mathcal{S}}^2_{\mathrm{THz}}(\theta)&=\langle 0_{\mathrm{THz}}|\hat{\tilde{\mathcal{S}}}^2_{\mathrm{THz}}(\theta)|0_{\mathrm{THz}}\rangle\\&=\left[\hat{\alpha}_{\mathrm{THz}}(\theta),\hat{\alpha}^\dagger_{\mathrm{THz}}(\theta)\right]+\left[\hat{\beta}_{\mathrm{THz}}(\theta),\hat{\beta}^\dagger_{\mathrm{THz}}(\theta)\right]+\left(\left[\hat{\alpha}_{\mathrm{THz}}(\theta),\hat{\beta}^\dagger_{\mathrm{THz}}(\theta)\right]+H.c.\right)\end{aligned} \tag{5.21}$$

is given by the vacuum fluctuations of the signal $\hat{\tilde{\mathcal{S}}}_{\mathrm{THz}}(\theta)$. Note that $N+\kappa(\theta)=\tilde{\kappa}(\theta)+\Delta\tilde{\mathcal{S}}^2_{\mathrm{THz}}(\theta)$. We want to stress that the deconvolution described here does not rely on any assumption about the THz state $|\Psi_{\mathrm{THz}}\rangle$ other than its initial separability from the NIR state. This deconvolution procedure is therefore also possible for non-Gaussian THz states.

Here, it is apparent that we have chosen $\tilde{\kappa}(\theta)$ such that $P_{\mathrm{THz}}(\mathcal{S},\theta)$ describes the statistics of the operator $\hat{\tilde{\mathcal{S}}}^2_{\mathrm{THz}}(\theta)$, i.e.,

$$\langle\Psi_{\mathrm{THz}}|\hat{\tilde{\mathcal{S}}}^k_{\mathrm{THz}}(\theta)|\Psi_{\mathrm{THz}}\rangle=\int_{-\infty}^{\infty}\mathrm{d}\mathcal{S}\ \mathcal{S}^k P_{\mathrm{THz}}(\mathcal{S},\theta). \tag{5.22}$$

Equation (5.18) together with Eq. (5.19) show that the probability distribution $P_{\mathrm{THz}}(\mathcal{S},\theta)$ can be obtained experimentally by deconvolving the measured probability distribution $P(\mathcal{S},\theta)$ of the electro-optic signal with $P'(\mathcal{S},\theta)$, where $P'(\mathcal{S},\theta)$ has to be calculated theoretically. Note that this deconvolution is possible in this case since $P'(\mathcal{S},\theta)$ is Gaussian. We have thus established that, after the just described post-processing of the measured statistics, electro-optic sampling can be used to obtain the statistics of the THz signal $\hat{\tilde{\mathcal{S}}}_{\mathrm{THz}}(\theta)$. As shown in Eq. (5.15), this THz signal consists of the sum of the two ultrabroadband frequency modes $\alpha(\Omega)$ and $\beta(\Omega)$,

$$\hat{\alpha}_{\mathrm{THz}}(\theta)=\sqrt{N}P(\theta)\int_0^{\Omega_{\max}}\mathrm{d}\Omega\ \alpha(\Omega)\hat{a}_s(\Omega), \tag{5.23a}$$

$$\hat{\beta}_{\mathrm{THz}}(\theta)=\sqrt{N}P^*(\theta)\int_0^{\Omega_{\max}}\mathrm{d}\Omega\ \beta(\Omega)\hat{a}_s(\Omega), \tag{5.23b}$$

with $\alpha(\Omega)=\int_0^\infty\mathrm{d}\omega\ h(\omega)p(\omega,\Omega)$ and $\beta(\Omega)=\int_0^\infty\mathrm{d}\omega\ h^*(\omega)q^*(\omega,\Omega)$. Note that both $\alpha(\Omega)$ and $\beta(\Omega)$ are essentially given by the frequency mode $h(\omega)$, which is shifted down into the THz frequency range through the functions $p(\omega,\Omega)$ and $q^*(\omega,\Omega)$, given by

the Bogoliubov transformation in Eq. (5.6). This results in ultrabroadband frequency modes, whose corresponding temporal modes consist of short (on the order of femtoseconds) few-cycle pulses.

As we can see, the phase shift θ of the wave plate in Fig. 1.2(a) induces a phase shift of $P(\theta)$ for $\hat{\alpha}_{\mathrm{THz}}(\theta)$ and the opposite phase shift $P^*(\theta)$ for $\hat{\beta}_{\mathrm{THz}}(\theta)$. Therefore, the two respective frequency modes cannot simply be combined into a single mode $\alpha(\Omega) + \beta(\Omega)$ since the phase can not be controlled in this case. We rather need to additionally suppress one of the frequency modes such that $\hat{\tilde{\mathcal{S}}}_{\mathrm{THz}}(\theta)$ can be considered to only consist of $\hat{\alpha}_{\mathrm{THz}}(\theta)$ or $\hat{\beta}_{\mathrm{THz}}(\theta)$ alone. This can be achieved by specific spectral filtering functions $\mathcal{F}(\omega)$ in Eq. (5.1) similar to the ones used in chapters 3 and 4.

5.4 Mode selection due to spectral filtering

In the last section, we have shown theoretically how the statistics of ultrashort THz states can be measured using electro-optic sampling. We will now provide an example of such a measurement using the Bogoliubov transformation given in Eq. (2.6) and derived in Appendix A.1 and show how spectral filtering can be used to select a specific mode for $\hat{\tilde{\mathcal{S}}}_{\mathrm{THz}}(\theta)$. This result can be used here since the squeezing process in chapter 2 also relies on the electro-optic effect.

In this case, the broadband modes $\alpha(\Omega)$ and $\beta(\Omega)$ can be expressed as

$$\alpha(\Omega) = \frac{\sqrt{|\Omega|}}{2\pi} \int_{\Omega_{\max}}^{\infty} \mathrm{d}\omega \int_{-\infty}^{\infty} \mathrm{d}t \frac{h(\omega)}{\sqrt{\omega}} e^{i\omega\tau'^{-1}(t) - i\Omega t}, \tag{5.24a}$$

$$\beta(\Omega) = -\frac{\sqrt{|\Omega|}}{2\pi} \int_{\Omega_{\max}}^{\infty} \mathrm{d}\omega \int_{-\infty}^{\infty} \mathrm{d}t \frac{h^*(\omega)}{\sqrt{\omega}} e^{-i\omega\tau'^{-1}(t) - i\Omega t}, \tag{5.24b}$$

where we select $\Omega_{\max}/(2\pi) = 130$ THz. Here, we have used Eq. (2.6) in the retarded reference frame to define $p(\omega, \Omega) = p_{L/2}(\omega, \Omega)$ and $q(\omega, \Omega) = q_{L/2}(\omega, \Omega)$. The corresponding inverse conformal time in the retarded reference frame $\tau'^{-1}(t)$ is given by Eq. (A.4), where we use the probe field in Eq. (A.5) to calculate $\tau'^{-1}(t)$ and assumed a squeezing parameter of $r = 1$.

Here, we will use a Gaussian probe pulse of the form $E_{\mathrm{p},z}(\omega) = iE_0 \exp\left(-\left(\frac{\omega-\omega_c}{\Delta\omega}\right)^2\right)$, with central frequency $\omega_c/(2\pi) = 255$ THz and $\Delta\omega/(2\pi) = 33$ THz, corresponding to a temporal duration at FWHM of $\Delta t = 16$ fs. The corresponding ultrabroadband frequency mode $h(\omega)$ for $\mathcal{F}(\omega) = 1$ [cf. (5.4)] is shown in Fig. 5.1(a). Figure 5.1(b) shows the two commutators $\left[\hat{\alpha}_{\mathrm{THz}}(\theta), \hat{\alpha}^\dagger_{\mathrm{THz}}(\theta)\right]$ and $\left[\hat{\beta}_{\mathrm{THz}}(\theta), \hat{\beta}^\dagger_{\mathrm{THz}}(\theta)\right]$ relative to the shot

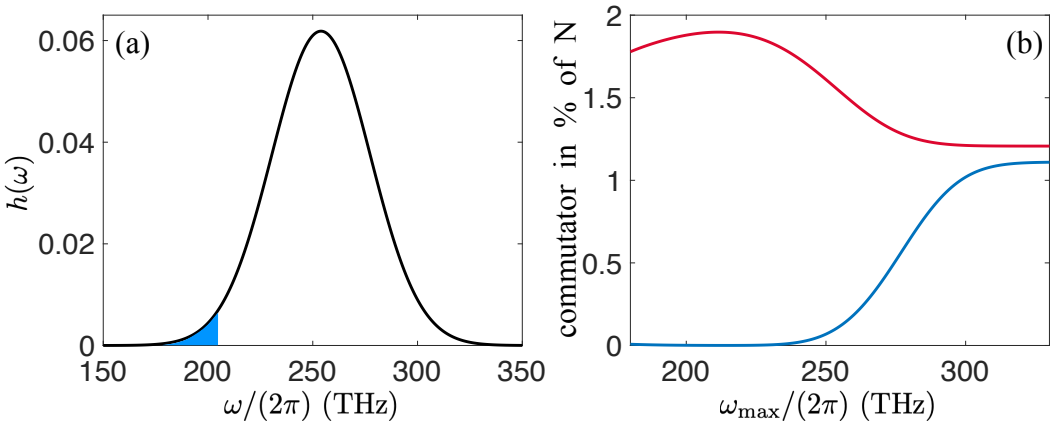

Figure 5.1: Ultrabroadband frequency mode $h(\omega)$ and spectral filtering. (a) The black line shows the unfiltered [$\omega_{\max} \to \infty$ in Eq. (5.25)] ultrabroadband mode $h(\omega)$ given by a Gaussian probe of central frequency $\omega_c/(2\pi) = 255$ THz and a temporal duration at FWHM of $\Delta t = 16$ fs. The blue area shows the part of the unfiltered mode that is selected for $\omega_{\max}/(2\pi) = 212$ THz in Eq. (5.25). In this case, the THz signal $\hat{\tilde{\mathcal{S}}}_{\mathrm{THz}}(\theta)$ is only given by the mode $\beta(\Omega)$ as in Eq. (5.26). (b) The red (blue) line depicts the commutator $\left[\hat{\beta}_{\mathrm{THz}}(\theta), \hat{\beta}^{\dagger}_{\mathrm{THz}}(\theta)\right]/N$ $\left(\left[\hat{\alpha}_{\mathrm{THz}}(\theta), \hat{\alpha}^{\dagger}_{\mathrm{THz}}(\theta)\right]/N\right)$ relative to the shot noise N for different $\omega_{\max}$ in Eq. (5.25).

noise for different spectral filtering functions of the form

$$\mathcal{F}(\omega) = \mathrm{H}(\omega_{\max} - \omega), \tag{5.25}$$

where $\mathrm{H}(\omega)$ is the Heaviside function. Here, only the lower part of the probe spectrum is measured up to a maximal frequency $\omega_{\max}$. As expected, measuring only the lower part of the probe spectrum suppresses the mode $\alpha(\Omega)$ in comparison to $\beta(\Omega)$ since $\alpha(\Omega)$ essentially describes the SFG contribution to the electro-optic process, while $\beta(\Omega)$ describes the DFG contribution. Decreasing $\omega_{\max}$ in Eq. (5.25) decreases both the measured shot noise of the probe N and the vacuum fluctuations $\Delta\tilde{\mathcal{S}}^2_{\mathrm{THz}}(\theta)$ in Eq. (5.21) of $\hat{\tilde{\mathcal{S}}}_{\mathrm{THz}}(\theta)$. As is visible in Figure 5.1(b), there exists an optimum at $\omega_{\max}/(2\pi) \approx 212$ THz for the relative contribution $\left[\hat{\beta}_{\mathrm{THz}}(\theta), \hat{\beta}^{\dagger}_{\mathrm{THz}}(\theta)\right]/N$. The blue area in Fig. 5.1(a) denotes the part of the unfiltered ultrabroadband frequency mode $h(\omega)$ that is measured in this case.

Figure 5.2(a) compares the THz vacuum fluctuations $\Delta\tilde{\mathcal{S}}^2_{\mathrm{THz}}(\theta)$ relative to the shot noise N in case of no spectral filtering ($\omega_{\max} \to \infty$) and according to the optimal spectral filtering $\omega_{\max}/(2\pi) = 212$ THz. With no spectral filtering applied, $\hat{\tilde{\mathcal{S}}}_{\mathrm{THz}}(\theta)$ depends on the phase shift θ because of the interference term $\left(\left[\hat{\alpha}_{\mathrm{THz}}(\theta), \hat{\beta}^{\dagger}_{\mathrm{THz}}(\theta)\right] + H.c.\right)$ between the two modes in Eq. (5.21). At the optimal spectral filtering, the mode $\alpha(\Omega)$ can

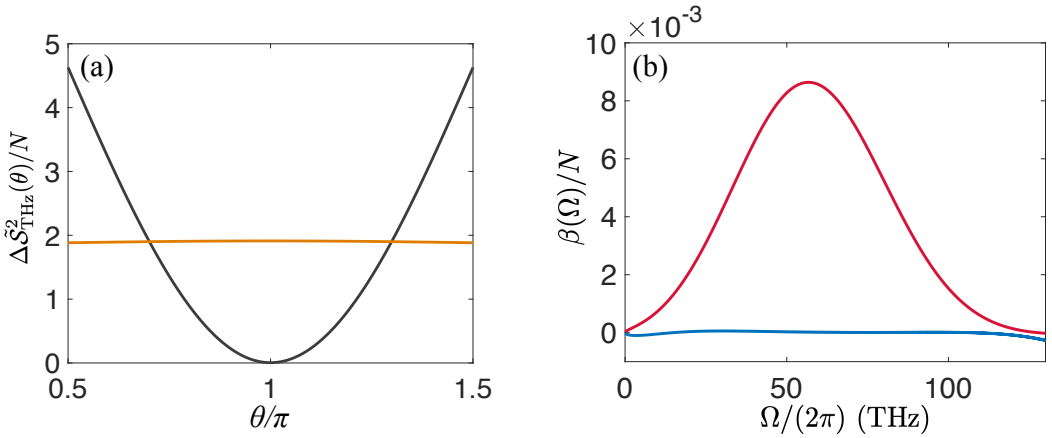

Figure 5.2: Vaccum fluctuations and frequency mode profiles. (a) The black [orange] line depicts the phase dependence of $\Delta\tilde{\mathcal{S}}^2_{\mathrm{THz}}(\theta)$ for $\omega_{\mathrm{max}} \to \infty$ [$\omega_{\mathrm{max}}/(2\pi) = 212$ THz]. (b) The red (blue) line shows the frequency mode $\beta(\Omega)$ [$\alpha(\Omega)$] for the optimal spectral filtering.

be neglected and the vacuum fluctuations become phase independent as they should be. The frequency modes $\alpha(\Omega)$ and $\beta(\Omega)$ for the optimal spectral filtering are shown in Fig. 5.2(b). The mode $\alpha(\Omega)$ is strongly suppressed in comparison to $\beta(\Omega)$. Therefore, the signal $\hat{\tilde{\mathcal{S}}}_{\mathrm{THz}}(\theta)$ is essentially given by

$$\hat{\tilde{\mathcal{S}}}_{\mathrm{THz}}(\theta) \approx \hat{\beta}_{\mathrm{THz}}(\theta) + \hat{\beta}^{\dagger}_{\mathrm{THz}}(\theta) \tag{5.26}$$

and the phase shift of this signal can be controlled by θ. Figure 5.2(b) also shows that the mode $\beta(\Omega)$ constitutes an extremely broadband mode with a central frequency of 57 THz and a FWHM of 54 THz.

5.5 Sampling of ultrashort pulsed Schrödinger cat states

Equation (5.26) together with Fig. 5.2(b) shows that the spectral filtering allows us to select a single ultrabroadband mode in the THz frequency range, whose phase shift can be controlled via the wave plate in Fig. 3.1(a). We now give an example of this technique in form of the measurement of an even ultrashort pulsed Schrödinger cat state of the form

$$|\Psi_{\mathrm{THz}}\rangle = |\mathrm{cat}_+\rangle = \frac{1}{\sqrt{\mathcal{N}}}\left(\left|\{\gamma(\Omega)\}\right\rangle + \left|-\{\gamma(\Omega)\}\right\rangle\right), \tag{5.27}$$

where $\left|\{\gamma(\Omega)\}\right\rangle$ denotes a broadband coherent state $\hat{a}(\Omega)\left|\{\gamma(\Omega)\}\right\rangle = \gamma(\Omega)\left|\{\gamma(\Omega)\}\right\rangle$ and $\mathcal{N} = \frac{1}{\sqrt{2\left(1+\exp\left(-2\int_0^\infty \mathrm{d}\Omega|\gamma(\Omega)|^2\right)\right)}}$ is normalization factor.

The corresponding reconstructed THz probability distribution in Eq. (5.20) for the mode-selected signal in Eq. (5.26) is given by

$$\begin{aligned} P_{\mathrm{THz}}(\mathcal{S},\theta) = \frac{2\mathcal{N}^2}{\sqrt{2\pi\Delta\tilde{\mathcal{S}}^2_{\mathrm{THz}}}} \exp\left(-\frac{\mathcal{S}^2}{2\Delta\tilde{\mathcal{S}}^2_{\mathrm{THz}}}\right) \\ \times\left[\cosh\left(\frac{2\mathcal{S}\Re\left\{\gamma^{(d)}(t,\theta)\right\}}{\Delta\tilde{\mathcal{S}}^2_{\mathrm{THz}}}\right)\exp\left(-\frac{2\Re\left\{\gamma^{(d)}(t,\theta)\right\}^2}{\Delta\tilde{\mathcal{S}}^2_{\mathrm{THz}}}\right)\right. \\ \left.+\exp\left(-2\int_0^\infty \mathrm{d}\Omega|\gamma(\Omega)|^2\right)\cos\left(\frac{4\mathcal{S}\Im\left\{\gamma^{(d)}(t,\theta)\right\}}{\Delta\tilde{\mathcal{S}}^2_{\mathrm{THz}}}\right)\exp\left(\frac{2\Im\left\{\gamma^{(d)}(t,\theta)\right\}^2}{\Delta\tilde{\mathcal{S}}^2_{\mathrm{THz}}}\right)\right], \end{aligned} \tag{5.28}$$

where $\gamma^{(d)}(t) = \left\langle\{\gamma(\Omega)\}\right|\hat{\beta}_{\mathrm{THz}}(\theta)\left|\{\gamma(\Omega)\}\right\rangle = \int_0^\infty \mathrm{d}\Omega\ \gamma(\Omega)\beta(\Omega)e^{-i\Omega t}$ is the overlap between the frequency mode of the cat state $\gamma(\Omega)$ and $\beta(\Omega)$. Note that we also accounted for delay times t between the probe and the THz cat state so that the temporal evolution of the pulsed cat state can be measured.

The first term in the rectangular bracket of Eq. (5.28) splits the initial Gaussian state of the vacuum at $t \to -\infty$ into two Gaussians with opposite mean values $\pm 2\Re\left\{\gamma^{(d)}(t,\theta)\right\}$. This term is also obtained if a statistical mixture between the two coherent states of opposite signs is considered. The second term describes the interference between the two coherent states and results from the negativities in the corresponding Wigner function of this state. The interference term is attenuated by the factor $\exp\left(-2\int_0^\infty \mathrm{d}\Omega|\gamma(\Omega)|^2 + \frac{2\Im\left\{\gamma^{(d)}(t,\theta)\right\}^2}{\Delta\tilde{\mathcal{S}}^2_{\mathrm{THz}}}\right)$ where the first term in the exponent essentially describes the overlap between the two coherent amplitudes $\pm\gamma(\Omega)$ of opposite sign of the cat state and the second term describes the overlap between the frequency mode of the cat state $\gamma(\Omega)$ and $\beta(\Omega)$ divided by the vacuum fluctuations $\Delta\tilde{\mathcal{S}}^2_{\mathrm{THz}}$ of $\hat{\beta}_{\mathrm{Thz}}(\theta)$. We thus see that a mismatch between these two overlaps restricts the maximal amplitude of the cat state, at which the interference pattern can still be resolved. In order to observe them, it is therefore generally necessary to match the mode of $\beta(\Omega)$ to $\gamma(\Omega)$, as is also the case in balanced homodyning with temporal modes [48, 113].

Equations (5.20) and (5.26) show that the entire probability distribution of the mode $\beta(\Omega)$ over the interval $\pi/2 < \theta < 3\pi/2$ can be sampled. Since the phase shift spans over an interval of length π, the corresponding Wigner function $W(\delta)$ of the probability distribution can be calculated by performing an inverse Radon transform

[10, 48, 110] on the sampled probability distribution,

$$W(\delta) = \frac{1}{\pi^2}\int_{-\pi/2}^{\pi/2}\mathrm{d}\varphi\int_{-\infty}^{\infty}\mathrm{d}y\int_{-\infty}^{\infty}\mathrm{d}\mathcal{S}\; P_{\mathrm{THz}}(\mathcal{S},\theta(\varphi)) \times |y|\exp\left(iy\left[x - 2\Re\{\delta\}\cos(\varphi) + 2\Im\{\delta\}\sin(\varphi)\right]\right). \tag{5.29}$$

Note that we replaced θ by the function $\theta(\varphi) = 2\arccos\left(\sin(\varphi)/\sqrt{2}\right)$ in $P_{\mathrm{THz}}(\mathcal{S},\theta)$, so that $P(\theta(\varphi)) = e^{i\varphi}$ and φ corresponds to the actual phase shift induced in $\hat{\tilde{\mathcal{S}}}_{\mathrm{THz}}(\theta)$ in Eq. (5.26).

The Wigner function obtained in this way for the cat state in Eqs. (5.27) and (5.28) for different delay times t between the probe and the cat state is shown in Fig. 5.3. Here, we assumed perfect mode matching between the cat state and $\beta(\Omega)$,

$$\gamma(\Omega) = \gamma_0\beta(\Omega), \tag{5.30}$$

with $\gamma_0 = \sqrt{\frac{6}{\int_0^{\Omega_{\max}}\mathrm{d}\Omega|\beta(\Omega)|^2}}$, which corresponds to a mean photon number of 6 photons in the cat state. Figure 5.3(a) shows that the temporal mode $\gamma(t)$ of the cat state (blue line) is similar to the sampled temporal mode $\gamma^{(d)}(t)$ in Eq. (5.28) (red line), but possesses a slightly shorter temporal envelope. This is a result of the mode matching condition which needs to be fulfilled in order to resolve the negativities in the Wigner function. This means that the probe pulse (black line) needs to possess a similar temporal duration as the mode of the sampled THz state. As a result, the temporal dynamics of the sampled state cannot be resolved perfectly. The temporal evolution of the Wigner function is shown in Figs. 5.3(b)-(f). The time points cover one cycle of $\gamma^{(d)}(t)$ and are chosen to coincide with its maxima/minima and roots. The Wigner function shows two barely separated Gaussians at t_1 and just within one cycle (after $t_5 - t_1 \approx 16$ fs) evolves to their maximal separation with a clearly visible interference pattern in the middle at t_5.

5.6 Conclusion

Here, we have shown that the statistics of arbitrary THz input fields can be reconstructed from the statistics of the measured electro-optic signal. The spectral width of the measured THz frequency mode is essentially given by the width of the probe field. This results in an ultrabroadband frequency mode corresponding to ultrashort few-cycle temporal modes on the order of femtoseconds.

In order to reconstruct the statistics of the THz field, the probability distribution of the electro-optic signal has to be deconvolved with a Gaussian function whose vari-

ance is essentially given by the shot noise and small additional corrections due to the electro-optic process. Therefore, a precise theoretical model of the electro-optic process, fitted to the experimental parameters, needs to be present to ensure a successful reconstruction. We note that the deconvolution process is independent on the THz state and only a precise model of the electro-optic process for the vacuum input in both the s-polarized NIR and THz frequencies is needed. Furthermore, we have shown that in case of a crystal with an isotropic refractive index, the equal contribution of SFG and DFG processes leads to the presence of two different frequency modes in the THz signal, whose phases are rotated in opposite directions when changing the phase of the waveplate in the ellipsometry. We have shown that one of the modes can be suppressed by spectral filtering in the NIR photon detectors so that the phase of the THz signal can be controlled by the phase of the waveplate. Alternatively, birefringent crystals such as gallium selenide (GaSe), silver gallium sulfide ($AgGaS_2$), or β-barium borate (BBO) [47, 102] could be employed. Here, either the DFG or the SFG process can be suppressed due to unfavorable phase matching, so that spectral filtering might not be necessary.

As an example, we have shown the tomography of a femtosecond, few-cycle THz cat state. Here, we saw that mode matching between the THz state and the sampled mode is necessary in order to resolve the negativities of the Wigner function. This means that there exists a trade-off between the resolution of the temporal characteristics of the sampled THz state and the resolution of its negativities in the Wigner function. Further research needs to be done in order to see how additional orthogonal modes can be created, since the THz modes can only be controlled indirectly over the probe pulse shape and the spectral filtering.

In order to describe the electro-optic process, we have used the Bogoliubov transformation derived in chapter 2. This solution provides a very simplified model, since it ignores phase matching, the off axis propagation directions at very low THz frequencies, and time-ordering effects discussed in chapter 4. The effective Hamiltonian and quantization of the THz field derived in chapter 4 can be used in the future to obtain a more precise model for the electro-optic process by calculating the Bogoliubov transformation perturbatively.

Lastly, we note that, as long as the initial states of the s-polarized NIR and THz fields are separable, the probability distribution of the electro-optic signal can always be written as a convolution of two probability distributions as in Eq. (5.18). Whether a deconvolution is possible to obtain the THz statistics then only depends on the actual form of the probability distribution of the NIR state. More precisely, a deconvolution is always possible as long as the initial s-polarized NIR and THz states are separable

and the Fourier transform of the NIR state does not posses any roots inside the spectral range of the Fourier transform of the THz probability distribution. Recently, the employment of photon-number entangled twin beams was suggested in order to obtain conditioned non-classical probes for quantum electro-optic sampling. These Fock-state probes were shown to increase the signal-to-noise ratio of the electro-optic signal [119]. A reconstruction of the THz probability distribution might also be possible in this case. Another obvious possibility is given by the employment of squeezed s-polarized NIR vacuum fields in quantum electro-optic sampling in order to increase the signal-to-noise ratio. Of course, this would only be possible for a specific phase shift, so that the orthogonal quadrature would exhibit noise above the shot noise limit. Changing the angle of squeezing according to the induced phase shift could circumvent this problem. In this case, interesting questions about the uncertainty relations of the measured quadratures and their information content about the THz state arise.

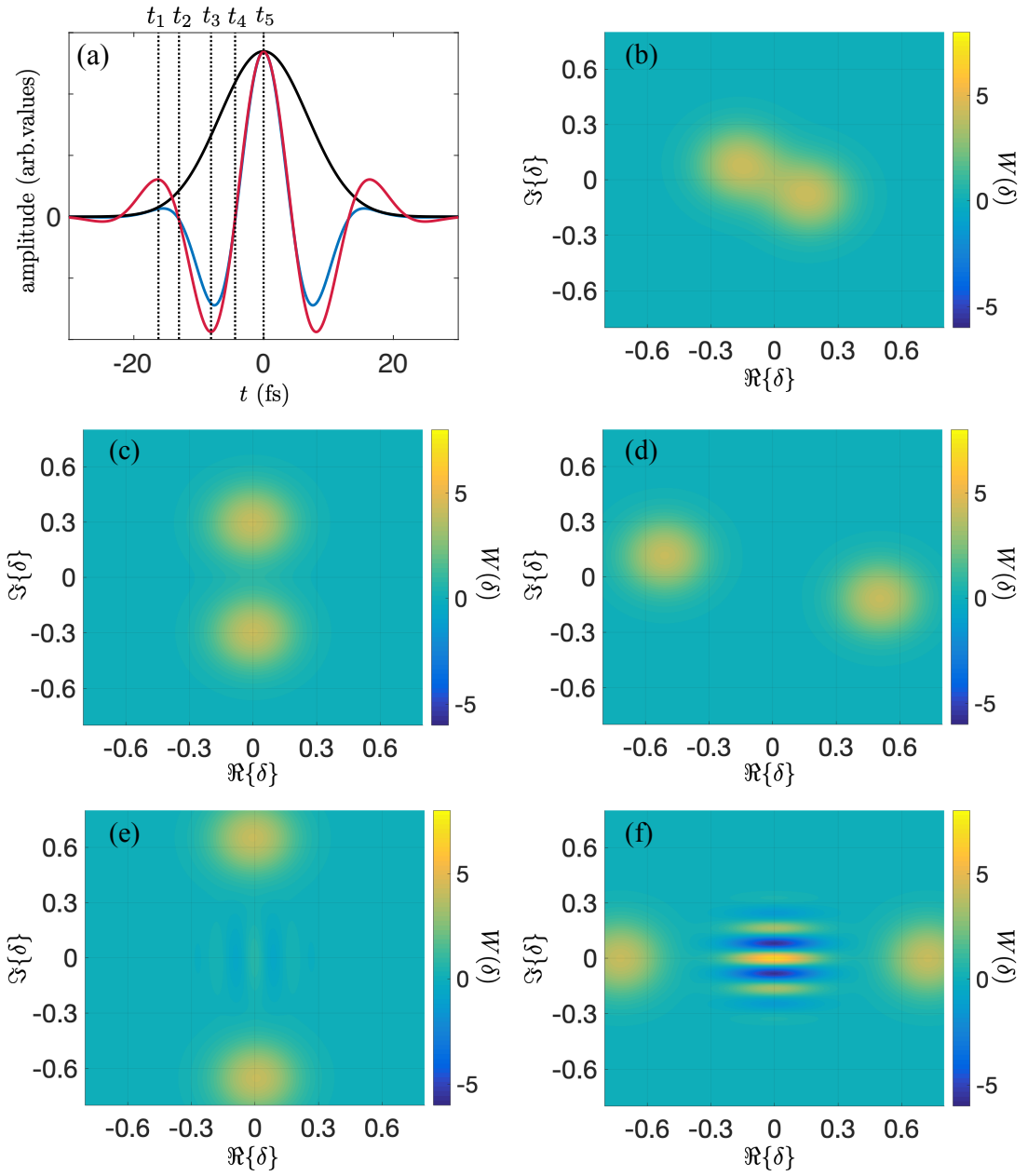

Figure 5.3: Wigner function of an ultrashort pulsed cat state. (a) The black line shows the envelope of the probe pulse. The blue line shows the temporal mode of the cat state, given by the Fourier transform of $\gamma(\Omega) = \gamma_0\beta(\Omega)$, $\gamma(t) = \gamma_0 \int_0^\infty \mathrm{d}\Omega\ \Re\left\{\beta(\Omega)e^{i\Omega t}\right\}$. The red line shows the overlap $\gamma^{(d)}(t) = \int_0^\infty \mathrm{d}\Omega\ \gamma(\Omega)\beta(\Omega)e^{-i\Omega t}$ between $\beta(\Omega)$ and $\gamma(\Omega)$ for different delay times t. The vertical dashed lines show the time points at which the Wigner function is shown in (b)-(f). The time points are chosen at maxima/minima or roots of $\gamma^{(d)}(t)$. The values on the y-axis are arbitrary since the amplitudes of the respective functions at $t = 0$ are chosen to coincide to give a comparison of the shape of the different temporal modes. (b)-(f) Wigner functions at time points $t_1 - t_5$, respectively.

Chapter 6

Conclusion

Quantum electro-optic sampling is a promising technique for the study of ultrafast quantum electric fields. This thesis summarizes my efforts in extending the theoretical background of this novel technique and its possible applications for the generation and study of ultrashort quantum fields. Below, we give a short summary of the conclusions of the main chapters of this thesis, more detailed conclusions can be found at the end of each chapter.

In chapter 2, we describe the generation of ultrashort squeezed states of light by means of the electro-optic process. A classical drive induces effective local accelerations of the incoming vacuum field, which results in a change in the flow of time the vacuum field is experiencing. Connections to gravitational effects are drawn by using the induced time-dependent dispersion relation of the field to extract an effective curved metric inside the crystal. For higher driving strengths, distinct asymmetries between the squeezing and anti-squeezing can be observed. The squeezing intervals are characterized by long and flat valleys, while the anti-squeezing intervals are given by strong and narrow peaks.

In chapter 3, we develop a microscopic theory of electro-optic sampling of THz vacuum fluctuations, where we employ a superoperator formalism to incorporate the quantum nature of both the fields and matter at the same level. Here, the electro-optic medium is modelled as an ensemble of noninteracting three-level systems. We separate the electro-optic response into a classical part, representing the quantum analogue to the sampling of classical fields, and a quantum part, whose contribution is independent on the state of the sampled field. The quantum part is further separated into a cascading contribution and a genuine quantum contribution stemming from so-called noncausal susceptibilities. The cascading contribution can also be obtained within an effective Hamiltonian framework describing the electro-optic process. In contrast, the quantum contribution only arises from a detailed description of the interaction between the

fields and matter, so that no effective theory describing the field degrees of freedom alone can be formulated. Lastly, we show that the ellipsometry also allows for the measurement of arbitrary quadratures of the generated electro-optic signal. We find that each of the three contributions described above are dominating at different phase shifts of the electro-optic signal. We describe how the statistics of the THz vacuum field can be reconstructed and note that this reconstruction needs to take into account the cascading and quantum contributions.

In chapter 4 we provide an effective Hamiltonian of the electro-optic process and go beyond the paraxial description of the THz field in order to describe the diffraction losses at lower frequencies. Furthermore, we discuss how phase matching changes the qualitative behaviour of the time-ordering effects in the cascading contributions derived in chapter 3.

Lastly, chapter 5 shows that a reconstruction of the THz statistics for arbitrary THz states is possible even in the presence of additional cascading contributions described in the previous two chapters. The electro-optic process together with the NIR probe select an ultrashort few-cycle temporal mode of the THz state. Spectral filtering can be used to control the SFG and DFG contributions to this mode and one of these two processes needs to be suppressed strongly in order to be able to control the phase of the few cycle THz mode with the waveplate. An example of such a detection is given through the electro-optic sampling of a few-cycle cat state. We demonstrate that a trade-off exists between the temporal resolution of the dynamics of the state and the resolution of negativities inside the Wigner function, since increased time resolution inherently leads to the admixture of excess noise.

Appendix A

Appendix

A.1 Method of characteristics

The method of characteristics is used to solve a given partial differential equation (PDE) by reducing it to a set of ordinary differential equations (ODEs), which define parametric curves in the space of the PDE variables (so-called characteristic curves). These curves allow then to construct the solution of the PDE. Let us assume that the original variables of the PDE, in our case Eq. (2.2), depend on the parameter ζ. Comparison of the total derivative of $\hat{\varepsilon}$ with respect to ζ with Eq. (2.2) gives us ODEs for $z(\zeta)$ and $t(\zeta)$ (with their respective initial conditions):

$$\frac{\mathrm{d}z}{\mathrm{d}\zeta} = 1, \qquad z(\zeta = 0) = -l/2; \tag{A.1}$$

$$\frac{\mathrm{d}t}{\mathrm{d}\zeta} = -\frac{d}{nc}\left[\mathcal{E}(z,t) - \frac{n^2}{d}\right]_{z=z(\zeta),t=t(\zeta)}, \qquad t(\zeta = 0) = \tau. \tag{A.2}$$

Here an additional parameter τ was introduced as the initial condition for $t(\zeta)$ when $\zeta = 0$. Solving Eq. (A.1) reveals that $\zeta = z + l/2$. Changing the variable from ζ to z in Eq. (A.2) and solving it, we obtain $t(z, \tau)$, where now also an explicit dependence on τ appears. Finally, the function $t(z, \tau)$ can be inverted to obtain $\tau(z, t)$ with $\tau(z = -l/2, t) = t$. The functional form of $\tau(z, t)$ ensures that the total derivative of $\tau(z(\zeta), t(\zeta))$ with respect to ζ vanishes,

$$\frac{\mathrm{d}\tau(z(\zeta), t(\zeta))}{\mathrm{d}\zeta} = \frac{\partial\tau(z,t)}{\partial z} - \frac{d}{nc_0}\left[\mathcal{E}(z,t) - \frac{n^2}{d}\right]\frac{\partial\tau(z,t)}{\partial t} = 0, \tag{A.3}$$

meaning that $\tau(z(\zeta), t(\zeta))$ remains constant when moving along a characteristic curve $\{z(\zeta), t(\zeta)\}$ parameterized by ζ. This PDE for $\tau(z, t)$ can now be used to prove that Eq. (2.5) indeed satisfies Eq. (2.2). Therefore, the only remaining nontrivial task is to

solve Eq. (A.2) finding $\tau(z,t)$. Inserting the solution for $\tau(z,t)$ into Eq. (2.5) then gives $\hat{\varepsilon}(z,t)$.

For the purpose of solving Eq. (A.2) the retarded reference frame with $t' = t - \frac{n}{c_0}z$, $z' = z$ and $\mathcal{E}(z,t) = \mathcal{E}'(t')$ is utilized. This transforms Eq. (A.2) into a separable ODE. $\tau(z,t)$ can then be expressed as

$$\tau(z,t) = f^{-1}\left(f\Big(t - \frac{n}{c_0}z\Big) + \frac{1}{nc_0}\Big(z + \frac{l}{2}\Big)\right) - \frac{nl}{2c_0} \tag{A.4}$$

in the original reference frame, where $f(t')$ is defined as solution of the following ODE

$$\frac{\mathrm{d}f(t')}{\mathrm{d}t'} = \frac{1}{d\mathcal{E}'(t')}. \tag{A.5}$$

Note that for Eq. (A.5) no initial condition needs to be stated because it can be chosen arbitrarily. The necessary initial condition is already incorporated in the solution for $\tau(z,t)$ with $\tau(z = -l/2, t) = t$, regardless of the specific form of $f(t')$.

A.2 Slowly varying amplitude approximation and causality

Equation (2.5) shows that the quantum field at the exit of the crystal at time t is influenced by the quantum field at the entrance at time $\tau_{\mathrm{out}}(t)$. This fact raises the question whether in our calculations this can technically lead to an information exchange faster than the speed of light or even the conformal time preceding the lab time. Already the first case would contradict causality. Figure 2.2(b) shows $\tau_{\mathrm{out}}(t)$ as a function of t (full black line). Without the driving field, $\tau_{\mathrm{out}}(t)$ is delayed with respect to t by the time nl/c_0 which the light needs to travel through the crystal (see dashed black line). The red-coloured area in the figure marks the region for $\tau_{\mathrm{out}}(t)$ where the delay between $\tau_{\mathrm{out}}(t)$ and t is less than l/c_0, which is the time required for light to travel the distance l in vacuum. Due to causality, the information about the incoming quantum field cannot propagate to the end of the crystal in a time shorter than l/c_0. Causality forbids this area for $\tau_{\mathrm{out}}(t)$. Since its deviation from the lab time t grows with higher squeezing strengths r, the restriction that $\tau_{\mathrm{out}}(t) - t + nl/c_0$ (vertical difference between the full red and dashed black line in Fig. 2.2(b) should not exceed $(n-1)l/c_0$ ultimately puts an upper bound to the maximally allowed r. However, the use of a broadband version of the SVAA, underlying our theoretical approach, imposes an even stricter upper bound to the squeezing strength that then already ensures causality, as we will show in the following. Within the utilized broadband SVAA we neglected $\frac{\partial^2 \hat{\varepsilon}(z;\Omega)}{\partial z^2}$ with

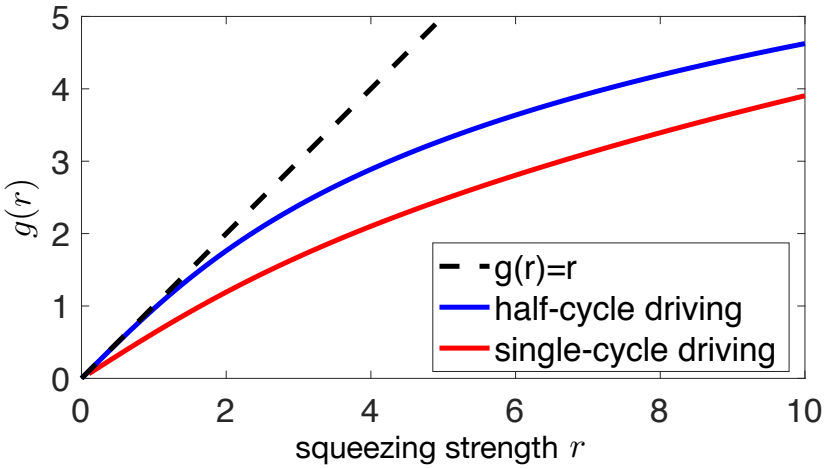

Figure A.1: Function $g(r)$ for the half-cycle (blue line) and single-cycle (red line) driving. For $r \ll 1$, $g(r)$ approximately equals r ($0.64r$) in the case of half-cycle (single-cycle) driving. For higher squeezing strengths, $g(r)$ grows more slowly with r.

respect to $k_\Omega \frac{\partial \hat{\varepsilon}(z;\Omega)}{\partial z}$. This is possible only if $\hat{\varepsilon}(z;\Omega)$ does not change too rapidly with z. The corresponding condition limiting the strength of the coherent field, which induces variations of $\hat{\varepsilon}(z;\Omega)$, can be found from Eq. (2.1) differentiating it with respect to z. Assuming that the driving field has a peak amplitude $\mathcal{E}_0$, we obtain $\mathcal{E}_0 d \ll n^2$. With the frequencies of the ultrabroadband driving field being on the order of Γ_0 this restriction can be reformulated as a condition on the squeezing strength r,

$$r \ll \frac{n\Gamma_0 l}{c_0}. \tag{A.6}$$

Solutions obtained within the broadband SVAA do not automatically preserve causality, i.e. the impossibility of information exchange faster than the speed of light. The condition

$$g(r) := \Gamma_0 \max_{t'} \left[\tau'(z' = l/2, t') - t'\right] \leq \frac{\Gamma_0 (n-1) l}{c_0}, \tag{A.7}$$

formulated in the retarded reference frame, ensures causality. This also effectively sets a boundary for r. For $r \ll 1$, the left hand side of the expression above is proportional to r with a proportionality factor given by $\max \mathcal{E}'(t')/\mathcal{E}_0 \lesssim 1$. For higher r, the increase becomes even slower [see Fig. A.1]. Since for nonlinear crystals typically n and $n-1$ are on the same order, the limit imposed by the range of validity of the broadband SVAA, Eq. (A.6), already ensures causality. This means that it is sufficient to respect Eq. (A.6). For squeezing strengths beyond the SVAA the changes in the refractive index induced by the driving field would be comparable to the initial refractive index n

of the crystal. Furthermore, effects of higher order nonlinearities like $\chi^{(3)}$ would need to be taken into account.

Considering an experimentally realistic situation with $\Gamma_0/(2\pi) = 26$ THz and a $l = 15$ μm thick ZnTe crystal with $n = 2.57$, Eq. (A.6) leads to an estimation

$$r \ll 20. \tag{A.8}$$

In comparison, the limit given by causality in this case can be calculated to

$$g(r) \leq 13. \tag{A.9}$$

In this work the refractive index of the nonlinear crystal is treated as a dispersionless constant. In doing so we neglect the phonon resonances, located for ZnTe at around 5 THz, and assume that the main contributions to the signal will be given by higher frequencies. In principle, from Eq. (A.6) we see that higher values of r become possible if the crystal thickness is increased. This possibility is, however, limited by the requirement to fulfill the ultrabroadband phase matching conditions. Overcoming this issue would open a way for ultrabroadband squeezing in the high gain regime.

A.3 Conformal map and conformal time

Considering a flat '1+1'-Minkowski metric with coordinates $x'^{\mu} = (c_0 T, Z)$ and interval

$$\mathrm{d}s'^2 = c_0^2 \mathrm{d}T^2 - \mathrm{d}Z^2, \tag{A.10}$$

we find the following conformal mapping connecting this flat metric to the space-time expressed in terms of the lab coordinates $x^{\mu} = (c_0 t, z)$:

$$T(z,t) = \frac{1}{2}\Big(\tau_{\mathrm{out}}\left[t + (z - l/2)/c_0\right] + \tau_{\mathrm{out}}\left[t - (z - l/2)/c_0\right]\Big), \tag{A.11}$$

$$Z(z,t) = \frac{c_0}{2}\Big(\tau_{\mathrm{out}}\left[t + (z - l/2)/c_0\right] - \tau_{\mathrm{out}}\left[t - (z - l/2)/c_0\right]\Big). \tag{A.12}$$

Here $\tau_{\mathrm{out}}(t) = \tau(z = l/2, t)$ and $\tau(z,t)$ is determined explicitly by Eq. (A.4). Indeed, expressed in terms of x^{μ} the interval in Eq. (A.10) takes the form

$$\mathrm{d}s'^2 = \frac{1}{\Omega^2(z,t)}\left(c_0^2 \mathrm{d}t^2 - \mathrm{d}z^2\right) = \frac{1}{\Omega^2(z,t)}\mathrm{d}s^2_{\mathrm{flat}}. \tag{A.13}$$

Therefore, the metric in Eq. (A.10) appears curved in the lab coordinates x^{μ} but is conformally equivalent to the Minkowski metric. The function $\Omega(z,t)$ is called *conformal*

factor and is given here by

$$\Omega(z,t) = \frac{1}{\sqrt{\dot{\tau}_{\text{out}}\left[t + (z - l/2)/c_0\right] \dot{\tau}_{\text{out}}\left[t - (z - l/2)/c_0\right]}}\,, \tag{A.14}$$

where $\dot{\tau}_{\text{out}}(t) \equiv \frac{\mathrm{d}}{\mathrm{d}t}\tau_{\text{out}}(t)$. Specifically at $z = l/2$ we have

$$\mathrm{d}z = \mathrm{d}Z = 0\,, \tag{A.15}$$

$$\mathrm{d}T = \frac{\mathrm{d}t}{\Omega(z = l/2, t)}\,. \tag{A.16}$$

For $z \neq l/2$, Eq. (A.15) does not hold anymore ($\mathrm{d}Z \neq 0$) and the relation between T and t is not determined directly via the conformal factor $\Omega(z,t)$ alone. The relation between $T(z = l/2, t) = \tau_{\text{out}}(t)$ and t through Eq. (A.16) is analogous to the definition of the so-called conformal time η with respect to the Friedmann-Robertson-Walker metric in general relativity ($\mathrm{d}\eta = \frac{\mathrm{d}t}{a(t)}$ where $a(t)$ is the conformal factor describing the expansion of the universe) [90]. Figure A.2 visualizes the curved space-time that arises when the geodesics of the flat metric with respect to x^μ are expressed in the conformally equivalent coordinates x'^μ. The conformal mapping preserves the angles

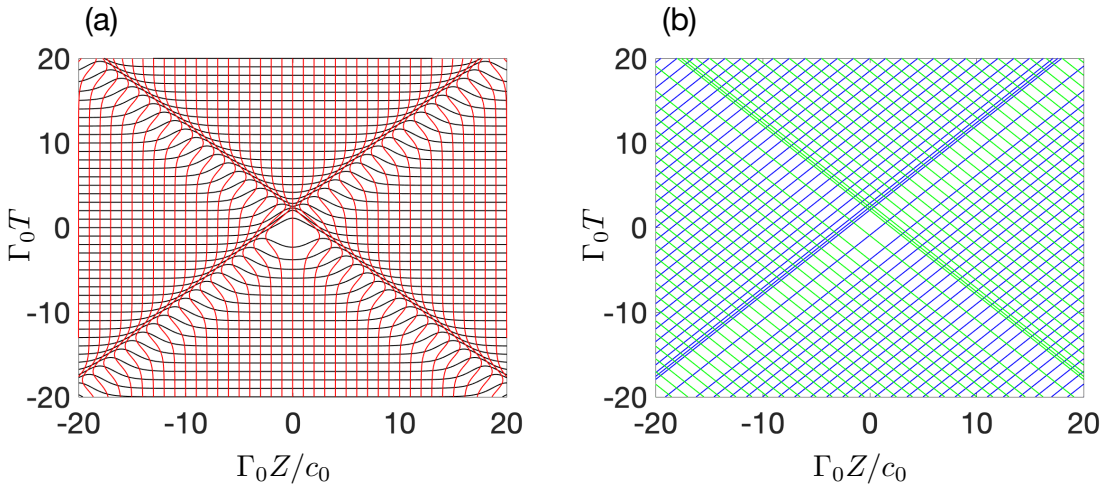

Figure A.2: Visualization of the conformal mapping. (a) Lines of constant time $\mathrm{d}t = 0$ (black) and constant position, $\mathrm{d}z = 0$, (red lines) in the space of coordinates T and Z. (b) Light cones $\mathrm{d}(t - z/c_0) = 0$ (blue lines) and $\mathrm{d}(t + z/c_0) = 0$ (green lines) in the space of coordinates T and Z. The conformal map preserves the angles of the light cones at each space-time point.

of the light cones and only changes the parametrization when propagating along them,

$$T - Z/c_0 = \tau_{\text{out}}\left[t - (z - l/2)/c_0\right], \tag{A.17}$$

$$T + Z/c_0 = \tau_{\text{out}}\left[t + (z - l/2)/c_0\right]. \tag{A.18}$$

The parametrization along the light cones is therefore given by the conformal time $\tau_{\text{out}}(t)$ phase-shifted by $\pm(z - l/2)/c_0$.

In the consideration above we have introduced the conformal mapping and the corresponding conformal time $\tau_{\text{out}}(t)$ resulting upon the light propagation through the whole generation crystal. It is possible to extend these concepts also for the evolution taking place inside of the crystal. In this case, $\tau(z,t)$ can be introduced at any point z as the local conformal time that arises from the corresponding conformal mapping assuming that the crystal ends at z. Afterwards the shape of $\tau(z,t)$ [cf. black lines on the surface in Fig. 2.2(a)] is not evolving any more but just moving along the light cone $t - (z - l/2)/c_0$. The respective inverse conformal factor is given by $\frac{\partial}{\partial t}\tau(z,t)$.

A.4 Half-cycle pulse

The shape of the half-cycle pulse $\mathcal{E}'(t') = \mathcal{E}_0 \operatorname{sech}(\Gamma_0 t')$ used as the driving field in Fig. 2.3 is depicted in Fig. B.1 as the black line. Because of its non-vanishing integral over time, these type of pulses are actually not supported in the far-field region with respect to the light source. However, for our particular problem the selected temporal profile can serve as a good model of a waveform capable to propagate in the far-field zone, which is relevant to the experimental situation. Let us consider the following allowed pulse shape (red line in Fig. B.1)

$$\mathcal{E}'_{\text{r}}(t') = \mathcal{E}_0 \operatorname{sech}(\Gamma_0 t') - 0.1\mathcal{E}_0 \operatorname{sech}\left(\frac{\Gamma_0 t'}{10}\right). \tag{A.19}$$

The correction introduced by the second term forces the integral over time to vanish. In principle, one might want to use such or similar shapes for our calculations directly in place of a simpler profile $\mathcal{E}'(t')$. However, the latter has the advantage that the solution for the evolution of the conformal time inside the crystal could be found in an analytical form also for stronger driving fields. Compared with $\mathcal{E}'(t')$, the field $\mathcal{E}'_{\text{r}}(t')$ has a somewhat lower central positive peak and possesses negative side wings, which are low-amplitude and extended in time . An important point is that the difference between both discussed waveforms remains small for any moment in time. Furthermore, in the calculations of the detected variance the difference is even less than it could be anticipated looking at Fig. B.1. Indeed, let us consider for example the case of

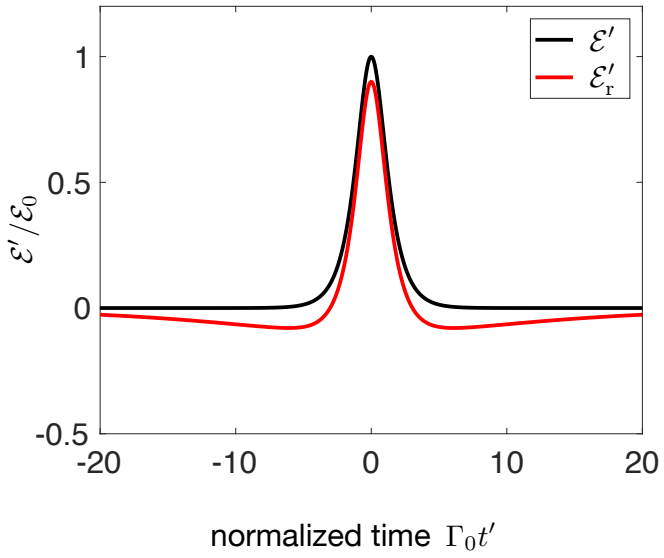

Figure A.3: Comparison between the half-cycle pulse (black) used for the calculations depicted in Fig. 2.3 and the more realistic propagating pulse (red) that it approximates. The two side wings of the red curve compensate the big maximum in the center but are still small compared to the maximum.

the vanishing probe pulse duration t_{p} and weak driving when the dynamics of the detected variance is governed by $\mathrm{d}^3\mathcal{E}'(t_{\mathrm{d}})/\mathrm{d}t_{\mathrm{d}}^3$ or $\mathrm{d}^3\mathcal{E}'_{\mathrm{r}}(t_{\mathrm{d}})/\mathrm{d}t_{\mathrm{d}}^3$, respectively. In the third derivative the contribution of the second term on the right hand side of Eq. (A.19) is suppressed by an additional factor of 10^3 with respect to the first term. Thus the difference in the calculated variances may be neglected with a high degree of accuracy.

A.5 Fitting procedure for the extraction of the degrees of squeezing

The red line in Fig. 2.4(b) depicts the squeezing pattern in the simplified picture. Here the degree of squeezing is determined by a calculation similar to Eq. (2.10), with a minus prefactor (following the convention to assign positive values of the degree of squeezing for squeezing and negative ones for anti-squeezing) and using the ratio between the variances of the outgoing field and vacuum field taken at a given time moment. At times when the driving field vanishes this ratio depends exponentially on the squeezing strength r. For such a point inside a squeezing (anti-squeezing) region, it exponentially decays (grows) with r. In this case it is guaranteed that the squeezing turns into anti-squeezing and vice versa by changing the polarity of the driving field. This exponential

dependence is shown in Fig. 2.4(c) as the red lines, where the degree of squeezing at $t_\mathrm{d} = 0$ fs is plotted for both polarities of the driving field amplitude in dependence of the squeezing strength r. The observed asymmetry between the maximal positive values of the degree of squeezing (corresponding to squeezing) and its minimal negative values (corresponding to anti-squeezing) can serve as a direct measure of the degree of squeezing.

Figure 2.4(c) demonstrates that a similar measure can be used to extract the degree of squeezing from the RDV within the full description accounting for a finite detection window. The two grey lines reflect the corresponding maximal squeezing and anti-squeezing values obtained for the RDV for different polarities of the driving field amplitude. In order to extract the degree of squeezing from these lines an exponential fit

$$h_\pm(r) = A_1\big[\exp\left(\pm A_2 r\right) - 1\big] \tag{A.20}$$

is applied. The degree of squeezing is then given by $-\mathrm{RDV}/A_1$. Since the two fitting functions only differ in the sign of the exponent, the parameters A_1 and A_2 can be fitted well either to the squeezing or the anti-squeezing values, where the respective differences decrease for shorter probe pulse durations. One should select rather the squeezing branch, since the corresponding dynamics is better resolved than for the anti-squeezing, due to the slower flow of the conformal time in the former case. The result of this fit is shown in Fig. 2.4(c) as the dashed red lines. For the case of a much shorter probe pulse duration the extracted squeezing and anti-squeezing curves would coincide with the red curves of the simplified picture.

The right axes of Figs. 2.4(b) and 2.4(c) show the degrees of squeezing obtained in this way from the RDV and within the simplified picture.

Appendix B

Appendix

B.1 The Total Electro-Optic Signal; Detailed Calculation of the Diagrams

Here we give a detailed example for the calculation of the normally-ordered second moment of the signal Γ for a general quantum THz field with a vanishing mean field, given by the density matrix $\hat{\rho}_{\mathrm{THz}}$. In this case, the initial field density matrix is given by $\hat{\rho}_{\mathrm{field}} = |\{E_{\mathrm{p},z}\}\rangle\langle\{E_{\mathrm{p},z}\}| \otimes |0_{\mathrm{NIR},s}\rangle\langle 0_{\mathrm{NIR},s}| \otimes \hat{\rho}_{\mathrm{THz}}$. In order to obtain a non-vanishing contribution to the normally-ordered second moment Γ in Eq. (3.7), we need to expand the exponential to sixth order. The expectation value over the matter degrees of freedom may then be split into the product of two expectation values for two different molecules where each interacts once with each of the three fields.

To derive the nonlinear response of matter and pinpoint its quantum nature, we work with the $'\pm'$ superoperator algebra [13]. Figure B.1 depicts all of the diagrams contributing to Γ which is given in Eq. (3.7).

Since the probe field is considered classical because of its strong coherent amplitude, we can neglect any quantum features by only using the $'+'$-superoperator $\hat{E}_{\mathrm{p},z,+}$ for this field. This step means that it can be simply replaced by its coherent amplitude $E_{\mathrm{p},z}$. The generated NIR field $\hat{E}_{\mathrm{p},s}$ and the THz field $\hat{E}_{\mathrm{THz},s}$ are essentially quantum, i.e. they can appear with either superoperator index $'+'$ or $'-'$. The electro-optic signal in Eq. (3.3) describes the measurement of the generated NIR field. Consequently, the last interaction has to also occur with $\hat{E}_{\mathrm{p},s,-}$ for obtaining a non-vanishing expectation value for the matter degrees of freedom. Any other interaction would lead to a trace over a commutator for either the field or matter expectation value which vanishes. The previous interaction with $\hat{E}_{\mathrm{p},s}$ at the other molecule can then either be a $'+'$ or $'-'$. Contrary to $\hat{E}_{\mathrm{p},s}$, the last interaction with the THz field must be a $'+'$ to obtain a

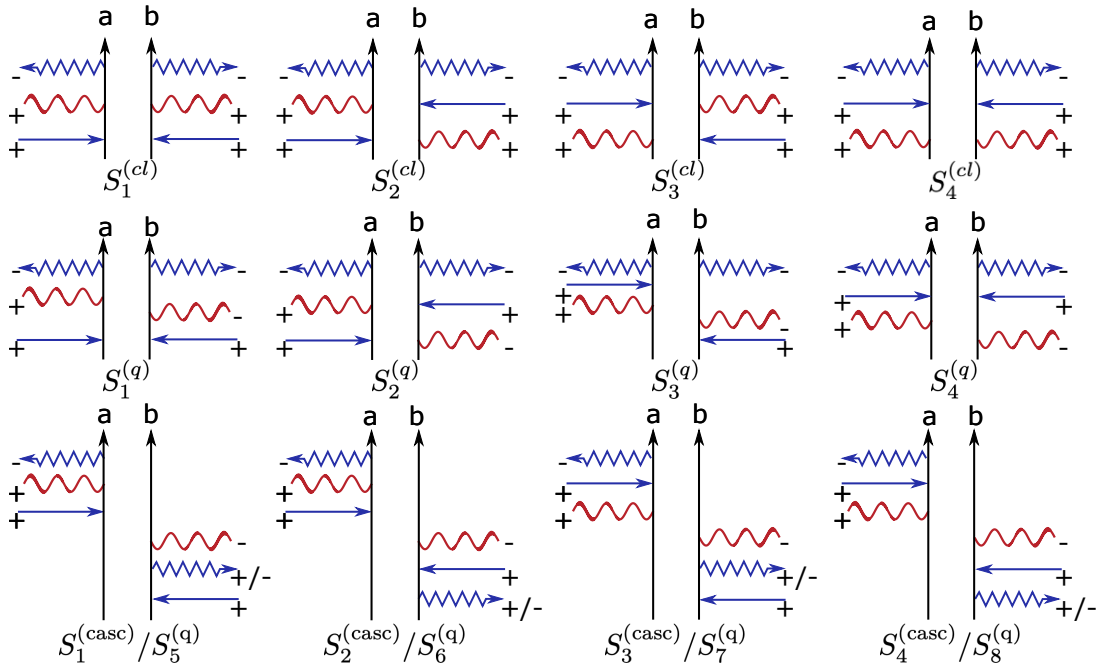

Figure B.1: Complete set of superoperator diagrams contributing to Γ [cf. Eq. (3.7)]. Vertical arrows represent the density matrices of a pair of molecules a and b as indicated, with the past at the bottom and the future at the top. Horizontal arrows denote interactions with the electric fields. Blue zigzag arrows: generated NIR field $\hat{E}_{\mathrm{p},s}$; wavy red lines: THz field $\hat{E}_{\mathrm{THz},s}$; straight blue arrows: coherent probe field $\hat{E}_{\mathrm{p},z}$. An arrow pointing to the right (left) corresponds to the annihilation (creation) of a photon. The interaction with the THz field (wavy red lines) does not have an arrow since for any interaction it can be pointing either to the right or to the left. The $\pm$ indices denote the superoperator nature of the corresponding mode of the interacting field. Additional contributing diagrams are given by flipping all field arrows attributed to molecule a and/or molecule b. Note that flipping the field arrows at both molecules results in the Hermitian conjugation of the corresponding terms. The first row describes the classical DFG response contribution to Γ if the THz arrows are chosen to point outwards at each molecule while the classical SFG is obtained when all of the THz arrows point inwards. Here, the intermolecular time ordering does not play any role. The second and third rows represent the quantum corrections to the classical response. Terms with the superscript (q) denote processes involving quantum susceptibilities on molecule b (note the two $'-'$-type interactions) while terms with the superscript (casc) describe cascading processes. For the second and third row, the intermolecular time ordering is important since the interaction with the THz field on molecule a has to always occur after the THz interaction with molecule b.

non-vanishing expectation value for the field degrees of freedom, since this field is not being measured. Again the previous interaction with the other molecule can either be a $'+'$ or $'-'$. These considerations leave us with the contributing diagrams shown in Fig. B.1.

The first row in Fig. B.1 depicts the classical matter response where the interaction of matter with the THz field is considered classical (because it is a $'+'$ for the field). In general, the response depends on the actual state of the THz field. The second row is essentially the same as the first with the difference that molecule b interacts with the THz mode according to the $'-'$ type. In that case, the response of molecule b may not be described by a classical susceptibility. Here, intermolecular time ordering is crucial since these diagrams only contribute to the electro-optic signal if the interaction with the THz field on molecule b takes place before the one at molecule a. The third row depicts diagrams where the last interaction with molecule b is with the THz field. That field must then be considered quantum (i.e. has to have a $'-'$) in order to obtain a non-vanishing expectation value for the matter degrees of freedom for molecule b. This finding means that the entire $\chi^{(2)}$ process on molecule b has to take place before the interaction with the THz field on molecule a. The diagrams in the third row where $\hat{E}_{\mathrm{p},s}$ interacts with molecule b according to a $'+'$ can be interpreted as cascaded $\chi^{(2)}$ processes [103] where, e.g., a THz photon is emitted during the first $\chi^{(2)}_{+--}$ interaction and is afterwards absorbed in a second $\chi^{(2)}_{+--}$ process emitting a NIR photon back into the detected field $\hat{E}_{\mathrm{p},s}$. The contributions to Γ given by the second and third row in Fig. B.1 involve the commutator of the THz field, essentially amounting to a factor proportional to its frequency Ω and are therefore independent on the actual state of the THz field.

To illustrate the difference between the classical and the quantum response, let us write down the contributions for diagrams $S_4^{(\mathrm{cl})}$ and $S_4^{(\mathrm{casc})}$ in Fig. B.1. We assume that the nonlinear medium consists of noninteracting molecules at uniform density and has a length of L along the propagation direction of the involved electric fields. The coherent amplitude of the probe field is represented by

$$E_{\mathrm{p},z}(\mathbf{r},t) = \int_0^\infty \mathrm{d}\omega E_{\mathrm{p},z}(\omega) e^{i(k_\omega x - \omega t)},$$

and the quantized electric field is given by

$$\begin{aligned}\hat{E}(\mathbf{r},t) &= \int_0^\infty \mathrm{d}\omega \hat{E}(x,\omega) e^{-i\omega t} \\ &= i\int_0^\infty \mathrm{d}\omega \sqrt{\frac{\hbar\omega}{C}} \left(\hat{a}(\omega)e^{ik_\omega x} + \hat{b}(\omega)e^{-ik_\omega x}\right) e^{-i\omega t}.\end{aligned}$$

Here, $\hat{E}(\mathbf{r},t)$ corresponds to the annihilation operator in the time domain, which is usually expressed as the positive frequency field $\hat{E}^{(+)}(\mathbf{r},t)$ in standard quantum optics notation [4]. We choose not to follow this convention here in order to avoid confusion with the superoperator notation. $\hat{a}(\omega)$ and $\hat{b}(\omega)$ are the bosonic annihilation operators for the forwards and backwards propagating wave, respectively. Note that we may neglect the backwards propagating wave for the NIR field because of unfavorable phasematching and only take it into account for the THz field. All fields are considered as plane waves propagating along the x-axis.

Diagram $S_4^{(\mathrm{cl})}$ for outwards-pointing THz field arrows, corresponding to two DFG processes, is given by

$$\begin{aligned}
S_4^{(\mathrm{cl})} &= \frac{-\rho_0^2}{\hbar^6}\int_V \mathrm{d}\mathbf{r}_a \int_V \mathrm{d}\mathbf{r}_b \int_{-\infty}^{\infty}\mathrm{d}\tau_3\int_{-\infty}^{\tau_3}\mathrm{d}\tau_2\int_{-\infty}^{\tau_2}\mathrm{d}\tau_1\int_{-\infty}^{\infty}\mathrm{d}\overline{\tau}_3\int_{-\infty}^{\overline{\tau}_3}\mathrm{d}\overline{\tau}_2\int_{-\infty}^{\overline{\tau}_2}\mathrm{d}\overline{\tau}_1 \\
&\times \mathrm{tr}\left\{ :\hat{\mathcal{S}}^2(\theta): \hat{E}^{\dagger}_{\mathrm{p},s,-}(\mathbf{r}_a,\tau_3)\hat{E}_{\mathrm{p},z,+}(\mathbf{r}_a,\tau_2)\hat{E}^{\dagger}_{\mathrm{THz},s,+}(\mathbf{r}_a,\tau_1)\hat{E}_{\mathrm{p},s,-}(\mathbf{r}_b,\overline{\tau}_3)\hat{E}^{\dagger}_{\mathrm{p},z,+}(\mathbf{r}_b,\overline{\tau}_2)\right. \\
&\times \left.\hat{E}_{\mathrm{THz},s,+}(\mathbf{r}_b,\overline{\tau}_1)\hat{\rho}_{\mathrm{field}}\right\}\mathrm{tr}\left\{\hat{V}_{s,+}(\tau_3)\hat{V}_{z,-}(\tau_2)\hat{V}_{s,-}(\tau_1)\hat{\rho}_{\mathrm{mat},a}\right\} \\
&\times \mathrm{tr}\left\{\hat{V}_{s,+}(\overline{\tau}_3)\hat{V}_{z,-}(\overline{\tau}_2)\hat{V}_{s,-}(\overline{\tau}_1)\hat{\rho}_{\mathrm{mat},b}\right\} \\
&= 2\left(\frac{N\omega_{\mathrm{p}}A\rho_0}{2\pi c_0}\right)^2\int_0^{\infty}\mathrm{d}\omega\mathrm{d}\omega'\mathrm{d}\omega_2\mathrm{d}\omega_1\mathrm{d}\Omega\mathrm{d}\Omega'\ \mathbb{E}(\omega,\omega',\omega_2,\omega_1)\int_{-\infty}^{\infty}\mathrm{d}\tau_3\mathrm{d}\overline{\tau}_3 \\
&\times \int_0^{\infty}\mathrm{d}t_2\mathrm{d}t_1\mathrm{d}\bar{t}_2\mathrm{d}\bar{t}_1 e^{i(\omega+\Omega-\omega_1)\tau_3}e^{i(\omega_1-\Omega)t_2}e^{-i\Omega t_1}e^{-i(\omega'+\Omega'-\omega_2)\overline{\tau}_3}e^{-i(\omega_2-\Omega')\bar{t}_2}e^{i\Omega'\bar{t}_1} \\
&\times \chi^{(2)}_{+--}(t_2,t_1)\chi^{(2)}_{+--}(\bar{t}_2,\bar{t}_1) \\
&\times \int_0^L \mathrm{d}x_a\int_0^L \mathrm{d}x_b e^{-i(k_\omega-k_{\omega_1})x_a}e^{i(k_{\omega'}-k_{\omega_2})x_b}\mathrm{tr}\left\{\hat{E}^{\dagger}_{\mathrm{THz},s}(x_a,\Omega)\hat{E}_{\mathrm{THz},s,+}(x_b,\Omega')\hat{\rho}_{\mathrm{THz}}\right\},
\end{aligned}$$

where

$$\mathbb{E}(\omega,\omega',\omega_2,\omega_1) = \frac{E^*_{\mathrm{p},z}(\omega)E_{\mathrm{p},z}(\omega')E^*_{\mathrm{p},z}(\omega_2)E_{\mathrm{p},z}(\omega_1)}{4\left(\int_0^{\infty}\mathrm{d}\omega\left|E_{\mathrm{p},z}(\omega)\right|^2\right)^2}$$

results from replacing the probe field operators $\hat{E}_{\mathrm{p},z}$ by their coherent amplitudes, $\omega_{\mathrm{p}} = \int_0^{\infty}\mathrm{d}\omega\left|E_{\mathrm{p},z}(\omega)\right|^2 / \int_0^{\infty}\mathrm{d}\omega\omega^{-1}\left|E_{\mathrm{p},z}(\omega)\right|^2$ is the average detected frequency and $N = C\int_0^{\infty}\mathrm{d}\omega\frac{1}{\hbar\omega}\left|E_{\mathrm{p},z}(\omega)\right|^2$ is the mean photon number of the coherent probe, coinciding with its variance which represents the shot noise. Furthermore, we have replaced the sums over the molecules by integrals, assuming that the average distance between the molecules are much shorter than the involved electric field wavelengths, $\sum_i \to \rho_0\int_V \mathrm{d}\mathbf{r}$, where ρ_0 is the molecular density and V is the volume of the sample. The expectation values over the molecular degrees of freedom are identical for each molecule and there-

fore independent of $\mathbf{r}$. Note that the first line for $S_4^{(\mathrm{cl})}$ includes time-ordered integrals. In order to avoid this time-ordering, we have changed the integration variables in the fourth line from the actual interaction times τ_i to the time intervals between successive interactions $t_i = \tau_{i+1} - \tau_i$ (and likewise for $\overline{\tau}_i$). The second-order susceptibilities $\chi^{(2)}_{+--}(t_2, t_1)$ are the Fourier transforms of those given in Eq. (1.79)
Finally, $S_4^{(\mathrm{cl})}$ is given by

$$\begin{aligned} S_4^{(\mathrm{cl})} = 2\left(\frac{N\omega_\mathrm{p}\rho_0}{c_0}\right)^2 \int_0^\infty \mathrm{d}\omega\mathrm{d}\omega'\mathrm{d}\Omega\mathrm{d}\Omega' \int_0^L \mathrm{d}x_a\mathrm{d}x_b \mathbb{E}(\omega,\omega',\omega'+\Omega',\omega+\Omega) e^{i(k_\Omega x_a - k_{\Omega'} x_b)} \\ \times \mathrm{tr}\left\{\hat{E}^\dagger_{\mathrm{THz},s}(x_a,\Omega)\hat{E}_{\mathrm{THz},s,+}(x_b,\Omega')\hat{\rho}_\mathrm{THz}\right\} \chi^{(2)}_{+--}(-\omega;\omega+\Omega,-\Omega) \\ \times \chi^{(2)*}_{+--}(-\omega';\omega'+\Omega,-\Omega) \end{aligned}$$

To obtain the expression for inwards-pointing arrows (two SFG processes) we simply need to change the sign of Ω (Ω') in every argument and use the general relation $\hat{E}_{\mathrm{THz},s}(-\Omega) = \hat{E}^\dagger_{\mathrm{THz},s}(\Omega)$.

For $S_4^{(\mathrm{casc})}$, we calculate the interaction with $\hat{E}_{\mathrm{p},s,+}$ on molecule b and sum up the diagrams where the THz arrows are pointing outwards and inwards. The result is

$$\begin{aligned} S_4^{(\mathrm{casc})} &= \frac{-\rho_0^2}{\hbar^6}\int_V \mathrm{d}\mathbf{r}_a \int_V \mathrm{d}\mathbf{r}_b \int_{-\infty}^\infty \mathrm{d}\tau_6 \int_{-\infty}^{\tau_6} \mathrm{d}\tau_5 \int_{-\infty}^{\tau_5} \mathrm{d}\tau_4 \int_{-\infty}^{\tau_4} \mathrm{d}\tau_3 \int_{-\infty}^{\tau_3} \mathrm{d}\tau_2 \int_{-\infty}^{\tau_2} \mathrm{d}\tau_1 \\ &\quad \times \mathrm{tr}\Big\{ :\hat{\mathcal{S}}^2(\theta): \hat{E}^\dagger_{\mathrm{p},s,-}(\mathbf{r}_a,\tau_6)\hat{E}_{\mathrm{p},z,+}(\mathbf{r}_a,\tau_5)\hat{E}^\dagger_{\mathrm{p},z,+}(\mathbf{r}_b,\tau_2)\hat{E}_{\mathrm{p},s,+}(\mathbf{r}_b,\tau_1) \\ &\quad \times \left[\hat{E}_{\mathrm{THz},s,+}(\mathbf{r}_a,\tau_4)\hat{E}^\dagger_{\mathrm{THz},s,-}(\mathbf{r}_b,\tau_3) + \hat{E}^\dagger_{\mathrm{THz},s,+}(\mathbf{r}_a,\tau_4)\hat{E}_{\mathrm{THz},s,-}(\mathbf{r}_b,\tau_3)\right]\hat{\rho}_\mathrm{field}\Big\} \\ &\quad \times \mathrm{tr}\left\{\hat{V}_{s,+}(\tau_6)\hat{V}_{z,-}(\tau_5)\hat{V}_{s,-}(\tau_4)\hat{\rho}_{\mathrm{mat},a}\right\}\mathrm{tr}\left\{\hat{V}_{s,+}(\tau_3)\hat{V}_{z,-}(\tau_2)\hat{V}_{s,-}(\tau_1)\hat{\rho}_{\mathrm{mat},b}\right\} \\ &= -\left(\frac{N\omega_\mathrm{p}\rho_0}{2\pi c_0}\right)^2 \int_0^\infty \mathrm{d}\omega\mathrm{d}\omega'\mathrm{d}\omega_2\mathrm{d}\omega_1\mathrm{d}\Omega\ \mathbb{E}(\omega,\omega',\omega_2,\omega_1)\frac{\hbar\Omega}{C}\int_{-\infty}^\infty \mathrm{d}\tau_6 \\ &\quad \times \int_0^\infty \mathrm{d}t_5\mathrm{d}t_4\mathrm{d}t_3\mathrm{d}t_2\mathrm{d}t_1 e^{i(\omega-\omega_1-\omega'+\omega_2)\tau_6} e^{i(\omega_1+\omega'-\omega_2)t_5} e^{i(\omega'-\omega_2)t_4} e^{i(\omega'-\omega_2)t_2} e^{i\omega' t_1} \\ &\quad \times \chi^{(2)}_{+--}(t_5,t_4)\chi^{(2)}_{+--}(t_2,t_1)\int_0^L \mathrm{d}x_a \int_0^L \mathrm{d}x_b e^{-i(k_\omega - k_{\omega_1})x_a} e^{i(k'_\omega - k_{\omega_2})x_b} \\ &\quad \times 2\cos(k_\Omega(x_a - x_b))\left[e^{-i\Omega t_3} - e^{i\Omega t_3}\right] e^{i(\omega'-\omega_2)t_3}. \end{aligned}$$

Note that $S_4^{(\mathrm{casc})}$ involves a completely time-ordered expression where the entire $\chi^{(2)}$ process on molecule b needs to occur before the $\chi^{(2)}$ process on molecule a starts. In comparison, the two $\chi^{(2)}$ processes in $S_4^{(\mathrm{cl})}$ happen completely independent of each

other, i.e. there is no intermolecular time ordering. Finally, $S_4^{(\mathrm{casc})}$ is given by

$$\begin{aligned}S_4^{(\mathrm{casc})} = &-\left(\frac{N\omega_\mathrm{p}L\rho_0}{c_0}\right)^2\int_0^\infty \mathrm{d}\omega\mathrm{d}\omega'\mathrm{d}\overline{\omega}\mathbb{E}(\omega,\omega',\overline{\omega},\omega+\overline{\omega}-\omega')\\ &\times\left(\frac{\hbar(\omega'-\overline{\omega})}{2C}\left[1+\mathrm{sinc}\big(2(\omega'-\overline{\omega})L/c_0\big)^2\right]-i\frac{\hbar c_0}{2LC}\left[3+\mathrm{sinc}\big(2(\omega'-\overline{\omega})L/c_0\big)^2\right]\right)\\ &\times\chi^{(2)}_{+--}(-\omega;\omega-\omega'+\overline{\omega},\omega'-\overline{\omega})\chi^{(2)*}_{+--}(\omega'-\overline{\omega};\overline{\omega},-\omega').\end{aligned}$$

In order to compare $S_4^{(\mathrm{casc})}$ to the classical contribution, we can employ the substitutions $\overline{\omega}=\omega'-\Omega$ if $\omega'-\overline{\omega}\geq 0$ and $\overline{\omega}=\omega'+\Omega$ if $\omega'-\overline{\omega}\leq 0$ to obtain

$$\begin{aligned}S_4^{(\mathrm{casc})} = &\left(\frac{N\omega_\mathrm{p}L\rho_0}{c_0}\right)^2\int_0^\infty \mathrm{d}\omega\mathrm{d}\omega'\mathrm{d}\Omega\mathbb{E}(\omega,\omega',\omega+\Omega,\omega'+\Omega)\\ &\times\left(\frac{\hbar\Omega}{2C}\left[1+\mathrm{sinc}^2\big(2\Omega L/c_0\big)\right]+i\frac{\hbar c_0}{2LC}\left[3+\mathrm{sinc}^2\big(2\Omega L/c_0\big)\right]\right)\\ &\times\chi^{(2)}_{+--}(-\omega;\omega+\Omega,-\Omega)\chi^{(2)*}_{+--}(-\Omega;\omega'+\Omega,-\omega')\\ &-\left(\frac{N\omega_\mathrm{p}L\rho_0}{c_0}\right)^2\int_0^\infty \mathrm{d}\omega\mathrm{d}\omega'\mathrm{d}\Omega\mathbb{E}(\omega,\omega',\omega-\Omega,\omega'-\Omega)\\ &\times\left(\frac{\hbar\Omega}{2C}\left[1+\mathrm{sinc}^2\big(2\Omega L/c_0\big)\right]-i\frac{\hbar c_0}{2LC}\left[3+\mathrm{sinc}^2\big(2\Omega L/c_0\big)\right]\right)\\ &\times\chi^{(2)}_{+--}(-\omega;\omega-\Omega,\Omega)\chi^{(2)*}_{+--}(\Omega;\omega'-\Omega,-\omega').\end{aligned}$$

In the end, the total normally-ordered second moment Γ is given by

$$\begin{aligned}\Gamma = \mathrm{tr}&\left\{\left[\frac{N\omega_\mathrm{p}L\rho_0}{c_0}\int_0^\infty\mathrm{d}\Omega\int_0^L\mathrm{d}x\ \left(e^{-ik_\Omega x}\hat{E}_{\mathrm{THz},s}(x,\Omega)D(\Omega,\theta)+H.c.\right)\right]^2\hat{\rho}_\mathrm{THz}\right\}\\ &+\left(\frac{N\omega_\mathrm{p}L\rho_0}{c_0}\right)^2\int_0^\infty\mathrm{d}\Omega\ \frac{\hbar\Omega}{C}\left[1+\mathrm{sinc}^2\big(2\Omega L/c_0\big)\right]\Big(\Re\left\{D(\Omega,\theta)\left[D_\mathrm{q}(\Omega,\theta)+D_\mathrm{casc}(\Omega,\theta)\right]\right\}\\ &\quad-\frac{\hbar c_0}{CL}\left[3+\mathrm{sinc}^2\big(2\Omega L/c_0\big)\right]\Im\left\{D(\Omega,\theta)\left[D_\mathrm{q}(\Omega,\theta)+D_\mathrm{casc}(\Omega,\theta)\right]\right\}\Big).\end{aligned}\tag{B.1}$$

In general, the strengths of all contributions depend on the strength of the probe (entering as the photon number N of the probe), the length of the crystal L, and the strength of the dipole moments. The quantum contribution can be isolated at a phase shift of $\theta=\pi$. In order to increase the relative contribution of the cascading processes in Figure 3.4(a) and (b) one could utilize its linear scaling with the crystal length in contrast to the quadratic scaling of the classical contribution Γ_I.

The susceptibilities contained in the gating functions are given in Eq. (1.90).

Note that only the classical contribution given in the first line of Eq. (B.1) actually

depends on the state of the THz field. Furthermore, the expression inside of the square brackets of the classical contribution represents the first correction according to the THz field to the mean value of the electro-optic signal $\hat{\mathcal{S}}(\theta)$ itself.

Equation (B.1) together with Eq. (1.90) provide the general solution for Γ for arbitrary three-level schemes. In case of the specific level scheme shown in Figure 3.1, the expression for $\chi^{(2)}$ in Eq. (1.90) can be shortened significantly if the RWA approximation is employed. Here, the NIR probe as well as the generated s-polarized NIR field are off-resonant with respect to all molecular transition frequencies, so that only the THz field can drive resonant transitions (described by slowly rotating terms in the time domain). These resonant transitions enter in Eq. (1.90) in form of the functions $I_{g'g}(\Omega)$ or $I_{gg'}(-\Omega)$. The input arguments of the functions $I_{a'b'}$ [where $a'b'$ runs over all possible combinations in Eq. (1.90)] are given by the sum of the frequencies corresponding to all field interactions preceding the evolution reflected by $I_{a'b'}$. Looking at the sum in Eq. (1.90), we can therefore notice that the resonant terms occur either if the THz field is the field interacting first with the molecule or if it is the last field. In the latter case the frequency argument $\pm\Omega$ results, e.g., from the sum of the frequency of the probe $\omega \pm \Omega$ and the frequency $-\omega$ of $\hat{E}_{\mathrm{p},s}$. All diagrams containing these resonant transitions are shown in Figure 3.2.

Finally, Eq. (3.9) can be obtained by evaluating Eq. (B.1) for $\hat{\rho}_{\mathrm{THz}} = |0\rangle\langle 0|$.

Bibliography

[1] R. Hanbury Brown and R. Q. Twiss, Nature **177**, 27 (1956).

[2] R. Hanbury Brown and R. Q. Twiss, Proceedings of the Royal Society of London. Series A. Mathematical and Physical Sciences **242**, 300 (1957).

[3] R. Hanbury Brown and R. Q. Twiss, Proceedings of the Royal Society of London. Series A. Mathematical and Physical Sciences **243**, 291 (1958).

[4] R. J. Glauber, Phys. Rev. **130**, 2529 (1963).

[5] R. J. Glauber, Phys. Rev. **131**, 2766 (1963).

[6] C. Riek, D. V. Seletskiy, A. S. Moskalenko, J. F. Schmidt, P. Krauspe, S. Eckart, S. Eggert, G. Burkard, and A. Leitenstorfer, Science **350**, 420 (2015).

[7] A. S. Moskalenko, C. Riek, D. V. Seletskiy, G. Burkard, and A. Leitenstorfer, Phys. Rev. Lett. **115**, 263601 (2015).

[8] C. Riek, P. Sulzer, M. Seeger, A. S. Moskalenko, G. Burkard, D. V. Seletskiy, and A. Leitenstorfer, Nature **541**, 376 (2017).

[9] I.-C. Benea-Chelmus, F. F. Settembrini, G. Scalari, and J. Faist, Nature **568**, 202 (2019).

[10] W. Vogel and D. Welsch, *Quantum Optics*, 3rd ed. (Wiley, Weinheim, 2006).

[11] A. Salam, *Molecular Quantum Electrodynamics* (John Wiley and Sons, 2010).

[12] R. Loudon, *The Quantum Theory of Light* (Oxford University Press, New York, 2000).

[13] S. Mukamel, *Principles of Nonlinear Optical Spectroscopy* (Oxford University Press, Oxford, 1995).

[14] A. Aiello and J. P. Woerdman, Phys. Rev. A **72**, 060101 (2005).

[15] G. F. Calvo, A. Picón, and E. Bagan, Phys. Rev. A **73**, 013805 (2006).

[16] M. Abramowitz and I. Stegun, *Handbook of Mathematical Functions: with Formulas, Graphs, and Mathematical Tables* (Dover, New York, 2012).

[17] L. Yu, W. Huang, M. Huang, Z. Zhu, X. Zeng, and W. Ji, Journal of Physics A: Mathematical and General **31**, 9353 (1998).

[18] J. W. Goodman, *Introduction to Fourier Optics* (McGraw-Hill, New York, 1996).

[19] B. Huttner and S. M. Barnett, Phys. Rev. A **46**, 4306 (1992).

[20] J. J. Hopfield, Phys. Rev. **112**, 1555 (1958).

[21] S. Y. Buhmann, *Dispersion Forces I; Macroscopic Quantum Electrodynamics and Ground-State Casimir, Casimir-Polder and van der Waals Forces)* (Springer, Berlin, 2012).

[22] P. G. Kwiat, E. Waks, A. G. White, I. Appelbaum, and P. H. Eberhard, Phys. Rev. A **60**, 773 (1999).

[23] P. J. Mosley, J. S. Lundeen, B. J. Smith, P. Wasylczyk, A. B. U'Ren, C. Silberhorn, and I. A. Walmsley, Phys. Rev. Lett. **100**, 133601 (2008).

[24] P. Sharapova, A. M. Pérez, O. V. Tikhonova, and M. V. Chekhova, Phys. Rev. A **91**, 043816 (2015).

[25] C. Silberhorn, Contemp. Phys. **48**, 143 (2007).

[26] S. Mukamel *et al.*, J. Phys. B: At. Mol. Opt. Phys. **53**, 072002 (2020).

[27] O. Roslyak and S. Mukamel, Mol. Phys. **107**, 265 (2009).

[28] K. E. Dorfman and S. Mukamel, Phys. Rev. A **86**, 023805 (2012).

[29] K. E. Dorfman, F. Schlawin, and S. Mukamel, Rev. Mod. Phys. **88**, 045008 (2016).

[30] R. W. Boyd, *Nonlinear Optics (Third Edition)* (Academic Press, Burlington, 2008).

[31] J. J. Sakurai, *Advanced Quantum Mechanics* (Addison-Wesley, 1967).

[32] W. E. Lamb and R. C. Retherford, Phys. Rev. **72**, 241 (1947).

[33] A. Fragner, M. Göppl, J. M. Fink, M. Baur, R. Bianchetti, P. J. Leek, A. Blais, and A. Wallraff, Science **322**, 1357 (2008).

[34] H. Casimir, Proc. K. Ned. Akad. Wet. **51**, 793 (1948).

[35] H. B. G. Casimir and D. Polder, Phys. Rev. **73**, 360 (1948).

[36] H. J. Kimble, M. Dagenais, and L. Mandel, Phys. Rev. Lett. **39**, 691 (1977).

[37] L. Mandel, Phys. Rev. Lett. **49**, 136 (1982).

[38] R. E. Slusher, L. W. Hollberg, B. Yurke, J. C. Mertz, and J. F. Valley, Phys. Rev. Lett. **55**, 2409 (1985).

[39] G. Breitenbach, S. Schiller, and J. Mlynek, Nature **387**, 471 (1997).

[40] Q. Wu and X. Zhang, Appl. Phys. Lett. **67**, 3523 (1995).

[41] A. Nahata, A. S. Weling, and T. F. Heinz, Appl. Phys. Lett. **69**, 2321 (1996).

[42] G. Gallot and D. Grischkowsky, J. Opt. Soc. Am. B **16**, 1204 (1999).

[43] K. Liu, J. Xu, and X.-C. Zhang, Appl. Phys. Lett. **85**, 863 (2004).

[44] C. Kübler, R. Huber, S. Tübel, and A. Leitenstorfer, Appl. Phys. Lett. **85**, 3360 (2004).

[45] C. Kubler, R. Huber, and A. Leitenstorfer, Semicond. Sci. Technol. **20**, S128 (2005).

[46] A. Leitenstorfer, S. Hunsche, J. Shah, M. C. Nuss, and W. H. Knox, Appl. Phys. Lett. **74**, 1516 (1999).

[47] S. Keiber, S. Sederberg, A. Schwarz, M. Trubetskov, V. Pervak, F. Krausz, and N. Karpowicz, Nat. Photonics **10**, 159 (2016).

[48] M. G. Raymer, J. Cooper, H. J. Carmichael, M. Beck, and D. T. Smithey, J. Opt. Soc. Am. B **12**, 1801 (1995).

[49] I.-C. Benea-Chelmus, C. Bonzon, C. Maissen, G. Scalari, M. Beck, and J. Faist, Phys. Rev. A **93**, 043812 (2016).

[50] F. Lindel, R. Bennett, and S. Y. Buhmann, Phys. Rev. A **102**, 041701 (2020).

[51] F. Lindel, R. Bennett, and S. Y. Buhmann, Phys. Rev. A **103**, 033705 (2021).

[52] F. Lindel, F. F. Settembrini, R. Bennett, and S. Y. Buhmann, "Probing the Purcell effect without radiative decay: Lessons in the frequency and time domains," (2021), arXiv:2107.02647 .

[53] F. F. Settembrini, F. Lindel, A. M. Herter, S. Y. Buhman, and J. Faist, "Detection of quantum-vacuum field correlations outside the light cone," (2021), arXiv:2111.02377 .

[54] S. De Liberato, Phys. Rev. A **100**, 031801 (2019).

[55] M. Kizmann, T. L. M. Guedes, D. V. Seletskiy, A. S. Moskalenko, A. Leitenstorfer, and G. Burkard, Nat. Phys. **15**, 960 (2019).

[56] M. Kizmann, "Quantitative theory of the generation and detection of squeezed light transients in nonlinear crystals on subcycle time scales," (2017), Master thesis.

[57] E. Knill, R. Laflamme, and G. J. Milburn, Nature **409**, 46 (2001).

[58] C. Weedbrook, S. Pirandola, R. García-Patrón, N. J. Cerf, T. C. Ralph, J. H. Shapiro, and S. Lloyd, Rev. Mod. Phys. **84**, 621 (2012).

[59] M. A. Broome, A. Fedrizzi, S. Rahimi-Keshari, J. Dove, S. Aaronson, T. C. Ralph, and A. G. White, Science **339**, 794 (2013).

[60] A. N. Boto, P. Kok, D. S. Abrams, S. L. Braunstein, C. P. Williams, and J. P. Dowling, Phys. Rev. Lett. **85**, 2733 (2000).

[61] M. D'Angelo, M. V. Chekhova, and Y. Shih, Phys. Rev. Lett. **87**, 013602 (2001).

[62] D. J. Jones, S. A. Diddams, J. K. Ranka, A. Stentz, R. S. Windeler, J. L. Hall, and S. T. Cundiff, Science **288**, 635 (2000).

[63] R. Holzwarth, T. Udem, T. W. Hänsch, J. C. Knight, W. J. Wadsworth, and P. S. J. Russell, Phys. Rev. Lett. **85**, 2264 (2000).

[64] P. B. Corkum and F. Krausz, Nat. Phys. **3**, 381 (2007).

[65] F. Krausz and M. Ivanov, Rev. Mod. Phys. **81**, 163 (2009).

[66] A. S. Moskalenko, Z.-G. Zhu, and J. Berakdar, Phys. Rep. **672**, 1 (2017), and references therein.

[67] A. I. Lvovsky, "Squeezed light," in *Photonics: Scientific Foundations, Technology and Applications, Vol. 1*, edited by D. L. Andrews (John Wiley & Sons, Hoboken, 2015) pp. 121–163.

[68] M. Chekhova, G. Leuchs, and M. Zukowski, Opt. Commun. **337**, 27 (2015).

[69] C. M. Caves, Phys. Rev. D **23**, 1693 (1981).

[70] M. Xiao, L.-A. Wu, and H. J. Kimble, Phys. Rev. Lett. **59**, 278 (1987).

[71] P. Grangier, R. E. Slusher, B. Yurke, and A. LaPorta, Phys. Rev. Lett. **59**, 2153 (1987).

[72] J. Abadie *et al.*, Nat. Phys. **7**, 962 (2011).

[73] J. Aasi *et al.*, Nat. Photonics **7**, 613 (2013).

[74] B. P. Abbott *et al.*, Phys. Rev. Lett. **116**, 061102 (2016).

[75] K. J. Blow, R. Loudon, S. J. D. Phoenix, and T. J. Shepherd, Phys. Rev. A **42**, 4102 (1990).

[76] M. E. Anderson, D. F. McAlister, M. G. Raymer, and M. C. Gupta, J. Opt. Soc. Am. B **14**, 3180 (1997).

[77] R. E. Slusher, P. Grangier, A. LaPorta, B. Yurke, and M. J. Potasek, Phys. Rev. Lett. **59**, 2566 (1987).

[78] W. Wasilewski, A. I. Lvovsky, K. Banaszek, and C. Radzewicz, Phys. Rev. A **73**, 063819 (2006).

[79] S. E. Harris, Phys. Rev. Lett. **98**, 063602 (2007).

[80] D. B. Horoshko and M. I. Kolobov, Phys. Rev. A **88**, 033806 (2013).

[81] A. Christ, B. Brecht, W. Mauerer, and C. Silberhorn, New J. Phys. **15**, 053038 (2013).

[82] Y. Shaked, Y. Michael, R. Z. Vered, L. Bello, M. Rosenbluh, and A. Pe'er, Nat. Commun. **9**, 609 (2018).

[83] P. R. Sharapova, O. V. Tikhonova, S. Lemieux, R. W. Boyd, and M. V. Chekhova, Phys. Rev. A **97**, 053827 (2018).

[84] P. C. M. Planken, H.-K. Nienhuys, H. J. Bakker, and T. Wenckebach, J. Opt. Soc. Am. B **18**, 313 (2001).

[85] T. Brabec and F. Krausz, Phys. Rev. Lett. **78**, 3282 (1997).

[86] Y. R. Shen, *Principles of nonlinear optics* (Wiley-Interscience, New York, 1984).

[87] P. E. Powers, *Fundamentals of Nonlinear Optics* (Taylor & Francis, Boca Raton, 2011).

[88] T. L. M. Guedes, M. Kizmann, D. V. Seletskiy, A. Leitenstorfer, G. Burkard, and A. S. Moskalenko, Phys. Rev. Lett. **122**, 053604 (2019).

[89] F. Belgiorno, S. L. Cacciatori, G. Ortenzi, L. Rizzi, V. Gorini, and D. Faccio, Phys. Rev. D **83**, 024015 (2011).

[90] V. Mukhanov, *Physical Foundations of Cosmology* (Cambridge University Press, Cambridge, 2005).

[91] Y. Kawada, T. Yasuda, and H. Takahashi, Opt. Lett. **41**, 986 (2016).

[92] C. Riek, P. Sulzer, M. Seeger, D. V. Seletskiy, and A. Leitenstorfer, in *Conference on Lasers and Electro-Optics* (Optical Society of America, 2016) p. SM1L.1.

[93] S. Virally and B. Reulet, Phys. Rev. A **100**, 023833 (2019).

[94] M. Kizmann, A. S. Moskalenko, A. Leitenstorfer, G. Burkard, and S. Mukamel, Laser Photonics Rev. , 2100423 (2021).

[95] W. M. Tolles, J. W. Nibler, J. R. McDonald, and A. B. Harvey, Appl. Spectrosc. **31**, 253 (1977).

[96] M. Cho, N. F. Scherer, G. R. Fleming, and S. Mukamel, J. Chem. Phys. **96**, 5618 (1992).

[97] D. M. Jonas, Annu. Rev. Phys. Chem. **54**, 425 (2003).

[98] M. O. Scully and M. S. Zubairy, *Quantum Optics* (Cambridge University Press, Cambridge, 1997).

[99] M. Kira, S. W. Koch, R. P. Smith, A. E. Hunter, and S. T. Cundiff, Nat. Phys. **7**, 799 (2011).

[100] A. Yabushita and T. Kobayashi, Phys. Rev. A **69**, 013806 (2004).

[101] D. A. Kalashnikov, Z. Pan, A. I. Kuznetsov, and L. A. Krivitsky, Phys. Rev. X **4**, 011049 (2014).

[102] P. Sulzer, K. Oguchi, J. Huster, M. Kizmann, T. L. M. Guedes, A. Liehl, C. Beckh, A. S. Moskalenko, G. Burkard, D. V. Seletskiy, and A. Leitenstorfer, Phys. Rev. A **101**, 033821 (2020).

[103] K. Bennett and S. Mukamel, J. Chem. Phys. **140**, 044313 (2014).

[104] W. P. Schleich, *Quantum Optics in Phase Space* (Wiley-VCH, Berlin, 2001).

[105] L. Allen, M. W. Beijersbergen, R. J. C. Spreeuw, and J. P. Woerdman, Phys. Rev. A **45**, 8185 (1992).

[106] R. P. Kanwal, *Linear Integral Equations: Theory and Technique* (Academic Press, 1971).

[107] D. T. Smithey, M. Beck, M. G. Raymer, and A. Faridani, Phys. Rev. Lett. **70**, 1244 (1993).

[108] H. P. Yuen and V. W. S. Chan, Opt. Lett. **8**, 177 (1983).

[109] G. L. Abbas, V. W. S. Chan, and T. K. Yee, Opt. Lett. **8**, 419 (1983).

[110] K. Vogel and H. Risken, Phys. Rev. A **40**, 2847 (1989).

[111] J. Tiedau, V. S. Shchesnovich, D. Mogilevtsev, V. Ansari, G. Harder, T. J. Bartley, N. Korolkova, and C. Silberhorn, N. J. Phys. **20**, 033003 (2018).

[112] K. Laiho, K. N. Cassemiro, D. Gross, and C. Silberhorn, Phys. Rev. Lett. **105**, 253603 (2010).

[113] A. I. Lvovsky and M. G. Raymer, Rev. Mod. Phys. **81**, 299 (2009).

[114] M. G. Raymer and I. A. Walmsley, Physica Scripta **95**, 064002 (2020).

[115] C. Fabre and N. Treps, Rev. Mod. Phys. **92**, 035005 (2020).

[116] N. Quesada and J. E. Sipe, Opt. Lett. **41**, 364 (2016).

[117] B. L. Schumaker, Physics Reports **135**, 317 (1986).

[118] H. Fan, J. Opt. B: Q. S. Opt. **5**, R147 (2003).

[119] S. Virally, P. Cusson, and D. V. Seletskiy, "Enhanced electro-optic sampling with quantum probes," (2021), arXiv:2106.04402 [quant-ph] .